Coastal Zone Simulations with Variational Boussinesq Modelling

Didit Adytia

COASTAL ZONE SIMULATIONS
WITH VARIATIONAL BOUSSINESQ MODELLING

Didit Adytia

Samenstelling promotiecommissie:

Voorzitter en secretaris:	
prof.dr.ir. A. J. Mouthaan	University of Twente
Promotor	
prof.dr.ir. E. W. C. van Groesen	University of Twente
Leden	
prof.dr. S. A. van Gils	University of Twente
prof.dr. S. J. M. H. Hulscher	University of Twente
prof.dr.ir. R. H. M. Huijsmans	Delft University of Technology
prof.dr.ir. W. S. J. Uijttewaal	Delft University of Technology
prof.dr. C. Kharif	IRPHE, France
dr. Andonowati	LabMath-Indonesia & Institut Teknologi Bandung, Indonesia

The research presented in this thesis has been performed within the group of Applied Analysis and Mathematical Physics (AAMP), Departement of Applied Mathematics, University of Twente, PO Box 217, 7500 AE Enschede, The Netherlands and Laboratorium Matematika Indonesia (LabMath-Indonesia), Lawangwangi, Bandung, Indonesia.

Cover: Erika Tivarini, www.erikativarini.carbonmade.com
Printed by Wöhrmann Print Service, Zutphen, The Netherlands.
ISBN 978-90-365-3351-5
DOI 10.3990/1.9789036533515

COASTAL ZONE SIMULATIONS WITH VARIATIONAL BOUSSINESQ MODELLING

DISSERTATION

to obtain
the degree of doctor at the University of Twente,
on the authority of the rector magnificus,
prof. dr. H. Brinksma,
on account of the decision of the graduation committee,
to be publicly defended
on Thursday the 24^{th} May 2012 at 12:45

by

Didit Adytia
born on 5^{th} February 1983
in Belitung, Indonesia

Dit proefschrift is goedgekeurd door de promotor
prof. dr. ir. E. W. C. van Groesen

For my mother
Yensi Nio

Contents

Summary

Water waves propagating from the deep ocean to the coast show large changes in their profile, waveheight, wavelength and direction. The main challenge to simulate the essential wave characteristics is to model the wave speeds and nonlinear interactions. These problems have been addressed since 1872 when J.V. Boussinesq tried to simplify the Euler equations for irrotational, incompressible fluid from the full three dimensional water wave problem to two horizontal space dimensions. Since then, many different types of Boussinesq models have been designed. The quality of a Boussinesq model depends very much on the accuracy of the dispersion. Dispersion is the depth-dependent relation between the speed and the wavelength. It is a consequence of the modelling from 3D to 2D. The relation can be exactly calculated for small amplitude waves, and is then given by a non-algebraic relation. This is a source of many problems for most numerical discretization methods if this relation has to be accurate from the deep ocean to the shallow coast. Most Boussinesq models are derived using series expansions in 'small' parameters as wave height and inverse wavelength, and prescribing a restricted wave regime for which the model should be most accurate.

A completely different way of modelling became possible in the 1960's. In 1967 Luke formulated a variational principle, which can be transformed to an action principle for the water wave problem. The equations for the critical points are a dynamic system of equations in Hamilton form. This Hamiltonian formulation was given by Zakharov in 1968, independent of the result of Luke. This clearly showed that the water wave problem can be written exactly in terms of quantities (elevation and surface potential) of two horizontal directions. In this thesis we will use this formulation to find so-called Variational Boussinesq Models that are accurate as needed and furthermore easy to implement in a numerical Finite Element code; in all approximations and discretizations, the Hamiltonian structure remains attained.

The most important quantity in the variational formulation is the Hamiltonian, which is the total energy, i.e. the sum of potential and kinetic energy. The potential energy can easily be expressed exactly in the surface elevation. The kinetic energy is the squared interior velocity, integrated at each instant over the fluid domain, with given fluid potential at the surface. Actually, related to Dirichlet principle, the kinetic energy functional is minimal (only) for the desired incompressible fluid flow. Instead of solving (numeri-

cally) the Laplace problem for the interior potential (which would be the full 3D wave problem), a consistent and explicit approximation of kinetic energy in the surface variables can be made by restricting the minimization to a subclass of fluid potentials. In Klopman et al. [2010], a Boussinesq-type model has been derived by choosing as subclass the surface potential to which is added a linear combination of vertical profiles with spatially dependent functions as coefficients. The minimization property of the kinetic energy requires that these spatial functions have to satisfy a (linear) elliptic equation. The vertical profile was chosen to be a parabola inspired by the parabolic shape function in the classical Boussinesq equations.

In this thesis we will use so-called vertical Airy profiles functions, i.e. hyperbolic-cosine functions which appear in the exact expression for harmonic waves of linear potential theory. Using these functions we can get flexibility to improve the dispersion, which for the parabolic profile is only valid for long waves. This improvement is based on a method to use in an optimal way the parameters (wave numbers) in the vertical Airy profiles so that broad-band waves such as wind-waves can be dealt with. The optimal choice is again based on exploiting the minimization property of the kinetic energy. However, to become practically applicable, we need information from the initial state, or from properties of waves entering the fluid domain. This has as consequence that each specific problem gets a tailor-made model, with dispersion that is sufficiently accurate for all the waves under consideration. As is well-known, the underlying variational formulation of our model makes a numerical Finite Element implementation most appropriate, especially also because simple piecewise linear splines can be used since no higher than first order spatial derivatives appear in the positive definite Hamiltonian. The quality of our modelling is shown by results of simulations for various classes of broad-band waves. Simulations of irregular wind waves are compared for various cases with recent experiments by MARIN hydrodynamic laboratory. To test the performance of shoaling, refraction and nonlinearity, simulations are compared with the classical Berkhoff experiment. Finally we show simulations for realistic wind-waves in the complicated geometry and bathymetry of the Jakarta harbour. The work in this thesis has been published in international scientific journals and in proceedings of international conferences.

Samenvatting

Watergolven vertonen gedurende de reis van de diepe oceaan naar de kust grote veranderingen in vorm, golfhoogte, golflengte en voortplantingsrichting. Om deze golven te simuleren is de grootste uitdaging het goed modelleren van de golfsnelheden en de niet-lineaire interacties. Deze problemen worden bestudeerd sinds 1872 toen J.V. Boussinesq probeerde de Eulervergelijkingen voor rotatie-vrije en onsamendrukbare stroming te vereenvoudigen van het volle drie-dimensionale golfprobleem naar een probleem in twee ruimtelijke dimensies. Sinds die tijd zijn veel verschillende soorten Boussinesq modellen ontworpen.

De kwaliteit van zo'n Boussinesq model hangt sterk af van de nauwkeurigheid van de dispersie. Dispersie is de diepteafhankelijke relatie tussen de snelheid en golflengte van een golf. Het is een gevolg van de modellering van 3D naar 2D. Deze relatie kan exact berekend worden voor kleine golfhoogten, en wordt dan door een niet-algebraïsche relatie gegeven. Voor de meeste numerieke discretizatiemethoden is dit de oorsprong van veel problemen, zeker als de relatie nauwkeurig moet zijn van de diepe oceaan tot de kust. De meeste Boussinesq modellen worden afgeleid met een ontwikkeling in kleine parameters zoals golfhoogte en de inverse golflengte, en met een specificatie van de golftypen waarvoor de benadering het meest nauwkeurig moet zijn.

Een totaal andere manier van modelleren werd mogelijk in de zestiger jaren van de vorige eeuw. In 1967 formueerde Luke een variatieprincipe dat omgewerkt kan worden naar een actieprincipe voor de watergolven. De vergelijkingen voor de kritieke punten vormen een dynamisch systeem met Hamiltonse vorm. Deze Hamiltonse formulering werd, onafhankelijk van Luke, in 1968 gegeven door Zakharov. Daardoor werd het duidelijk dat het golfprobleem exact geschreven kan worden als een probleem in twee grootheden (namelijk de waterhoogte en de potentiaal ter plaatse van het wateroppervlak) die slechts van de twee horizontale richtingen afhangen. In dit proefschrift gebruiken we deze formulering om zogenoemde Variational Boussinesq modellen af te leiden; modellen die zo nauwkeurig zijn als vereist en daarnaast eenvoudig te implementeren zijn in een numerieke Eindige Elementen code. In de modelbenaderingen en de discretizaties blijft de Hamiltonse structuur gehandhaafd.

De belangrijkste grootheid in de variationele formulering is de Hamiltoniaan, gelijk aan de totale energie, zijnde de som van potentiële en kinetische energie. De potentiële energie kan eenvoudig exact worden uitgedrukt in de waterhoogte. De kinetische energie is het kwadraat van de snelheid, op elk moment geïntegreerd over het vloeistofgebied, bij gegeven potentiaal op het wateroppervlak. Opgemerkt kan worden dat, volgens het principe van Dirichlet, de kinetische energie functionaal minimaal is (alleen) voor de gewenste onsamendrukbare stroming. In plaats van het Laplace probleem in het inwendige gebied (numeriek) op te lossen hetgeen tot het volle 3D golfprobleem zou leiden wordt een consistente en expliciete benadering gemaakt van de kinetische energie door het minimalizeren te beperken tot een deelverzameling van potentialen. Door Klopman e.a. [2010] werd zo een Boussinesq model gemaakt door als deelverzameling te nemen de potentialen die de som zijn van de oppervlakte potentiaal en een combinatie van verticale profielfuncties met ruimte-afhankelijke coefficienten. De minimalizeringseigenschap van de kinetische energie leidt dan tot een elliptisch systeem van vergelijkingen voor de coefficienten. Als verticaal profiel werd een parabool genomen, zoals in de klassieke Boussinesq modellen.

In dit proefschrift zullen we zogenaamde Airy-functies gebruiken; dat zijn functies die optreden in lineaire potentiaaltheorie. Hierdoor is het mogelijk om de parameters van de Airy functies op een optimale manier te kiezen, waardoor golven met een breedbandige spectrum, zoals windgolven, goed berekend kunnen worden. De optimale keuze wordt weer bepaald door de minimaliteitseigenschap van de kinetische energie. Om dit echter praktisch toepasbaar te maken is informatie nodig van het begingolfveld, of van het signaal dat de golven opwekt. Daardoor wordt voor elk probleem een op maat gemaakt model ontworpen, waarvan de dispersie-eigenschappen goed zijn voor alle te beschouwen golven. Zoals bekend maakt de variationele structuur van onze modellen het zeer goed mogelijk om een implementatie met eindige elementen te maken; omdat geen hogere dan eerste-orde afgeleiden in de functionalen voorkomen, kunnen zelfs eenvoudige stuksgewijs lineaire functies gebruikt worden. De kwaliteit van onze modellering wordt getoond aan de hand van simulatieresultaten voor golven met een breed-band spectrum. Simulaties van windgolven worden vergeleken met nauwkeurige metingen van experimenten uitgevoerd op het MARIN. Shoaling, refractie en niet-lineariteit wordt gedemonstreerd aan de hand van simulaties voor het klassieke experiment van Berkhoff. Tenslotte tonen we simulaties van realistische windgolven in de haven van Jakarta. Alle resultaten zijn gepubliceerd in internationale tijdschriften of in proceedings van internationale conferenties.

Chapter 1

Introduction

Summary

In this chapter, we start with a brief review of the challenges in the modelling of surface water waves. Especially when dealing with broad-band waves, e.g. wind-generated waves, the accuracy in dispersiveness and nonlinearity of a surface water wave model becomes very important. Many wave models used in coastal engineering applications are Boussinesq-type models. Since the idea was introduced in 1872 by Boussinesq, the main challenges still remain the same until now: the accuracy in dispersiveness and nonlinearity. In Section 1.2, we will review the development in improving these properties since the beginning until now. Almost all these improved models are rather complicated, e.g. contain higher-order spatial derivatives (at least third-order) and sometimes mixed spatial-temporal derivatives. As a consequence, the complexity in the numerical implementation becomes a serious problem, in particular for two (horizontal) dimensional codes.

In this thesis we will study Boussinesq-type models that are derived via the variational formulation for surface water waves. One of them is the Variational Boussinesq Model (VBM) that was introduced by Klopman et al. [2005, 2007, 2010]. In this model, the vertical variations in the fluid potential are approximated by one or a combination of a priori chosen vertical profiles with spatially dependent functions as coefficient. The vertical profile can be a parabola (inspired by the parabolic shape function in the classical Boussinesq) or a hyperbolic-cosine function which is based on the Airy linear theory. The latter profile will be called the Airy vertical profile. The spatially dependent function has to satisfy a (linear) elliptic equation. The resulting model is quite simple, e.g. the highest spatial derivatives are of second-order and no mixed spatial-temporal derivatives are needed. Moreover, since it is derived with a consistent approximation in the variational structure, the resulting model is energy conserved and has positive Hamiltonian, i.e. sum of potential and kinetic energy. Non-positivity of the Hamiltonian may lead to instabilities. The derivation of the model in the framework of the variational formulation will be described in Section 1.3 and 1.4.

The aim of the work for this thesis is to improve the accuracy in dispersiveness of the VBM. This is needed for simulating broad-band waves, e.g. wind-generated waves. To that end, we extended the approximation in the VBM using a linear combination of a few Airy vertical profiles (up to three profiles). Moreover, since the Airy vertical profile contains a wavenumber as input, the choice of this wavenumber can be optimized to get the best possible dispersiveness. To that end, an optimization criterion to choose the most optimal wavenumber is introduced in Section 1.4.3. This criterion is a minimization of the kinetic energy for a given influx signal (when we deal with signalling problems). The combination of using a few Airy vertical profiles and applying the optimization criterion gives a very significant improvement in the dispersiveness of the model for a given initial signal.

The performance of a Finite Element implementation of the model (the numerical implementation will be described in Chapter 2) for simulating broad-band waves will be illustrated in Section 1.4.4. In this section, the numerical simulations of the model are compared with experimental data from MARIN hydrodynamic laboratory: a focusing wave group and a freak wave experiment. The agreement between the simulations of the model (with 2- and 3- vertical profiles) and the experiments are remarkably accurate. In Section 1.5 we describe the contents of the next chapters in this thesis.

1.1 Surface water wave modelling

Surface water waves, as we see in oceans, seas and lakes, are (in general) generated by wind. The wind that blows above the water surface with certain speed, duration of time and over a certain distance (fetch), strongly influences the generation of the wave. Provided the fetch is long enough and the wind speed is constant, an equilibrium sea-state is eventually reached. Such an equilibrium is called *a fully developed sea* with no significant changes in size and characteristics of the wave. In the fully developed sea, the propagation of the wave is then mainly influenced by the Earth's gravity as a restoring force.

The wind-generated waves usually have a chaotic (irregular) form. Mathematically, this irregular form can be approximated as a sum of (infinitely) many wave components, i.e. monochromatic waves, as in Fourier theory. This leads to the concept of amplitude spectrum (see Chapter 3 of Holthuijsen [2007]). In Figure 1.1, the narrowest spectrum corresponds to a monochromatic wave (upper plot), a rather narrow spectrum corresponds to rather regular waves (middle plot), and the wider (broad) spectrum corresponds to irregular waves (lower plot). This spectrum shows how the wave energy is distributed over the frequencies. In middle and lower plot of Figure 1.1, we use random phases. Wind-generated waves have a spectrum as in the lower plot of Figure 1.1. Intuitively, modelling of such broad-band waves is more challenging than the regular waves in the upper and middle plot of Figure 1.1.

Understanding the characteristics of waves has been a challenge for wave modellers. Some motivations for understanding the characteristics are as follows.

- How to reduce ship accidents due to unpredictable waves, e.g. extreme wave conditions.

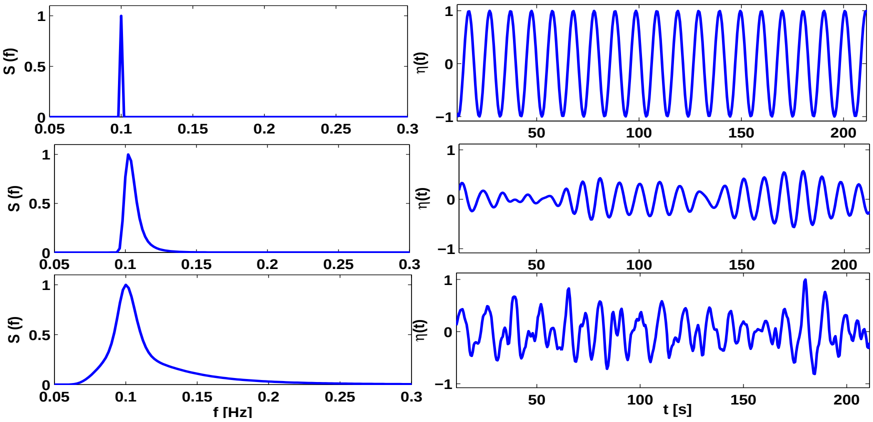

Figure 1.1: *Characters of waves (right part) based on the width of their spectrum (left part).*

- How to optimize a harbour design by analyzing its response to average or extreme wave conditions.
- How to analyze the response of offshore oil and gas platforms to extreme wave conditions.

Using mathematical physics, modelling of surface water waves contributes to solve (at least to understand) the problems above.

Water wave models can be classified into two categories, based on properties of the waves to be considered:

Phase-averaged models: the wave conditions are described in average characteristics. In this category, the energy spectrum is modelled, while the phase is considered to be uniformly distributed between $[0, 2\pi]$. As a consequence, the details of the time series of the wave motion are lost. This model is typically used for studying the generation of waves by wind on the ocean and the wave propagation from the open sea to the coast.

Phase-resolving models: individual waves (wave components) in the energy spectrum are resolved with their phases and amplitudes. This model is typically used for studying wave propagation in a small area, such as in a harbour or near coasts.

Phase-resolving models can also be divided into two categories based on dimension of variables in the model. The first category is *the Three-dimensional (3D) wave model*. In this category, variables involved in the model depend on 3 dimensional coordinates, e.g. as functions of (x, y, z). Since the model depends on the full 3D coordinates, the computational effort is rather costly for solving large problems such as waves in a harbour. Therefore, this model is usually used for studying small problems, e.g. the response of a ship to colliding waves. The second category are *the Two-Horizontal Dimensional (2HD) models*. In this category, vertical variations of the flow are approximated to eliminate the dependence on the vertical coordinate. Since a dimension reduction (from 3D to 2D) is applied in this category, the computational capability increases. Therefore, this type of model is more applicable for simulating wave propagation in larger domains, such as waves in the coastal area.

Most of the 2HD phase-resolving models that are used in coastal engineering applications are *Boussinesq-type models*. This thesis focuses on the modelling of one variant of Boussinesq model. In the following section, we will review the development of the Boussinesq models and their main challenges.

1.2 Boussinesq-type models

The main issue behind the modelling of water waves from the full 3D problem to 2HD models is to reduce the computational cost by reduction of the vertical dimension while preserving two important properties of water waves:

Dispersiveness is determined by the accuracy in *the dispersion relation* which connects the angular frequency $\omega = 2\pi/T$ (T is the wave period) to the wavenumber $k = 2\pi/\lambda$ (λ is the wavelength). This relation will be described in detail in Section 1.4.2.

Nonlinearity becomes important if the waves have large amplitude. Nonlinearity expresses the interactions as energy exchange between wave components in the energy spectrum.

The original formulation of the now-called Boussinesq models was introduced by Boussinesq [1872] for wave propagation over a constant water depth. It is actually the first correction of the nonlinear shallow water equations to the weakly dispersive (with $kh << 1$) and the weakly nonlinear (with $a/h << 1$) water wave model. Here, kh is the relative water depth, where k and h are the wavenumber and the water depth respectively, and a/h is the relative amplitude, where a is the wave amplitude. The original formulation of Boussinesq was achieved by introducing a polynomial expansion of the vertical variation in the horizontal velocity. The formulas were expressed in terms of depth-averaged velocity and were derived for low-order expansion by assuming $a/h = O\left((kh)^2\right)$ and retaining terms of order $O((kh)^2)$. Since 1953, initiated by the work of Serre [1953], the modelling of the extended version of the original formula to higher order models received much attention from wave modellers.

The popularity of Boussinesq-type models in coastal engineering applications started by the works of Mei and Méhauté [1966], who extended the classical formula into variable depth in 1D, and Peregrine [1967] in 2D. Peregrine presented the equations in alternative velocity variables, namely the horizontal velocity at the sea bed and at the still water. The quality of these models was still quite poor both in dispersion and in nonlinearity, but these works initiated the first computer model simulation (in Peregrine [1967]). Since 1978 by Abbott et al. [1978] and followed by Madsen and Warren [1984] and Schaper and Zielke [1984], the focus of the applications of Boussinesq-type models shifted from long waves (Solitary and Cnoidal waves) to nonlinear irregular waves.

The applications of Boussinesq-type models were limited by the weak dispersion property. Rather noticeable Boussinesq-type models in the 90's that triggered another development of the ideas in improving the dispersion and nonlinear properties are the enhanced Boussinesq model of Madsen et al. [1991] and Madsen and Sørensen [1992], and the extended Boussinesq model of Nwogu [1993]. Madsen et al [1991] used the idea of Witting [1984], who introduced the concepts of Padé approximant within differential equations in the framework of conventional Boussinesq equations. This resulted in a new set of low-order equations with dispersion characteristics corresponding to Padé$[2,2]$. The equations were expressed in depth-integrated velocity and later, Madsen and Sørensen [1992] applied this idea for uneven bottom. The other Boussinesq-type model is derived differently by Nwogu [1993] who uses the velocity at a depth z_α to be determined by choice of a parameter α. He optimized the choice of z_α to get the best possible dispersion relation. As it turns out $\alpha = -0.39$ (which corresponds to a depth $z_\alpha = 0.531h$) gave the best dispersion relation for the model. The free coefficient was chosen to match Padé$[2,2]$. Interestingly, for $\alpha = -0.3$ this formula gave the same quality of dispersion relation as the classical Boussinesq and $\alpha = -0.4$ for the Boussinesq-type model of Madsen and Sørensen [1992].

The ideas behind the derivation of these Boussinesq-type models received more attention in improving the quality of dispersion relation and nonlinearity by extending the approximation in the power series of the vertical variation into higher order, see Wei et al. [1995], Madsen and Schäffer [1998], Agnon et al. [1999], Zou [2000] and Kennedy et al. [2001]. The most recent results of Madsen et al. [2002, 2003] have high accuracy both in dispersion and nonlinearity up to $kh = 25$. But the high order approximation introduces high order derivatives and many terms in continuity and momentum equations. The latest model of Madsen et al. [2002, 2003] included *fifth-order derivatives* to get the best possible dispersion. As it turns out, the complexity in the numerical implementation becomes unavoidable, and the complexity increases when the models are generalized for 2HD.

Motivated by the complexity of the higher-order Boussinesq-type equations, especially in the higher order derivatives, Lynett and Liu [2004a] introduced a different approach to obtain a higher-order depth-integrated model. Instead of employing a high-order polynomial for the vertical distribution of the flow field, two quadratic polynomials are used and matched at an interface that divides the water into two layers. They called this method *the two-layer approach*. The optimized model showed good linear characteristics up to $kh \approx 6$ while maintaining the maximum order of differentiation at three. In Lynett and Liu [2004b], the two-layer approach is generalized to multi-layers by considering three, four, and five layers. The achievement in the quality of dispersion relation is quite impressive: for three-layers the model is accurate up to $kh \approx 17$ and four-layers up to $kh \approx 30$.

A rather different approach for deriving Boussinesq-type equations is via the variational formulation. Motivated by the complexity of high-order Boussinesq-type models, Klopman et al. [2005, 2007, 2010] introduced a variational Boussinesq-type modelling for describing long wave propagation from shallow to intermediate depth. They called this model *the Variational Boussinesq Model (VBM)*. In the framework of the variational formulation for surface water waves, the idea is to approximate the fluid potential $\Phi(\mathbf{x}, z, t)$ in the expression of kinetic energy with a sum of the surface fluid potential

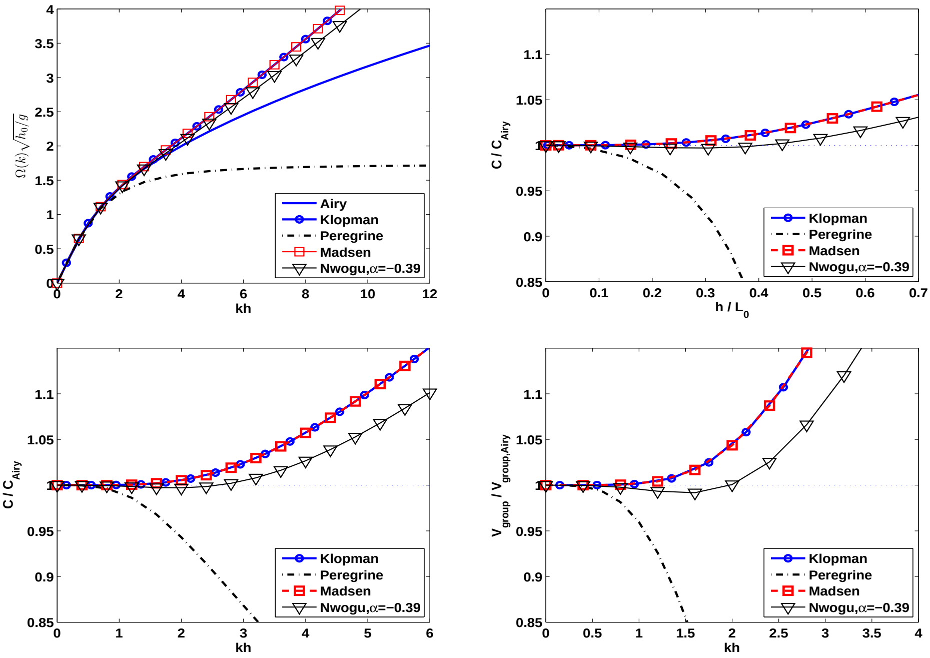

Figure 1.2: *Comparison of Boussinesq-type models by Klopman et al. [2010], Peregrine [1967], Madsen and Sørensen [1992], Nwogu [1993] with the Airy linear theory dispersion relation (upper left), ratio of the phase velocity of the models with the phase velocity of Airy linear theory as functions of h/L_0 (upper right) and relative depth kh (lower left), and ratio of the group velocity of the models with the group velocity of Airy linear theory (lower right).*

$\phi(\mathbf{x}, t) = \Phi(\mathbf{x}, z = \eta, t)$ and a multiplication of a vertical profile $F(z)$ (to be chosen a priori) and a spatially dependent function $\psi(\mathbf{x}, t)$ as coefficient. The function ψ is chosen in an optimal way by minimizing the kinetic energy function with respect to ψ, which leads to a linear elliptic equation. In Klopman et al. [2010], three types of vertical profiles are suggested: a normalized parabolic profile, an Airy profile (hyperbolic-cosine functions) and a power series profile, but mainly the parabolic profile (valid for rather long waves) was used for simulations.

Compared to the other Boussinesq-type models, the VBM is relatively simple and much easier for numerical implementation since the highest derivative in the equations is just of second order. Furthermore, there are no mixed spatial-temporal derivatives. Since this model is derived with a consistent approximation in the variational structure, the resulting model is energy conserved and has positive Hamiltonian, i.e. sum of potential and kinetic energy. Non-positivity of the Hamiltonian may lead to instabilities (see Broer [1974], Broer et al. [1976], Milder [1990] and Yoon and Liu [1994]). The higher-order Boussinesq models previously introduced are non-Hamiltonian. In Fuhrman and Madsen [2008], they added an artificial damping to keep the numerical model (high-order Boussinesq) stable.

Interestingly, by choosing a parabolic profile as the vertical profile, the VBM with parabolic profile gives exactly the same quality of dispersion relation as the enhanced Boussinesq model of Madsen and Sørensen [1992] (regardless how the two models were derived) and slightly less accurate than the model of Nwogu [1993] (with $\alpha = -0.39$). We illustrate the quality of various models in Figure 1.2. To that end, we use the relative water depth kh and relative depth $D_0 = h/L_0$ where L_0 is the wavelength. The shallow water regime is usually associated with $D_0 \leq \frac{1}{25}$, the intermediate/transitional water with $\frac{1}{25} \leq D_0 \leq \frac{1}{2}$ and the deep water with $D_0 > \frac{1}{2}$. In the upper left part of Figure 1.2, the dispersion relation of Madsen and Sørensen [1992], Nwogu [1993], Peregrine [1967], Klopman et al. [2010] (the VBM with parabolic profile) and the exact dispersion relation (based on Airy linear theory given by (1.21) in Section 1.4.2) are compared. In the upper right part the ratio of the phase velocity of the models with the exact phase velocity are compared as a function of h/L_0. In the lower part of Figure 1.2, the ratio between the phase (left plot) and the group (right plot) velocities with the exact velocities are shown as functions of relative water depth kh. All models (except Peregrine [1967]) are able to simulate waves propagation from shallow water to intermediate water with errors in phase and group velocities less than 5%. The model of Nwogu [1993] has a good phase velocity up to $kh \approx 3$ and the group velocity up to $kh \approx 2.5$.

The focus of this thesis is to improve the quality of the dispersion relation of the original VBM of Klopman et al. [2010] for simulating waves with broad spectra, such as focusing wave groups or irregular waves. To that aim, as suggested by Klopman et al. [2010], the improvement can be achieved by taking more vertical profiles in the approximation of the fluid potential $\Phi(\mathbf{x}, z, t)$ in the kinetic energy using a few Airy profiles (in this thesis, up to three profiles). Furthermore, the choice for the wavenumber in the Airy profile is obtained in an optimal way by minimizing the kinetic energy for a given influx signal. This optimization criterion can also be applied for varying bottom. In the previously mentioned Boussinesq-type models, the dispersiveness is measured by the largest relative water depth kh until which a certain accuracy is achieved. This then holds for any simulation in this interval. With the optimization criterion for the VBM, instead of achieving a larger value of kh, the Optimized VBM (OVBM) will give the highest desired accuracy in the dispersiveness for the waves that have to be simulated for a given influx signal: the model (i.e. the dispersion) depends on the problem to be solved.

Besides improving the dispersiveness of the VBM, for numerical implementation, we choose the Finite Element Method (FEM) as a numerical solver. In Klopman et al. [2005, 2007, 2010], the model was implemented with a pseudo-spectral method on (regular) rectangular grids. A limitation of this implementation is a lack of flexibility when dealing with complicated domains such as harbours or complicated coastlines. Also, to reduce the computational cost, the use of unstructured (triangular) grid in the FEM gives more flexibility compared to, e.g. curvilinear meshes and nested grids. Besides this, since the model was derived via the variational formulation, it is natural to choose the FEM as the numerical implementation. This implementation will be described in Chapter 2.

In Section 1.3, we first discuss the dynamic equations for surface water waves, followed by an introduction of the variational principle for water wave modelling. Within this framework, it can be shown that the principle of minimization of energy is equivalent with the full 3D Laplace problem for water waves. Consistent approximations in the

Hamiltonian can be introduced, while preserving consequences of the exact formulation, e.g. energy conservation. By restricting the problem to a certain wave class, an approximation for the VBM will be introduced in Section 1.4. An optimization criterion for the Airy vertical profile will be discussed in Section 1.4.3.

1.3 Dynamic equations and Variational principle

We consider water as a fluid layer that is inviscid and incompressible with uniform mass density $\rho = 1$ kg/m^3. The fluid layer is assumed to be bounded below by an impermeable bottom and above by a free surface, while horizontal directions run from $-\infty$ to ∞. At the free surface, we assume there is no surface tension, no wind or other forces, so the Earth's gravity is the only restoring force to force back the free surface into its equilibrium position. Furthermore, the flow of the fluid is assumed to be irrotational. This is a common assumption for surface water waves.

We use the following notational conventions. We consider three dimensional space Cartesian coordinate system, two horizontal directions $\mathbf{x} = (x, y)$, and vertical z-axis. The gravitational acceleration g has direction opposite to the z-axis. The fluid region is bounded below by an impermeable bottom at $z = -h\left(\mathbf{x}\right)$ and above at the surface elevation $\eta\left(\mathbf{x}, t\right)$, where t denotes time. The fluid velocity in the interior is denoted by $\mathbf{U}$. By assuming irrotational flow, where $\nabla \times \mathbf{U} = 0$, a fluid potential $\Phi(\mathbf{x}, z, t)$ is related to $\mathbf{U}$ by $\mathbf{U} \equiv \nabla_3\Phi = (\nabla\Phi, \partial_z\Phi)$. Here, ∇ is the horizontal gradient and ∂_z denotes the partial derivative with respect to z and likewise ∂_t with respect to time t.

By combining the incompressibility condition ($\nabla \cdot \mathbf{U} = 0$) and the irrotationality condition above, one get the Laplace equation for surface water waves. The governing equations and boundary conditions for idealized conditions mentioned above are as follows:

$$\nabla_3 \cdot \nabla_3\Phi = 0, \qquad \text{for } -h < z < \eta \tag{1.1}$$

$$\nabla_3\Phi \cdot N_b = 0, \qquad \text{at } z = -h \tag{1.2}$$

$$\nabla_3\Phi \cdot N_s = \partial_t\eta, \qquad \text{at } z = \eta \tag{1.3}$$

$$\partial_t\Phi + \frac{1}{2}\left|\nabla_3\Phi\right|^2 + g\eta = 0, \qquad \text{at } z = \eta \tag{1.4}$$

Here, normal direction vectors are used: $N_b = (-\nabla h, -1)$ and $N_s = (-\nabla\eta, 1)$. The equation in the interior (1.1) is the Laplace equation, which represents the continuity equation. Equation (1.2) represents the impermeability condition at the bottom. The kinematic free surface condition is equation (1.3), stating that the fluid will remain below the free surface η. The dynamic boundary condition is equation (1.4) that the pressure (described by the Bernoulli equation) at the free surface is constant. The governing equations and boundary conditions above are usually called *the full 3D surface wave equations*.

In the classical derivation of Boussinesq-type models (see Kirby [1997] and Madsen and Fuhrman [2010] for reviews), usually, the velocity potential $\Phi(\mathbf{x}, z, t)$ is represented as a power series in the vertical coordinate, i.e.

$$\Phi\left(\mathbf{x}, z, t\right) = \Sigma_0^\infty (h + z)^n \phi^{(n)}\left(\mathbf{x}, t\right)$$

where $\phi^{(n)} = \frac{\partial^n \Phi}{\partial z^n}|_{z=0}$. With this representation, a dimension reduction (3D to 2HD) is achieved. This approximation is then inserted into the governing equations (1.1), while also introducing velocity-type variables. High-order Boussinesq-type models usually refer to how many terms in the power series are taken into account. This high-order expansion leads to higher-order derivatives in a resulting Boussinesq-type model.

Instead of following the classical approximation of Boussinesq-type models above, a different approach via the variational principle can be applied to get a Boussinesq-type model. This approach is motivated by the observation that the mathematical-physical description of surface water waves has a Hamiltonian structure. This observation has been made by Zakharov [1968], Broer [1974] and Miles [1977] (see also Milder [1977]).

To that end, we will first introduce Luke's variational principle for surface water waves, then show that this variational principle is equivalent to a Hamiltonian structure. Luke [1967] formulated an expression for the pressure as the Lagrangian $\mathcal{L}(\Phi, \eta)$

$$\mathcal{L}\left(\Phi, \eta\right) = -\int_t \int_{\mathbf{x}} \int_{-h}^{\eta} \left[\partial_t \Phi + \frac{1}{2}\left|\nabla_3 \Phi\right|^2 + gz\right] dz d\mathbf{x} dt \tag{1.5}$$

which describes inviscid, incompressible homogeneous fluid, with irrotational flow. He showed that the full 3D surface wave equations (1.1 - 1.4) can be obtained by vanishing of the first variations of (1.5) with respect to Φ and η. More precisely, vanishing of the first variation of (1.5) with respect to variations $\delta\Phi$ in Φ leads to

$$\int_t \left\{\int_{\mathbf{x}} \int_{-h}^{\eta} \left[\partial_t \left(\delta\Phi\right) + \nabla_3 \Phi \cdot \nabla_3 \left(\delta\Phi\right)\right] dz d\mathbf{x}\right\} dt = 0 \tag{1.6}$$

Now, we apply Leibniz's integral rule for the first term of (1.6)

$$\partial_t \int_{-h}^{\eta} \delta\Phi dz = \int_{-h}^{\eta} \partial_t \left(\delta\Phi\right) dz + \left(\delta\Phi\right)|_{z=\eta} \partial_t \eta + \left(\delta\Phi\right)|_{z=-h} \partial_t h$$

and Green's theorem (integration by parts) for the second term of (1.6)

$$\int_{\mathbf{x}} \int_{-h}^{\eta} \nabla_3 \Phi \cdot \nabla_3 \left(\delta\Phi\right) dz d\mathbf{x} = -\int_{\mathbf{x}} \int_{-h}^{\eta} \nabla_3 \cdot \nabla_3 \Phi (\delta\Phi) dz d\mathbf{x} + \int_{\mathbf{x}} \left(\delta\Phi\right) \partial_n \Phi|_{z=-h}^{z=\eta}$$

Here, the lateral boundaries have been neglected. Then vanishing for all variations $\delta\Phi$, we obtain the Laplace equation (1.1) in the interior, the impermeability condition at the bottom (1.2) and the kinematic free surface condition (1.3). The dynamic boundary condition (1.4) can be obtained by vanishing of the first variations of (1.5) with respect to variations $\delta\eta$ in η.

Now we will show the relation between the Lagrangian $\mathcal{L}\left(\Phi, \eta\right)$ (1.5) and its Hamiltonian representation. To that end, we use the surface potential $\phi(\mathbf{x}, t) = \Phi(\mathbf{x}, z = \eta(\mathbf{x}, t), t)$ and the surface elevation $\eta(\mathbf{x}, t)$ as the canonical variables for the Hamiltonian representation. Following Miles [1977], the Lagrangian $\mathcal{L}\left(\Phi, \eta\right)$ (1.5) can be reformulated as

$$\begin{aligned} \mathcal{L}\left(\Phi, \eta\right) &= -\int_t \int_{\mathbf{x}} \int_{-h}^{\eta} \left[\partial_t \Phi + \frac{1}{2}\left|\nabla_3 \Phi\right|^2 + gz\right] dz d\mathbf{x} dt \\ &= \int_t \left[\begin{array}{c} \int_{\mathbf{x}} \phi \partial_t \eta d\mathbf{x} - \int_{\mathbf{x}} \left\{\int_{-h}^{\eta} \frac{1}{2}\left|\nabla_3 \Phi\right|^2 dz + \frac{1}{2} g \left(\eta^2 - h^2\right)\right\} d\mathbf{x} dt \\ -\partial_t \int_{\mathbf{x}} \int_{-h}^{\eta} \Phi dz d\mathbf{x} \end{array} \right] dt \end{aligned} \tag{1.7}$$

by using Leibniz's integral rule

$$\partial_t \int_{-h}^{\eta} \Phi dz = \int_{-h}^{\eta} \partial_t \Phi + \phi \partial_t \eta + \Phi|_{z=-h} \partial_t h.$$

By dropping dynamically uninteresting terms, i.e. the volume integral Φ itself and the horizontal-space integral: $\int_t \partial_t \int_{\mathbf{x}} \int_{-h}^{\eta} \Phi dz d\mathbf{x} dt$ and $\int_t \int_{\mathbf{x}} \frac{1}{2} g h^2 d\mathbf{x} dt$ respectively, the Lagrangian (1.7) can be rewritten as

$$\mathcal{L}(\phi, \eta) = \int_t \left[\int_{\mathbf{x}} (\phi \partial_t \eta) \, d\mathbf{x} - \mathcal{H}(\phi, \eta) \right] dt \tag{1.8}$$

Here, $\mathcal{H}(\phi, \eta)$ is the Hamiltonian or the total energy. Just as in Classical Mechanics, it is the sum of the potential energy $P = \frac{1}{2} \int_{\mathbf{x}} g \eta^2 d\mathbf{x}$ and the kinetic energy

$$\mathcal{K}(\phi, \eta) = \min_{\Phi} \left\{ K(\Phi, \eta) \, | \Phi = \phi \text{ at } z = \eta \right\} \tag{1.9}$$

with

$$K(\Phi, \eta) := \frac{1}{2} \int_{\mathbf{x}} \int_{-h}^{\eta} |\nabla_3 \Phi|^2 \, dz d\mathbf{x}. \tag{1.10}$$

Note that condition (1.9) leads to the requirement of the fluid potential Φ to satisfy the Laplace equation in the interior (1.1), the bottom impermeability condition (1.2) and the condition $\Phi = \phi$ at the free surface. So definition (1.9) implies the validity of the 3D surface wave equations (1.1 - 1.3). Recapitulating so far, the Lagrangian $\mathcal{L}(\phi, \eta)$ has been represented in surface variables only, i.e $\phi(\mathbf{x}, t)$ and $\eta(\mathbf{x}, t)$. This concludes that a dimension reduction (3D to 2HD) has been achieved.

Now, by taking variations of (1.8) with respect to η and ϕ, the Hamiltonian system is found

$$\partial_t \eta - \delta_\phi \mathcal{H} = 0, \quad \partial_t \phi + \delta_\eta \mathcal{H} = 0 \tag{1.11}$$

where $\delta_\phi \mathcal{H}$ and $\delta_\eta \mathcal{H}$ denote the variational derivatives of $\mathcal{H}$ with respect to ϕ and η respectively. This can be recognized as the *canonical action principle*, the generalization of similar principles in Classical Mechanics to infinite dimensions with canonical variables η as 'position' and ϕ as 'momentum' (see van Groesen et al. [2010] and chapter 6.3 in van Groesen and Molenaar [2007]).

The potential energy P is already expressed explicitly in the surface variable η. Unfortunately this is not the case for the kinetic energy. This is actually the essential problem in the variational formulation for surface wave theory to achieve the dimension reduction. Nevertheless, an approximate model can be obtained by taking an appropriate approximation in the kinetic energy. This approximate model will share consequences of the variational form, such as energy conservation.

Two extreme approximations, the Shallow Water Equations (SWE) and the Linear (Airy) wave theory, can be obtained by taking specific assumptions when restricting the waves to a certain wave class. The SWE can be obtained by assuming that the wavelength is much larger than the depth of the water so the variations in the vertical direction can be ignored completely. As a result, the dispersive effects are ignored. This can be achieved by taking $\Phi = \phi$ in the expression of the kinetic energy (1.10). Inserting this approximation into the Hamiltonian equations (1.11) results in the Hamiltonian equations for the SWE:

$$\begin{cases} \partial_t \eta & = -\nabla \cdot \left[(h+\eta) \nabla \phi \right] \\ \partial_t \phi & = -g\eta - |\nabla \phi|^2 / 2 \end{cases} \tag{1.12}$$

For the other extreme approximation, linear wave theory, it is assumed that the bottom variations and the surface elevations are small compared to others dimensions. As a result, all nonlinear effects are ignored, but the model has the exact dispersion relation (see Subsection 1.4.2).

Notice that SWE ignores completely dispersive effects but is exact in the nonlinearity (no assumption is made regarding the nonlinearity). Opposite to this, the linear wave theory models the dispersion exactly but completely neglects the nonlinearity. In coastal engineering applications, Boussinesq-type models are usually preferred above these two 'extreme' approximations since in their approximation, the dispersion and nonlinear effects are taken into account.

In the next section, we derive a Boussinesq-type model in the framework of the variational principle: the Variational Boussinesq Model (VBM). This can be obtained by restricting the wave problem to a certain wave class. Instead of achieving large value for relative depth kh for the accuracy in dispersiveness as other Boussinesq-type models, the resulting model will be optimized to have the best possible accuracy in dispersiveness for a given wave problem. In other words, the optimized model will be case-dependent.

1.4 The Variational Boussinesq Model

The motivation behind the modelling of the Variational Boussinesq Model (VBM) is to construct a Boussinesq-type model that has a positive Hamiltonian and the resulting model has to be simple for numerical implementation, i.e. has low order spatial derivatives and no mixed spatial-temporal derivatives. As introduced in Klopman et al. [2005, 2007, 2010], this leads to the idea to directly apply a Ritz method for the vertical structure of the fluid potential $\Phi(\mathbf{x}, z, t)$:

$$\begin{aligned} \Phi(\mathbf{x}, z, t) &= F_0(z)\psi_0(\mathbf{x}, t) + F_1(z)\psi_1(\mathbf{x}, t) + \cdots + F_M(z)\psi_M(\mathbf{x}, t) \\ &= \Sigma_{m=0}^{M} F_m(z)\psi_m(\mathbf{x}, t) \end{aligned} \tag{1.13}$$

where $F_m(z)$ are vertical shape functions and $\psi_m(\mathbf{x}, t)$ are spatially dependent functions that have to be determined. If this approximation is substituted directly into the kinetic energy functional (1.10), the positivity of the Hamiltonian is achieved. The Hamiltonian system has now additional constraints: $\delta_{\psi_m}\mathcal{H} = 0$ for $m = 0, \cdots, M$, where $\delta_{\psi_m}\mathcal{H}$ denotes the variational derivatives with respect to ψ_m. Since in general, these additional constraints introduce time derivatives for all parameters $\psi_m(\mathbf{x}, t)$ in the resulting dynamical equations, the canonical structure of the Hamiltonian system (1.11) is lost. However, by requiring **only one term** to be nonzero at the free surface $z = \eta(\mathbf{x}, t)$, i.e. $F_0(z = \eta)\psi_0(\mathbf{x}, t) = \phi(\mathbf{x}, t)$ and the rest to be zero: $F_m(z = \eta)\psi_m(\mathbf{x}, t) = 0$ for $m = 1, \cdots, M$, the canonical structure of the Hamiltonian system (1.11) is regained. Hence, $F_0(z = \eta) = 1$ and $F_m(z = \eta) = 0$ for $m = 1, \cdots, M$ are required to keep the canonical structure (1.11).

1.4.1 The VBM with multiple profiles

As introduced in Klopman et al. [2005] for 1D model, Klopman et al. [2007] for 2D model and more specific cases in Klopman et al. [2010], the VBM can be obtained by approximating the vertical structure in the fluid potential Φ in the kinetic energy functional (1.10). To that end, in order to construct a model with a positive Hamiltonian without destroying its canonical structure, the fluid potential Φ is approximated by:

$$\Phi\left(\mathbf{x},z,t\right)\approx\phi\left(\mathbf{x},t\right)+\Sigma_m F_m\left(z;\eta,h\right)\psi_m\left(\mathbf{x},t\right)=\phi+F\cdot\Psi \tag{1.14}$$

where F and Ψ are vector functions. To keep the canonical structure of the Hamiltonian (1.11), the condition $\phi\left(x,t\right)=\Phi\left(x,z=\eta,t\right)$ has to be assured, and it is required that $F_m|_{z=\eta}=0$ for any m. The bottom impermeability condition (1.2) requires $\nabla_3\Phi\cdot N_b=0$ with $N_b=-(\nabla h,1)$ at $z=-h$. Here, we assume the bottom is slowly varying, so that the requirement $\partial_z F_m|_{z=-h}=0$ is sufficiently accurate.

The vertical profiles F_m have to be chosen in advance, while ψ_m is chosen in the optimal way by minimizing the kinetic energy, with respect to ψ_m. In Klopman et al. [2010], one parabolic vertical profile

$$F^{(p)}\left(z;\eta,h\right)=\frac{1}{2}\frac{\left(z+h\right)^2-\left(\eta+h\right)^2}{\left(h+\eta\right)}=\frac{1}{2}\left(z-\eta\right)\frac{\left(2h+z+\eta\right)}{\left(h+\eta\right)} \tag{1.15}$$

is used. This is inspired by the parabolic shape function of the classical Boussinesq and valid only for long waves (see Figure 1.2). In this thesis, we will only work with the hyperbolic-cosine functions

$$F_m\left(z;\eta,h\right)=\frac{\cosh\left(\kappa_m\left(z+h\right)\right)}{\cosh\left(\kappa_m\left(\eta+h\right)\right)}-1 \tag{1.16}$$

which are based on the Airy linear theory (see Subsection 1.4.2). This vertical profile will be referred as Airy profile for the rest of this thesis.

Now, substituting the approximation of Φ of VBM (1.14) into the kinetic energy functional (1.10) results in

$$\begin{aligned}
K_{vbm}&=\frac{1}{2}\int_{\mathbf{x}}\int_{-h}^{\eta}\left|\nabla\phi+\nabla\left(F\cdot\Psi\right)\right|^2+\left(\partial_z F\cdot\Psi\right)^2dzd\mathbf{x}\\
&=\frac{1}{2}\int_{x}\left[\int_{-h}^{\eta}\left|\nabla\phi+F\cdot\nabla\Psi+\Psi\cdot\nabla F\right|^2+\left(\partial_z F\cdot\Psi\right)^2dz\right]d\mathbf{x}\\
&\approx\frac{1}{2}\int\left[\int_{-h}^{\eta}\left|\nabla\phi+F\cdot\nabla\Psi\right|^2+\left(\partial_z F\cdot\Psi\right)^2dz\right]d\mathbf{x}
\end{aligned} \tag{1.17}$$

In the third line, we use the *weakly-nonlinear* variant of the VBM (as defined in Klopman et al.[2005]) where the effects of $\nabla F=\left(\partial_\eta F\nabla\eta+\partial_h F\nabla h+\partial_{\kappa_m}F\nabla\kappa_m\right)$ are neglected. Taking this term into the approximation will produce the *fully-nonlinear* model, without approximation for the nonlinearity. Klopman et al. [2005] argued that neglecting the term $\partial_\eta F\nabla\eta$ will produce unsatisfactory performance. This was shown in the comparison with the high-accuracy Rienecker and Fenton [1981] when they used the VBM with parabolic profile. In all cases that we will deal with, the *weakly-nonlinear* model of the VBM (using Airy profiles) is accurate enough to describe the nonlinear effects for cases such as focusing wave groups, irregular waves, and freak-type of waves. In this thesis, we therefore limit ourself to the *weakly-nonlinear* model (to be referred to as nonlinear VBM in the rest of this thesis) and focus ourself to improve the linear dispersion of the model.

For simplicity, we introduce matrices α and γ, and a vector β which have elements that depend on the vertical profiles F_m

$$\alpha_{ij} = \int_{-h}^{\eta} F_i F_j dz; \quad \gamma_{ij} = \int_{-h}^{\eta} F_i' F_j' dz; \quad \beta_i = \int_{-h}^{\eta} F_i dz \tag{1.18}$$

The explicit formulas for these coefficients for F_m the Airy profiles (1.16) are given in the Appendix of Chapter 3. Using this notation, the kinetic energy (1.17) can be rewritten as

$$K_{vbm} = \frac{1}{2} \int_{\mathbf{x}} \left[(h+\eta) \left|\nabla\phi\right|^2 + 2\nabla\phi\beta \cdot \nabla\Psi + \nabla\Psi \cdot \alpha\nabla\Psi + \Psi \cdot \gamma\Psi \right] d\mathbf{x} \tag{1.19}$$

By substituting this expression into the Lagrangian (1.8), we obtain

$$\mathcal{L}_{vbm}(\phi, \eta, \psi_m) = \int \left[\int \phi\partial_t\eta - \mathcal{H}_{vbm}(\phi, \eta, \psi_m) \right]$$

where $\mathcal{H}_{vbm}(\phi, \eta, \psi_m)$ is the approximate Hamiltonian for the VBM. Note that the new approximate Hamiltonian $\mathcal{H}_{vbm}$ now also depends on ψ_m. Taking variations of $\mathcal{H}_{vbm}$ with respect to η and ϕ, leads to the dynamic forms as in (1.11), and variations with respect to ψ_m results in a system of linear elliptic equations:

$$\begin{cases} \partial_t\eta & = -\nabla \cdot \left[(h+\eta)\nabla\phi\right] - \nabla \cdot \left[\beta \cdot \nabla\Psi\right] \\ \partial_t\phi & = -g\eta - \left|\nabla\phi\right|^2/2 \\ -\nabla \cdot \left[\alpha\nabla\Psi\right] + \gamma\Psi & = \nabla \cdot \left[\beta\nabla\phi\right] \end{cases} \tag{1.20}$$

Klopman et al. [2005, 2007, 2010] used the 'velocity' $u(\mathbf{x},t)=\nabla\phi$ rather than the surface potential ϕ. In this thesis, we will work with the surface potential ϕ (as in (1.20)) to reduce the size in numerical computations.

1.4.2 Linear dispersion relation

For linear waves of finite amplitude that propagate above a constant depth h_0, the (linear) *dispersion relation*, denoted by $\omega = \Omega(k)$, connects the angular frequency $\omega = 2\pi/T$, where T is the wave period, with the wavenumber $k = 2\pi/\lambda$, where λ is the wavelength. From the Airy linear theory for infinitesimal small waves, the solution for the velocity potential Φ is given by

$$\Phi(\mathbf{x}) = \int \widehat{\phi}(\mathbf{k}) \frac{\cosh(k(z+h))}{\cosh(kh)} e^{i\mathbf{k}.\mathbf{x}} d\mathbf{k}$$

where $\mathbf{k} = (k_x, k_y)$ is the 2D wave vector with $k = |\mathbf{k}|$ and $\hat{\phi}$ is the Fourier transform of ϕ. By using this solution, the exact dispersion relation is given by

$$\Omega_{Airy}(k) = c_0 k \sqrt{\frac{\tanh(kh_0)}{kh_0}} \text{ with } c_0 = \sqrt{gh_0} \tag{1.21}$$

where c_0 is the speed of long waves. An individual wave (one frequency) will propagate with the so-called *phase velocity* (or wave celerity) which is defined as $c = \omega/k$ in 1D and $\underline{C}_p = c\bar{e}_k$ with $\bar{e}_k = \mathbf{k}/|\mathbf{k}|$, in 2D, while a wave package will propagate with the so-called *group velocity* (or energy velocity) which is defined as $V = \partial\Omega(k)/\partial k$ in 1D and $\underline{V}_g = V\bar{e}_k$ in 2D.

Notice that the limiting cases of (1.21) are $c_0 k$ for $h \to 0$ (the shallow water limit) and $k\sqrt{g|k|}$ for $h \to \infty$ (the deep water limit).

In constructing a wave model, the first property that has to be investigated is the dispersion relation of the model. This is because the accuracy in dispersion relation (compared to the exact relation (1.21)), will affect other properties such as effects of nonlinearity, shoaling, diffraction and refraction. In modelling water waves, many efforts have been made to obtain models with accurate dispersion relation. One procedure to obtain such model is to introduce polynomial expansions for the exact dispersion relation (1.21) near a certain wavenumber k, e.g. $k \to 0$. The resulting model is then transformed back to the real space from Fourier space. But high-order polynomial expansions in k (Fourier space) correspond to high-order spatial derivatives in real space, according to the relation $(ik)^n \Longleftrightarrow (\partial_x)^n$. As a consequence, high-order polynomial expansions result in high-order derivatives in the resulting model. Moreover, the dispersion relation of the resulting model is usually only valid near a certain wavenumber, which is commonly taken to be $k = 0$.

Now we will investigate the dispersion relation of the VBM. From (1.20), the VBM with multiple profiles has dispersion relation that (strongly) depends on the choice of the vertical profile(s). The VBM-dispersion is given by

$$\Omega_{vbm}(k) = c_0 k \sqrt{1 - \frac{k^2}{h_0} \beta \cdot \left(\alpha k^2 + \gamma\right)^{-1} \beta} \tag{1.22}$$

Here we assume that for multiple profiles, all values of κ_m in the Airy profiles (1.16) are different so that the matrix $\left(\alpha k^2 + \gamma\right)$ is invertible. For one profile VBM, (1.22) reduces to

$$\Omega_{vbm}(k) = c_0 k \sqrt{1 - \frac{(k\beta)^2}{h_0(\alpha k^2 + \gamma)}} \tag{1.23}$$

The short wave behaviour is given by

$$\lim_{k\to\infty} \Omega_{vbm} = c_0 k \sqrt{1 - \frac{\beta^2}{\alpha h}}$$

This limit is real and nonzero as a consequence of the Cauchy-Schwartz inequality

$$\left[\int_{-h}^{0} f.1 dz\right]^2 \leq \int_{-h}^{0} f^2 dz. \int_{-h}^{0} 1^2 dz$$

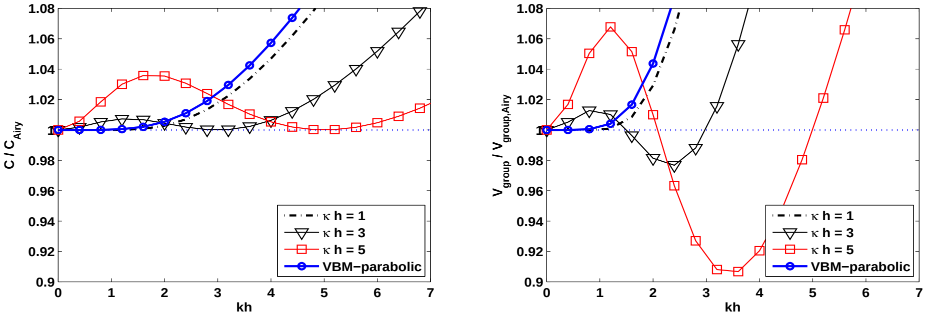

Figure 1.3: *In the left figure are shown the ratio with the exact phase velocity of Airy linear theory of the phase velocity of the VBM with parabolic profile (solid with circle), one Airy profile with* $\kappa h = 1$ *(dashed-dot),* $\kappa h = 3$ *(solid with downward-pointing triangle), and* $\kappa h = 5$ *(solid with square). The same in the right figure for the group velocities.*

for any choice of f, so $\beta^2 \leq \alpha h$ (Lakhturov et al. [2012]).

The limit for long waves of the VBM is $c_0 k$ for $h \to 0$, just as in the Airy dispersion relation.

Now, we will compare the dispersion relation of the VBM with one profile (1.23) with the exact dispersion relation (1.21). Using the Airy profile (1.16) as the vertical profile, for the specific value of κ_m the dispersion relation of VBM (1.22) has the exact value as in the Airy dispersion relation (1.21). As a consequence, it has the exact phase velocity for $k = \kappa_m$. In Figure 1.3 the ratio with the exact phase velocity of Airy linear theory of the phase velocities of the VBM with one Airy profile with $\kappa h = 1$, $\kappa h = 3$, $\kappa h = 5$ and with parabolic profile are shown, while in the right, the ratio of the group velocities. From these plots, it shows that the VBM with parabolic profile is only valid for long waves ($kh \leq 2.5$). For the VBM with one Airy profile, the velocity errors become larger for large value of κh and are only exact (in the phase velocity) at $kh = \kappa h$.

As can be observed in Figure 1.3, for $k \neq \kappa_m$, the VBM with one Airy profile has larger phase velocity compared to the exact one. This is actually true for any approximate VBM and is a direct consequence of the minimization property of the kinetic energy as in (1.9)

$$K = \min_{\Phi = \phi \text{ at } z=\eta} \frac{1}{2} \int \int_{-h}^{\eta} \left| \nabla_3 \Phi \right|^2 dz d\mathbf{x} \tag{1.24}$$

where an exact formulation can be obtained when one can find an optimum value of Φ with constraint $\Phi = \phi$ at $z = \eta$.

As stated in Lakhturov et al. [2012], for computational reason, the number of vertical profiles to be used in the VBM is desired to be as few as possible. Since we have the freedom to choose the value of κ_m for the Airy profile (1.16), this leads to the idea to optimize the dispersion relation of the VBM to be as close as possible to the exact dispersion relation. Our way to do so will be explained in the next section.

1.4.3 Optimization of the vertical profiles

As shown before, for waves with a narrow band spectrum, e.g. monochromatic waves, the choice for the wavenumber κ_m for the Airy profile (1.16) is clear to be the wavenumber that corresponds with the frequency of the waves to be simulated. But waves with a broad band spectrum, e.g. irregular waves, focusing wave groups, or freak-type of waves, the choice is not so clear. Intuitively, we expect κ_m to be (close to) the peak frequency of the waves to be simulated, since these are the most dominant waves in the spectra. In this section, we will show an optimization criterion to choose the optimum κ_m by using the kinetic energy minimization. It turns out that the optimal choice for κ_m will be far from the peak frequency of the broad band waves to be simulated. The optimization criterion to be described here, is based on the idea in Lakhturov, Adytia and van Groesen [2012] and in Lakhturov and van Groesen [2010] for flat bottom. In this section, the idea will be generalized for uneven bottom.

We will restrict to signalling problems. We simplify the problem to be linear and a horizontal bottom; hereafter we will show the generalization for an application with varying bottom. The kinetic energy expression in (1.24) can be rewritten in general form as

$$K(\phi) = \frac{1}{2g}\int |\Omega\phi|^2\, dx = \frac{1}{4\pi g}\int \left|\Omega(k)\,\widehat{\phi}(k)\right|^2 dk \tag{1.25}$$

Here Ω is the operator that is associated with the dispersion relation $\Omega(k)$ of a model, $\widehat{\phi}$ is the spatial Fourier transform of the surface potential ϕ. Now let $\eta_0(t) = \eta(x_0, t)$ be the influx signal given at position x_0. For uni-directional propagation, the governing equation is $\partial_t\hat{\eta} = i\Omega\hat{\eta}$, and there is a relation between the spatial and the temporal Fourier transform of the solution $\eta(x,t)$. Let $\Omega^{-1}(\omega) = k$ denote the inverse of $\Omega(k) = \omega$. Now we will relate the spatial Fourier transform of η to the temporal Fourier transform $\widetilde{\eta_0}(\omega)$ of the wave elevation $\eta_0(t)$. In uni-directional propagation it holds that

$$\eta(x,t) = \int \widehat{\eta_0}(k)\, e^{i(kx-\Omega(k)t)} dk = \int \widetilde{\eta_0}(\omega)\, e^{i\left(\Omega^{-1}(\omega)x-\omega t\right)} d\omega$$

Since $d\omega = V(k)\,dk$, where $V(k) = \partial\Omega(k)/\partial k$ is the group velocity, we conclude that

$$\widehat{\eta_0}(k) = V(k)\,\widetilde{\eta_0}(\omega) \tag{1.26}$$

where ω and k are related via the dispersion relation $\omega = \Omega(k)$.

For uni-directional waves, propagation of ϕ is given (in Fourier space) by $\partial_t\widehat{\phi} = -i\Omega(k)\,\widehat{\phi}$. Combining this fact with the second dynamic equation of the VBM (1.20) $\partial_t\phi = -g\eta$, we obtain a relation between the initial surface elevation η_0 and the initial surface potential ϕ_0

$$i\Omega(k)\,\widehat{\phi_0}(k) = g\widehat{\eta_0}(k) \tag{1.27}$$

By utilizing the relation (1.27) and the relation between spatial and temporal Fourier transforms of η_0 (1.26), we can rewrite expression (1.25) as

$$\begin{aligned} K &= \frac{g}{4\pi}\int \left|\widehat{\eta}_0\left(k\right)\right|^2 dk \\ &= \frac{g}{4\pi}\int \left|\widetilde{\eta}_0\left(\omega\right)\right|^2 V\left(\omega\right) d\omega \\ &= \frac{g}{2}\int S\left(\omega\right) V\left(\omega\right) d\omega \end{aligned} \tag{1.28}$$

where $S\left(\omega\right) = \widetilde{\eta}_0\left(\omega\right)\cdot\widetilde{\eta}_0^*\left(\omega\right)/2\pi$ is the power spectrum of the initial signal η_0. This shows that the kinetic energy expression can actually be rewritten in the form of the power spectrum of the given initial signal that is "weighted" with the group velocity. We will use this expression to optimize the dispersion relation of the VBM with the Airy profiles. As said, the kinetic energy for the exact dispersion will always be less than any approximation of VBM, which is the consequence of the minimization property (1.24). Utilizing this fact and the expression of the kinetic energy (1.28), we obtain as criterion for optimizing the choice of κ_m for the Airy profile(s) the minimization of the kinetic energy $K_{vbm}\left(\kappa_m\right)$ with respect to all possible κ_m

$$\min_{\kappa_m}\left[K_{vbm} - K_{ex}\right] = \min_{\kappa_m}\left\{\int \frac{g}{2}S\left(\omega\right)\left[V_{vbm}\left(\omega,\kappa_m\right) - V_{ex}\left(\omega\right)\right]d\omega\right\} \tag{1.29}$$

Here $V_{vbm}\left(\omega,\kappa_m\right)$ and V_{ex} are the group velocity of VBM (that depends on κ_m) and that of the exact Airy dispersion relation respectively. This optimized variant of the VBM will be called the *Optimized VBM* (OVBM).

Since the group velocity depends on the water depth, the generalization for varying bottom of (1.29) is given by

$$\min_{\kappa_m}\left[K_{vbm}\left(h\right) - K_{ex}\left(h\right)\right] = \min_{\kappa_m}\left\{\int \frac{g}{2}S\left(\omega\right)\left[V_{vbm}\left(\omega,\kappa_m,h\right) - V_{ex}\left(\omega,h\right)\right]d\omega\right\} \tag{1.30}$$

So, for varying bottom the minimization has to be performed for at each depth. Notice that the power spectrum $S\left(\omega\right)$ will change during wave propagation by nonlinear interactions and by bathymetry effects. But the value for κ_m in the Airy profile (1.16) has to be chosen a priori and (preferably) will not change during the wave propagation. For applications that we will deal with, the change in the power spectrum has been neglected.

In Figure 1.4, the quality of the dispersion relation, phase and group velocities of the OVBM with one, two and three profiles are shown. The value of κ_m are $\kappa = 3.16$ for 1-profile model, $\kappa_1 = 2.78$ and $\kappa_2 = 11.25$ for 2-profile model, and $\kappa_1 = 2.58$, $\kappa_2 = 11.24$, $\kappa_3 = 21.45$ for 3-profile model. These values are obtained for a test case of a freak-type of wave to be shown in the next section. In the upper left of Figure 1.4 the dispersion relation of the models are shown. In the upper right and lower left of Figure 1.4 the ratio of phase velocity of the models with the exact phase velocity are compared as functions of h/L_0 and kh respectively. In the lower right, the ratio of the group velocity of the models with the exact group velocity as functions of kh are shown.

Compared to the previous Boussinesq-type models (Peregrine [1967], Madsen and Sørensen [1992] and Nwogu [1993]) that were shown in Figure 1.2, the quality of dispersion

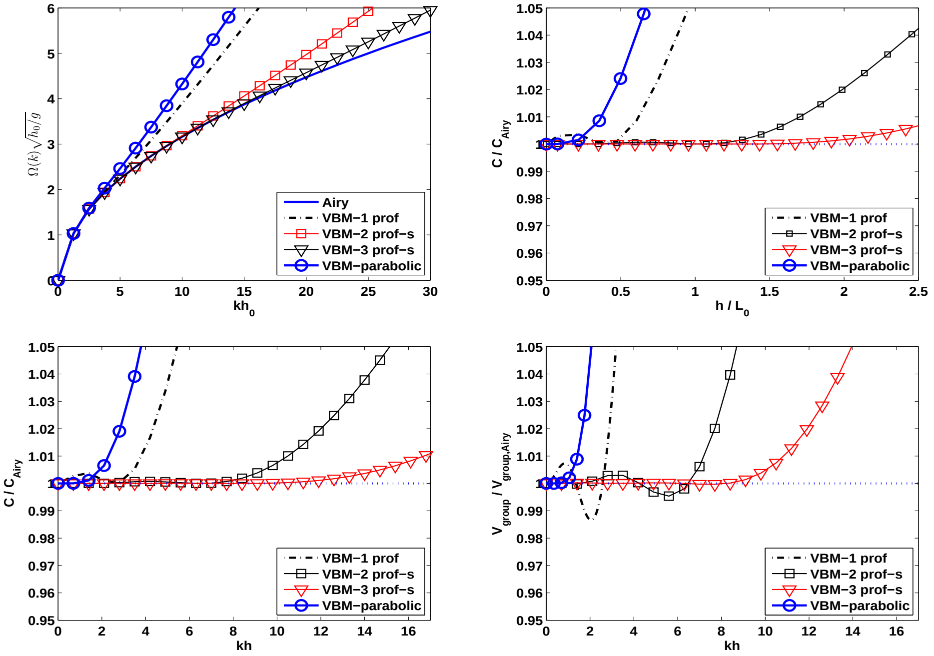

Figure 1.4: *Comparison of the VBM with parabolic profile (solid with circle), the Optimized VBM with one (dashed-dot), two (solid with square), and three profiles (solid with downward-pointing triangle) with the Airy linear theory in dispersion relation (upper left), the ratio of the phase velocity of the models with the phase velocity of Airy linear theory as functions of* h/L_0 *(upper right) and relative depth* kh *(lower left), and the ratio of the group velocity of the models with the group velocity of Airy linear theory (lower right).*

relation of the OVBM multiple profiles is much improved, i.e. the relative error (compared to the Airy theory) of the phase and group velocities are very small (up to 0.5% for two profiles and up to 0.02% for three profiles). Notice that the flexibility to choose the number of vertical profile functions and the possibility to optimize the vertical profiles with (1.30) means that the OVBM is *case-dependent*. In the OVBM, the model is optimized to give the best possible dispersion relation properties over the kh interval depending on the initial signal of the problem. This is different than other Boussinesq-type models that are mentioned previously in which the accuracy of these models is determined by the value of kh that can be achieved to obtain a certain the accuracy in dispersiveness for *all* simulations.

The performance of the 1D-OVBM for horizontal flat bottom will be illustrated in the next section. In Chapter 3, an application for varying bottom will be shown. In Chapters 4 and 5, the performance of the 2D-OVBM will be presented.

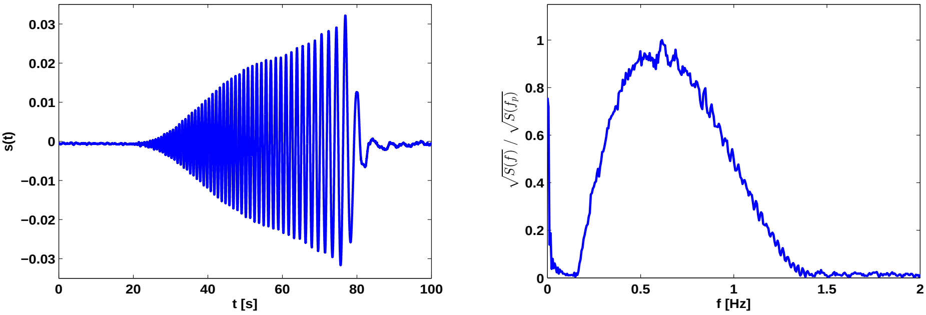

Figure 1.5: *The initial signal (left plot) and the amplitude spectrum (right plot) of the Focusing Wave Group experiment by MARIN.*

1.4.4 Broad band test-cases

In this section we show the performance of a Finite Element (FE) implementation of the Optimized Variational Boussinesq Model (OVBM). The numerical implementation will be described in detail in Chapter 2. Simulations of the FE-code of OVBM will be compared with two available experiments of waves with rather broad spectrum: a Focusing Wave Group (to be referred as FWG) and a freak-type of wave. Both experiments were conducted at MARIN (Maritime Research Institute Netherlands) hydrodynamic laboratory in Wageningen, The Netherlands, in a wave tank with 200 m length and 1 m of water depth.

The FWG is an experiment, with MARIN test number 101013, that was made for investigating wave focusing where short waves are generated before long waves. This experiment is designed in such a way that at a certain point, where the long (faster) waves catch up with the short (slow) waves, the waves collide and form a very high wave. The wave was generated by flap motion at $x = 0$, and measured at $x_0 = 10$ m and $x_1 = 50$ m. The measured elevation at x_0 is taken for numerical simulation as influx signal. Position $x_1 = 50$ m was designed to be the location where the waves are focused. The signal and its amplitude spectrum of this experiment at x_0 are shown in Figure 1.5. As seen, the spectrum of this wave is very broad. It turns out that using only one Airy profile function is not accurate enough to accommodate all short frequencies waves in the initial spectrum (see Lakhturov, Adytia, and van Groesen [2012]).

In Figure 1.6, we show the comparison of the signals at the focusing point of the OVBM with one (left plots) and two (right plots) profiles with value of κ_m that are obtained by using the kinetic energy minimization (1.29): $\kappa = 3.27$ (corresponds to 0.9 Hz) for the 1-profile model, and $\kappa_1 = 2.73$, $\kappa_2 = 5.25$ (corresponds to 0.43 Hz and 0.83 Hz) for the 2-profile model. In the upper part of Figure 1.6, the linear simulations of OVBM are shown, while in the lower part, the nonlinear simulations are shown. The contribution of the short (high frequency) waves are very important in this experiment. The result of OVBM with one profile is rather poor. Although the optimal value $\kappa = 3.27$ (corresponds to 0.8 Hz) is already far from the peak frequency (0.61 Hz), the errors in the speed and contribution of the shorter waves are still too large. As a consequence, the

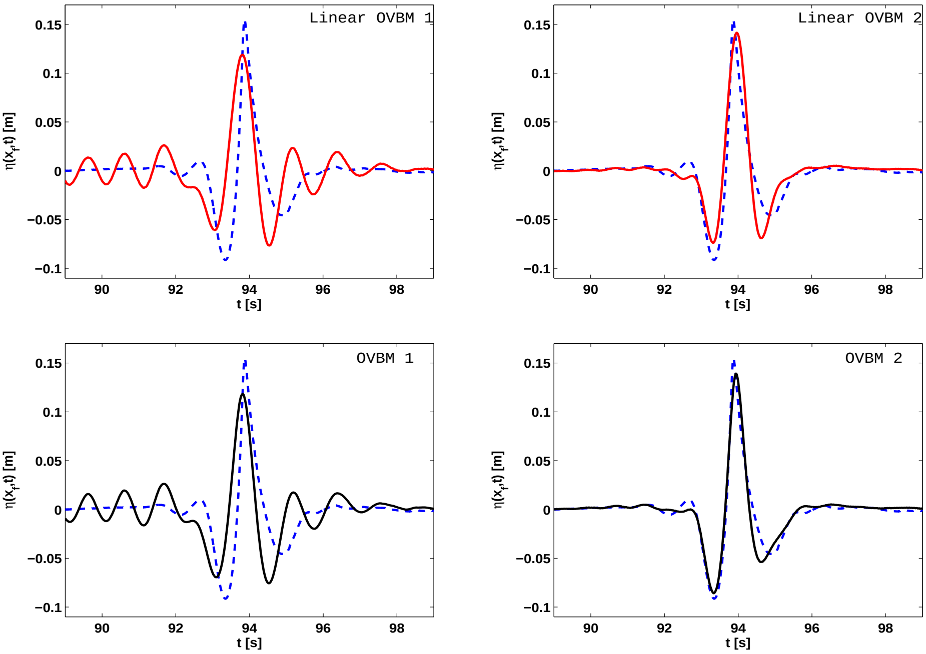

Figure 1.6: *Comparison of the linear (upper part) and nonlinear (lower part) simulations (solid lines) with the experiment of the Focusing Wave Group by MARIN (dash line). The left part is the result of OVBM with one profile, and the right part is with two profiles.*

maximal amplitude cannot be reached. While using two profiles, the error in phase and group velocities are much smaller than for the OVBM with one profile and the maximum (focusing) wave can be represented more accurately.

The other test case is a freak-wave. Freak waves (also called extremes waves, rogue waves, giant waves, monster waves) are unexpected large waves that suddenly appear in a relatively mild background wave field. It is called a freak wave if the ratio of the waveheight to the significant waveheight H_{sig} is more than 2 to 2.2 (Haver [2004]). The significant waveheight H_{sig} is the mean of the highest one-third of waves in the wave record, usually calculated as 4 times the standard deviation of the surface elevation η. One famous freak wave that has been recorded in nature by a measurement instrument is the Draupner wave or the New Year Wave; the wave was captured at the Draupner platform in the North sea off the coast of Norway on January 1, 1995. The maximum recorded waveheight is close to 26 m which is more than 2.2 times the significant waveheight (see Haver and Andersen [2000]).

The recorded wave was reconstructed at MARIN for a laboratory experiment, with MARIN test number 204001. The wave was generated at $x = 0$ m and measured at several positions $x = 10$ m, 20 m, 40 m, 49.5 m, 50 m and 54.5 m. The highest wave was observed at position $x = 50$ m. The measured signal and its amplitude spectrum at $x = 10$ m are shown in Figure 1.7. Notice that this wave has a very broad spectrum, even

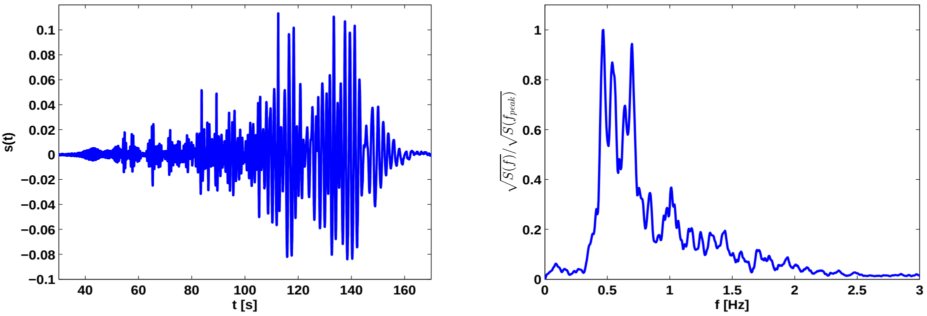

Figure 1.7: *The initial signal (left plot) and amplitude spectrum (right plot) of the New Year Wave experiment by MARIN.*

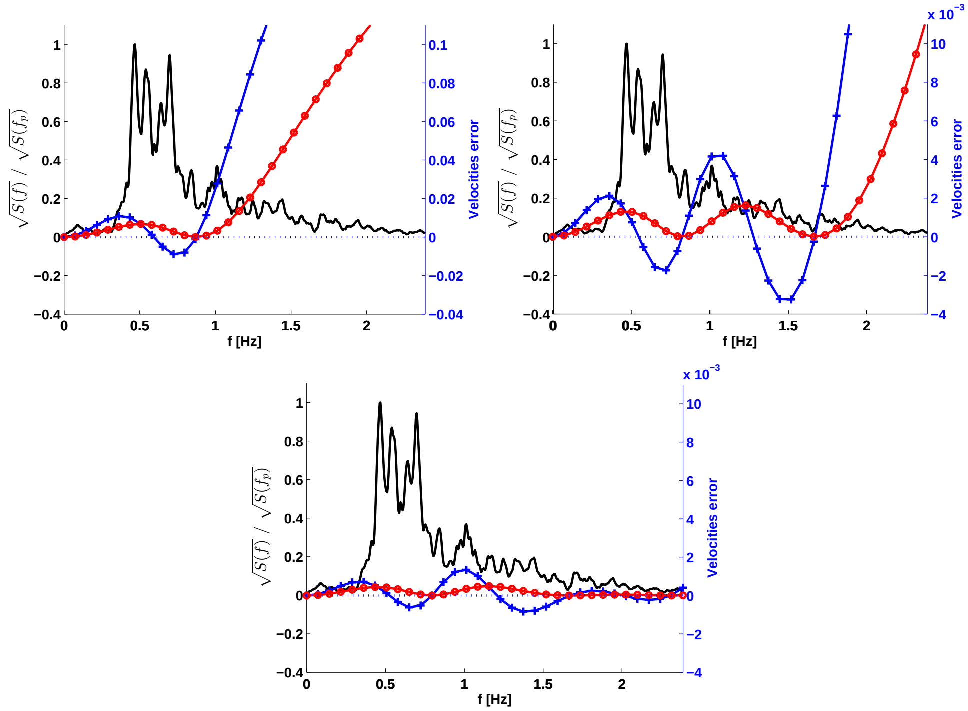

Figure 1.8: *The normalized amplitude spectrum (solid line, left hand axis) of the New Year Wave at* $x = 10$ *m is plotted together with the group velocity error (solid line with plus sign, right hand axis) and the phase velocity error (solid line with circle, right hand axis) as functions of frequency [Hz]. At the top left for the 1-profile model with* $\kappa = 3.16$ *(corresponds to* 0.88 *Hz), at the top right for the 2-profile model with* $\kappa_1 = 2.7$, $\kappa_2 = 11.24$ *(corresponds to* 0.82 *Hz and* 1.67 *Hz) and at the lower for the* 3*-profile model with* $\kappa_1 = 2.58$, $\kappa_2 = 11.24$, $\kappa_3 = 21.44$ *(corresponds to* 0.8 *Hz,* 1.67 *Hz and* 2.3 *Hz).*

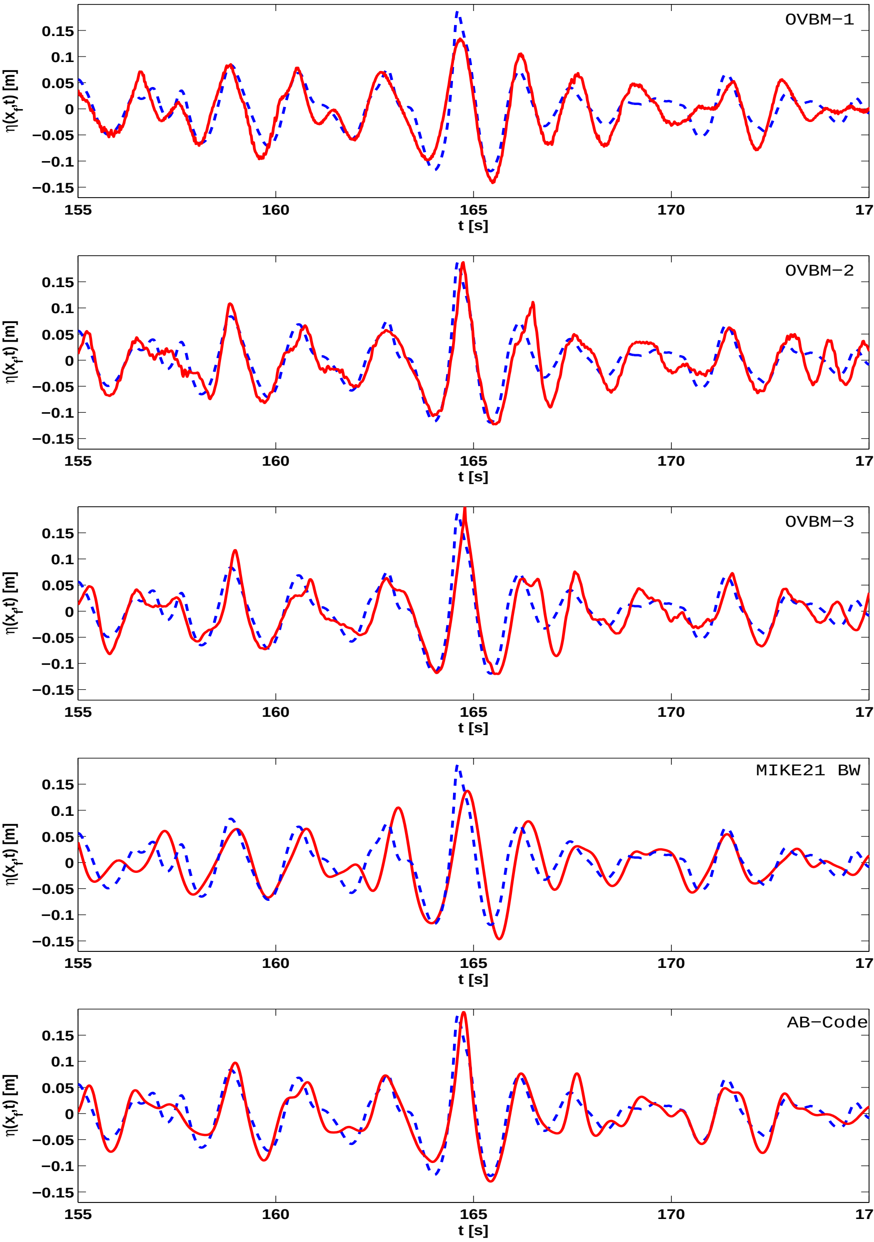

Figure 1.9: *The comparison of the experiment of The New Year Waves by MARIN (dashed line) with simulations (solid lines) of the OVBM with one (first row), two (second row) and three profiles (third row), the MIKE21 BW (fourth row), the AB-code (fifth row), at* $x = 50$ *m where the highest wave was observed.*

broader than the FWG that was shown in Figure 1.5. One can expect that the simulation with one profile will not be sufficient. This can already be anticipated from the plots in Figure 1.8 of the velocity errors of the OVBM with one (in the upper left plot), two (in the upper right plot) and three profiles (in the lower plot). The choices of κ_m in these plots are obtained by the optimization criterion in (1.29). The optimum values κ_m were given in Section 1.4.3. Using these optimal values, the quality of dispersion relation, phase and group velocities were shown in Figure 1.4. Using one profile, the velocity errors are quite large for the main frequencies of the waves, while with two and three profiles the errors are 10 and 20 times less, respectively. Therefore, to obtain good results for the New Year Wave simulation, two or three profiles are needed.

In Figure 1.9, we compare the measured signal at position $x = 50$ m with the simulations of the OVBM with one (first row), two (second row), three profiles (third row) and with two other codes: MIKE 21 BW (fourth row) and the AB-code (fifth row). MIKE 21 BW (MIKE, by DHI software) is a commercial package that uses the 'enhanced' Boussinesq model of Madsen and Sørensen [1992]. The quality of this model was shown in Figure 1.2. The AB-code is based on the AB-equation that was introduced in van Groesen and Andonowati [2007]. The AB-equation is a uni-directional model (originally) for flat bottom with exact dispersion in first and second order. This model has been extended for uneven bottom as the ABvar (van Groesen and Andonowati [2011] and van Groesen and van der Kroon [2012]). As expected, MIKE 21 BW and the OVBM with one profile cannot capture the maximum wave since they are poor in the dispersion relation. The OVBM with three profiles performs slightly better compared to the OVBM with two profiles. This is understandable since the phase and group velocities for the OVBM with three profiles is twice more accurate than the OVBM with two profiles, and 20 times more accurate than the OVBM with one profile model as can be seen in Figure 1.8.

1.5 Contents

In the previous sections, the development of Boussinesq-type of models has been described. This was followed by the derivation of the VBM in the framework of a variational principle, and the description of an optimization criterion for the choice of vertical profiles of the VBM. The performance of a Finite Element implementation of the OVBM was shown for simulating broad band waves above a constant bottom. In this short section we present the contents of the rest of this thesis.

In Chapter 2, we will give details of the numerical implementation of the model, together with technicalities regarding the boundary conditions, e.g. the fully reflective (hardwall) boundary condition, damping or absorbing boundary condition, and also an internal influxing method for both the 1D and 2D OVBM. To broaden the applicability of the model, we use the Finite Element Method (FEM) for numerical implementation rather than the pseudo-spectral method that was used in the previous variant of the VBM (Klopman et al. [2005, 2007, 2010]). Furthermore, especially for the 2D applications where the geometry is usually very complex, e.g. harbour geometry or coastline for a tsunami simulation, the use of an unstructured grid in the FEM is very helpful.

Chapter 3 is a published paper of the 1D Optimized Variational Boussinesq Model for varying bottom (Adytia and van Groesen [2012]). The paper describes the simulations of regular bichromatic waves and irregular waves that propagate above a sloping bottom where experimental data are available from MARIN hydrodynamic laboratory.

Chapter 4 is an extension of a published paper (Adytia and van Groesen [2011]), where the performance of the 2D FE implementation of the VBM is tested against the shoaling experiment of Berkhoff et al. [1982]. This experiment is well known for testing the ability of a code to represent refraction, diffraction and shoaling of nonlinear periodic waves.

In Chapter 5, the applicability of the 2D OVBM for simulating regular and irregular waves in the harbour of Jakarta (Pelabuhan Tanjung Priok) in Indonesia will be shown.

Finally, in Chapter 6, conclusions and outlook for future work will be summarized.

Chapter 2

Numerical Implementation

Summary

This chapter describes in Section 2.1 a numerical implementation for the Optimized VBM that was derived in Chapter 1. Consistent with the derivation of the model via the variational formulation, the Finite Element Method (FEM) is used for the spatial discretization. Since the highest spatial derivatives in the Lagrangian of the model are of the first order (second order in the equations), standard linear spline basis functions will be used. The resulting matrix system is then solved by using a Runge-Kutta time integrator for the dynamic system and an iterative method for solving the elliptic system.

In the implementation of the model, several types of boundary conditions will be used. The fully reflective (hard wall) boundary conditions will be shown to be the 'natural' boundary condition in the variational sense of the model. To absorb outgoing waves, a sponge-layer type of boundary will be implemented in the model. Also, since we mainly deal with signalling problems, an internal influx technique will be described in Section 2.2. Several cases for testing the combinations of these boundary conditions will be shown at the end of this chapter.

2.1 Variational formulation and Finite Element implementation

As described in Chapter 1, the VBM is derived via the variational formulation. For numerical implementation of the model, several types of boundary condition need to be imposed. To that end, we first derive the natural boundary condition of the model. More precisely, recall the Lagrangian for the VBM

$$\mathcal{L}_{vbm}\left(\eta, \phi, \psi_m\right) = \int_t \left[\int_{\mathbf{x}} \phi \partial_t \eta - \mathcal{H}_{vbm}\left(\phi, \eta, \psi_m\right) \right] d\mathbf{x} dt \qquad (2.1)$$

with $\mathcal{H}_{vbm} = P + K_{vbm}$, with K_{vbm} defined in (1.19). As stated in the previous chapter, vanishing of the first variations of (2.1) with respect to variations $\delta\phi$ of ϕ and $\delta\eta$ of η lead to the dynamic equations, while vanishing of the first variation with respect to variations $\delta\Psi$ of $\Psi = [\psi_1, \psi_2, ..\psi_N]$ leads to a system of elliptic equations. These are given by

$$\int_t \left\{ \int_{\mathbf{x}} \{\partial_t \eta \left(\delta\phi\right) - \left[\left(h+\eta\right)\nabla\phi.\nabla\left(\delta\phi\right) + \nabla\left(\delta\phi\right)\beta\cdot\nabla\Psi\right]\} \, d\mathbf{x} \right\} dt = 0 \tag{2.2}$$

$$\int_t \left\{ \int_{\mathbf{x}} \left\{ \phi\partial_t\left(\delta\eta\right) - \left[g\eta + \frac{1}{2}\left|\nabla\phi\right|^2\right]\left(\delta\eta\right) \right\} d\mathbf{x} \right\} dt = 0 \tag{2.3}$$

$$\int_t \left\{ \int_{\mathbf{x}} \{\beta\nabla\phi\cdot\nabla\left(\delta\Psi\right) + \alpha\nabla\Psi\cdot\nabla\left(\delta\Psi\right) + \gamma\Psi\cdot\left(\delta\Psi\right)\} \, d\mathbf{x} \right\} dt = 0 \tag{2.4}$$

The first variations above are called *the weak form* of the VBM. Now, by applying integration by parts in the second and third terms of (2.2), in the first term of (2.3), and in the first and second terms of (2.4), we obtain

$$\int_t \left\{ \int_{\mathbf{x}} \{\partial_t\eta + \nabla.\left[\left(h+\eta\right)\nabla\phi + \beta\cdot\nabla\Psi\right]\}\left(\delta\phi\right) d\mathbf{x} \; + B_1\left(\phi,\Psi\right) \right\} dt = 0 \tag{2.5}$$

$$\int_t \left\{ \int_{\mathbf{x}} \left[-\partial_t\phi - \left(g\eta + \frac{1}{2}\left|\nabla\phi\right|^2\right)\right]\left(\delta\eta\right) \; d\mathbf{x} + B_2\left(\phi\right) \right\} dt = 0 \tag{2.6}$$

$$\int_t \left\{ \int_{\mathbf{x}} \{-\nabla.\left[\beta\nabla\phi + \alpha\nabla\Psi\right] + \gamma\Psi\}\cdot\left(\delta\Psi\right) d\mathbf{x} + B_3\left(\phi,\Psi\right) \right\} dt = 0 \tag{2.7}$$

where $B_1\left(\phi,\Psi\right)$, $B_2\left(\phi\right)$ and $B_3\left(\phi,\Psi\right)$ are boundary terms

$$\begin{aligned} B_1\left(\phi,\Psi\right) &= -\int_{\partial X}\left(\delta\phi\right)\left[\left(h+\eta\right)\nabla\phi + \beta\cdot\nabla\Psi\right].\underline{n}d\partial X \\ B_2\left(\phi\right) &= \int_{\partial T}\phi\left(\delta\eta\right)\; d\partial T \\ B_3\left(\phi,\Psi\right) &= \int_{\partial X}\left(\delta\Psi\right)\cdot\left[\beta\nabla\phi + \alpha\nabla\Psi\right].\underline{n}\; d\partial X \end{aligned}$$

Here, ∂X and ∂T denote the boundary in space and in time respectively. The vector $\underline{n}= \left(n_x, n_y\right)$ is the outward normal vector. B_2 is a dynamically uninteresting term and will be neglected. Since the weak forms should vanish for all variations of $\delta\phi$, $\delta\eta$ and $\delta\Psi$, we obtain the system of PDE as in (1.20) with natural boundary conditions

$$\begin{aligned} \left[\left(h+\eta\right)\nabla\phi + \beta\cdot\nabla\Psi\right].\underline{n} &= 0 \\ \left[\beta\nabla\phi + \alpha\nabla\Psi\right].\underline{n} &= 0 \end{aligned}$$

For illustration, we write the natural boundary conditions above for the VBM with 1-profile as

$$\begin{bmatrix} \left(h+\eta\right) & \beta \\ \beta & \alpha \end{bmatrix} \begin{bmatrix} \nabla\phi \\ \nabla\psi \end{bmatrix} = 0 \tag{2.8}$$

The natural boundary conditions above can only be satisfied if $\left(h+\eta\right)\alpha - \beta^2 = 0$ or if $\nabla\phi$ and $\nabla\psi$ vanish. But the first condition is not satisfied for both the parabolic (1.15) and

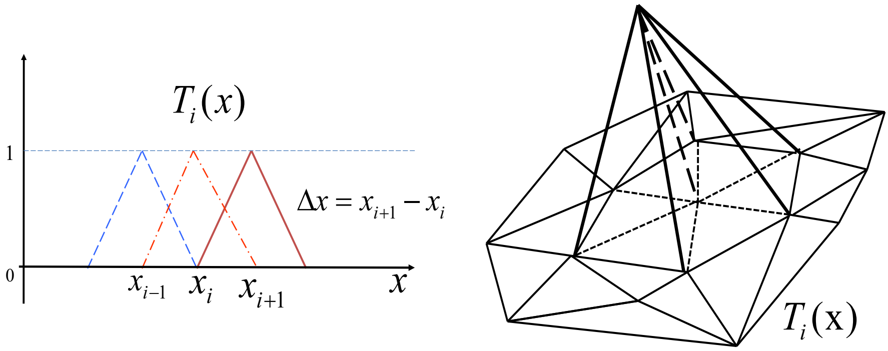

Figure 2.1: *Illustration of the linear spline basis functions in 1D (left) and 2D (right).*

the Airy profile (1.16), which implies that $\nabla\phi$ and $\nabla\psi$ should vanish. This condition is actually the fully reflective (hard wall) boundary condition which requires the horizontal velocity $U = \nabla\Phi = \nabla\phi + F\nabla\psi$ to vanish at the boundary. This shows that vanishing of the first variation of (2.1) with respect to ϕ, η and ψ_m is equivalent with the PDE of the VBM (1.20) with the fully reflective boundary condition (2.8).

Now we show the procedure for the numerical implementation of the model. Directly from the Lagrangian (2.1), it is possible to obtain a consistent numerical discretizations for the solutions ϕ, η and ψ_m. The solutions will be approximated by superpositions of chosen basis functions $\{T_i(\mathbf{x})\}_{i=1}^{n}$ as

$$\begin{aligned}
&\eta(\mathbf{x},t) \approx \Sigma_{i=1}^{n}\eta_i(t)\,T_i(\mathbf{x}) = \overline{\eta}(t)\cdot T(\mathbf{x})\\
&\phi(\mathbf{x},t) \approx \Sigma_{i=1}^{n}\phi_i(t)\,T_i(\mathbf{x}) = \overline{\phi}(t)\cdot T(\mathbf{x})\\
&\Psi(\mathbf{x},t) = \left[\psi_1(\mathbf{x},t),\psi_2(\mathbf{x},t),...,\psi_N(\mathbf{x},t)\right]\\
&\qquad\qquad\approx \left[\Sigma_{i=1}^{n}\psi_{1,i}(t)\,T_i(\mathbf{x}),\Sigma_{i=1}^{n}\psi_{2,i}(t)\,T_i(\mathbf{x}),...,\Sigma_{i=1}^{n}\psi_{N,i}(t)\,T_i(\mathbf{x})\right] = \underline{\Psi}(\mathbf{x},t)
\end{aligned} \tag{2.9}$$

where $\overline{\eta}$, $\overline{\phi}$, $\underline{\Psi}$ and $T(\mathbf{x})$ are vector functions. Here, we use the simplest basis functions in the FEM which are the linear spline basis functions as illustrated in Figure 2.1 for 1D (left plot) and 2D (right plot). It is possible to use these basis functions since the highest spatial derivatives in the Lagrangian (2.1) are of first order. For 1D FEM, the expression of these basis functions $\{T_i(x)\}_{i=1}^{n}$ is given by

$$T_i(x) = \begin{cases} \frac{x-x_{i-1}}{x_i-x_{i-1}}, & \text{if, } x \in [x_{i-1}, x_i]\\ \frac{x_{i+1}-x}{x_{i+1}-x_i}, & \text{if, } x \in [x_i, x_{i+1}]\\ 0, & \text{else}\end{cases} \tag{2.10}$$

For an equidistant grid with spatial grid size Δx, the formula above can be rewritten as

$$T_i(x) = \max\left\{1 - \frac{|x-x_k|}{\Delta x}, 0\right\} \tag{2.11}$$

The formula for 2D basis functions will be described in Appendix 2A.

Now we substitute the approximations in (2.9) directly into the Lagrangian (2.1) and obtain

$$\int_{\mathbf{x}} \phi \partial_t \eta d\mathbf{x} \approx \Sigma_{i,j} \phi_i \dot{\eta}_j M_{i,j} {=} M\bar{\phi} \cdot \partial_t \bar{\eta}$$

for the first term in (2.1). Here M is the so-called *mass-matrix*, with elements

$$M_{i,j} = \int_{\mathbf{x}} T_i \left(\mathbf{x}\right) T_j(\mathbf{x}) d\mathbf{x}.$$

$\dot{\eta}_j$ denotes the derivative of η_i with respect to time t. The second term in (2.1) results in

$$\begin{aligned} \mathcal{H}_{vbm}\left(\phi, \eta, \Psi\right) &= \frac{1}{2} \int_{\mathbf{x}} [g\eta^2 + \left(h + \eta\right) \left|\nabla \phi\right|^2 + 2\nabla\phi\beta \cdot \nabla\Psi + \nabla\Psi \cdot \alpha\nabla\Psi + \Psi \cdot \gamma\Psi] d\mathbf{x} \\ &\approx \frac{1}{2} gM\bar{\eta} \cdot \bar{\eta} + \frac{1}{2}\mathbf{D}\bar{\phi} \cdot \bar{\phi} + H_3\left(\bar{\eta}, \bar{\phi}\right) + \mathbf{B} \cdot \underline{\Psi} + \frac{1}{2}\mathbf{A}\underline{\Psi} \cdot \underline{\Psi} + \frac{1}{2}\mathbf{G}\underline{\Psi} \cdot \underline{\Psi} \\ &= \bar{\mathcal{H}}_{vbm}(\bar{\phi}, \bar{\eta}, \underline{\Psi}) \end{aligned}$$

where **D** and **A** are so-called *stiffness-matrices* with elements

$$\begin{aligned} D_{i,j} &= \int_{\mathbf{x}} h\left(\mathbf{x}\right) \nabla T\left(\mathbf{x}\right) \cdot \nabla T\left(\mathbf{x}\right) d\mathbf{x} \\ A_{i,j} &= \int_{\mathbf{x}} \alpha\left(\mathbf{x}\right) \nabla T\left(\mathbf{x}\right) \cdot \nabla T\left(\mathbf{x}\right) d\mathbf{x} \end{aligned}$$

respectively, **G** is the matrix with elements

$$\mathbf{G}_{i,j} = \int_{\mathbf{x}} \gamma\left(\mathbf{x}\right) T_i\left(\mathbf{x}\right) T_j(\mathbf{x}) d\mathbf{x}.$$

B is the column vector

$$\mathbf{B} = \left[B\left(\beta_1\right)\bar{\phi}, B\left(\beta_2\right)\bar{\phi}, \cdots B\left(\beta_N\right)\bar{\phi}\right], \text{ with } B\left(\beta_i\right) = \int_{\mathbf{x}} \beta_i \nabla T\left(\mathbf{x}\right) \cdot \nabla T\left(\mathbf{x}\right) d\mathbf{x}$$

and $\bar{H}_3\left(\bar{\eta}, \bar{\phi}\right)$ is the nonlinear cubic term

$$\bar{H}_3\left(\bar{\eta}, \bar{\phi}\right) = \frac{1}{2}\Sigma_{i,j,k}\eta_i\phi_j\phi k C_{ijk}, \text{ with } C_{ijk} = \int_{\mathbf{x}} T\left(\mathbf{x}\right) \nabla T\left(\mathbf{x}\right) \cdot \nabla T\left(\mathbf{x}\right) d\mathbf{x}$$

Now the Lagrangian of the VBM (2.1) becomes a Lagrangian with vector state variables $\left(\bar{\phi}, \bar{\eta}, \underline{\Psi}\right)$

$$\bar{\mathcal{L}}\left(\bar{\phi}, \bar{\eta}, \underline{\Psi}\right) = \int_t \left[M\bar{\phi} \cdot \partial_t\bar{\eta} - \bar{\mathcal{H}}_{vbm}\left(\bar{\phi}, \bar{\eta}, \underline{\Psi}\right)\right] dt \tag{2.12}$$

Vanishing of the first derivatives of (2.12) with respect to $\bar{\phi}$ and $\bar{\eta}$ results in the Hamiltonian equations as the matrix system

$$M\partial_t\bar{\eta} = \partial_{\bar{\phi}}\bar{H}_{vbm} = \mathbf{D}\bar{\phi} + \bar{b}\left(\bar{\eta}, \bar{\phi}\right) + B\left(\beta\right) \cdot \underline{\Psi} \tag{2.13}$$

$$M\partial_t\bar{\phi} = -\partial_{\bar{\eta}}\bar{H}_{vbm} = -gM\bar{\phi} - \bar{v}\left(\bar{\phi}\right) \tag{2.14}$$

where $\bar{b}\left(\bar{\eta},\bar{\phi}\right)$ and $\bar{v}\left(\bar{\phi}\right)$ are column vector with elements

$$b_j\left(\bar{\phi},\bar{\eta}\right) = \partial_{\phi_j}\bar{H}_{vbm} = \Sigma_{i,k}\eta_i\phi_k C_{ijk}$$
$$v_j\left(\bar{\phi}\right) = \partial_{\eta_j}\bar{H}_{vbm} = \frac{1}{2}\Sigma_{i,k}\phi_i\phi_k C_{jik}$$

Also, vanishing of the first derivative of (2.12) with respect to $\underline{\Psi}$ results in an additional matrix system of linear elliptic equations from $\partial_{\underline{\Psi}}\bar{H}_{vbm} = 0$

$$\left[\mathbf{A}+\mathbf{G}\right]\underline{\Psi} = -\mathbf{B} \tag{2.15}$$

The matrix system (2.13),(2.14) and (2.15) can also be obtained by the so-called *Ritz-Galerkin* method. In this method, we first obtain the weak formulation of the VBM equations (1.20) by multiplying with arbitrary test functions and then integrate over the domain of computation. The resulting weak formulations are (2.2), (2.3), and (2.4). By integrating by parts and substituting the approximate solutions (2.9), we obtain equivalent results as (2.13), (2.14) and (2.15) with fully reflective boundary condition as the natural boundary condition.

Recapitulating so far, we have discretized the VBM equations in space using basis functions $\{T_i\left(\mathbf{x}\right)\}_{i=1}^{N}$. This discretization results in the ODE-system (2.13), (2.14) and (2.15) which can be solved according to the following algorithm:

1. For an initial value problem, for given initial conditions $\bar{\eta}_0 = \bar{\eta}\left(t=0\right)$ and $\bar{\phi}_0 = \bar{\phi}\left(t=0\right)$, we calculate/update the coefficients α, β and γ given by (1.18), then calculate $\underline{\Psi}_1$ by solving (2.15).

2. By using the initial conditions η_0, ϕ_0 and the resulting $\underline{\Psi}_1$ (from the elliptic system), we solve the dynamic matrix system (2.13) and (2.14) by using a time integrator. Here, we choose Runge-Kutta formulas of order 4 and 5 (or ODE45 in MATLAB).

3. These steps can be repeated until the desired end-time.

Note that for multiple vertical profiles and a large size of the spatial discretization, the elliptic matrix system (2.15) can become very large. But since we use local basis functions as (2.11), the resulting matrix $(\mathbf{A}+\mathbf{G})$ in (2.15) is very sparse. Also, since the VBM has positive Hamiltonian, this matrix is symmetric and positive. Therefore, an iterative method such as preconditioned conjugate gradient method can and will be used. In general, the solution for the elliptic system will only take 2 to 10 iterations, since we have a good initial guess of $\underline{\Psi}$ from the previous time step. Overall, for the applications in this thesis, the time to solve the elliptic system takes 20% to 40% of the total computational time.

For the 1D numerical implementation of the VBM we use an equidistant grid. For the 2D implementation, an unstructured triangular grid will be used. An unstructured triangular grid system gives more flexibility than a regular rectangular grid, e.g. local refinement can be applied in shallower areas where the waves have shorter wavelength and complex geometries of the domain, e.g. the boundary of a harbour or a complex coastline, can be well represented by using an unstructured triangular grid.

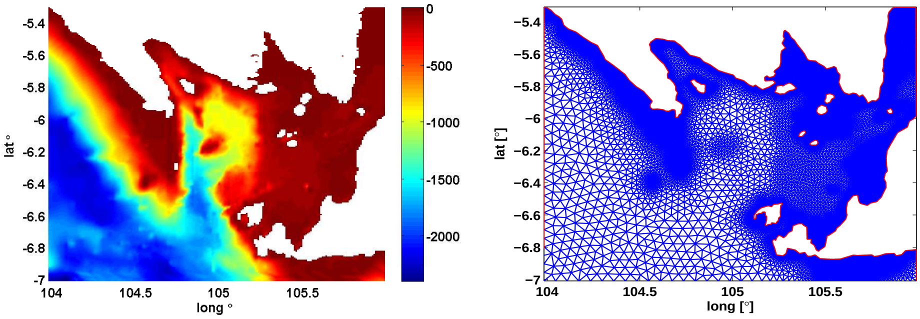

Figure 2.2: *An illustration for 2D of an unstructured triangular grid (right) where the grid size depends on the bottom topography (left).*

For the coastal applications in this thesis, we use a 2D mesh generator that is based on the algorithm of *DistMesh - A Simple Mesh Generator in MATLAB* that was introduced in Persson and Strang [2008]. In this algorithm, the grid size can be made to depend on a prescribed function. Since the wavelength of a water wave depends on the water depth, i.e. in deep water a wave has longer wavelength than in shallower water, the grid size can be made to depend on this physical property. The procedure to do so can be described as follows. In water waves, the period of a wave is given by $T = \lambda/c_p$, where λ is the wavelength and c_p is the phase velocity. This period will not change during the wave propagation. Suppose we only consider the period of the long waves $T_0 = \lambda_0/c_0$, where λ_0 and $c_0 = \sqrt{gh}$ are the wavelength and phase speed of the long waves respectively. By assuming one wave can be well represented by 20 points, we can estimate the grid size for a given wave period T_0 and water depth $h(\mathbf{x})$ as

$$\textit{grid size} \approx \frac{\lambda_0(\mathbf{x})}{20} = \frac{T_0\sqrt{gh(\mathbf{x})}}{20}$$

Figure 2.2 gives an illustration of an unstructured triangular grid, for wave period $T =$ 120 s (used in tsunami-simulation), that depend on the water depth. In the left plot of Figure 2.2 the bathymetry (bottom topography) is shown, while in the right plot the corresponding grid is shown.

For coastal applications, two types of boundary condition, e.g. fully reflective and absorbing (sponge layer) boundary conditions, need to be imposed in the numerical implementation of the model. Also, an internal wave generation is needed for dealing with signalling problems. The fully reflective boundary condition has been shown as the natural boundary condition of the VBM (2.8). Now we will describe the absorbing (sponge layer) boundary, and then in the next section we describe the derivation of an internal wave generation method.

Absorbing boundaries should dissipate the energy of the incoming wave so that no reflected waves will be generated at the boundary. To apply this type of boundary, we force the surface elevation η and the surface potential ϕ to decay in a damping-zone (sponge layer). The damping-zone is defined by a smoothened characteristic function $\chi(\mathbf{x})$, which has value one in the damping-zone and vanishes in the domain of interest.

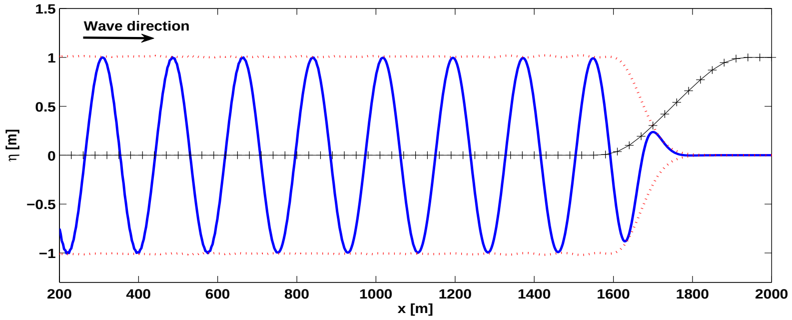

Figure 2.3: *An illustration of the characteristic function $\chi(x)$ (solid line with marker +) for damping-zone and its effect when it is applied to a harmonic wave (solid line).*

In the damping-zone, the exponential decay of the solutions η and ϕ is of the order of e^{-aT_d}, where a is a damping coefficient and T_d is the travel time of the wave in the damping-zone. As an illustration, to obtain an exponential decay of the longest waves up to 10^{-3} ($\approx e^{-7}$), the width of the damping-zone should be at least $L_d = 7c_0/a$, where $c_0 = \sqrt{gh}$. By implementing this boundary, the dynamic matrix system in (2.13), (2.14) becomes

$$M\partial_t\bar{\eta} = \mathbf{D}\bar{\phi} + \bar{b}\left(\bar{\eta}, \bar{\phi}\right) + B\left(\beta\right) \cdot \underline{\Psi} - aM(\bar{\chi} \cdot \bar{\eta}) \tag{2.16}$$

$$M\partial_t\bar{\phi} = -gM\bar{\phi} - \bar{v}\left(\bar{\phi}\right) - aM(\bar{\chi} \cdot \bar{\phi}) \tag{2.17}$$

where $\bar{\chi}$ is the vector of the discretized function $\chi(x)$. In Figure 2.3, a monochromatic wave with period $T = 12$ s and wavelength 177 m propagating above a flat bottom $h = 30$ m is damped in the damping-zone at $x \in [1600m, 2000m]$.

2.2 Internal wave generation

To simulate waves from offshore to nearshore, the waves have to be generated offshore. Although it is possible to generate waves at the boundary of a computation domain, waves that are reflected within the domain should be able to pass through this boundary. An alternative way is to use a combination of internal wave generation and an absorbing boundary; this has been used in the applications described in this thesis, and will now be detailed.

Internal wave generation, to be referred as embedded influxing, has been a specific problem in water wave modelling. Especially for Boussinesq-type models, embedded influxing techniques have been developed since 1983 when Larsen and Dancy applied the technique for the classical Boussinesq model of Peregrine [1967]. In general, embedded influxing is achieved by adding a source function to the continuity equation of the Boussinesq model. The precise expression of the source function is obtained by comparing the solution of the linear, forced Boussinesq equations, with the desired wave signals to be influxed. As a consequence, the source function will depend on the model to be investigated. Wei et al. [1999] used a Gaussian shaped source function for the nonlinear shallow water equations, the classical Boussinesq equations of Peregrine [1967] and the extended Boussinesq equations of Nwogu [1993]. Kim et al. [2007] showed that for these internal wave generation techniques the group velocity plays a central role.

In Wei et al. [1999] and Kim et al. [2007], solutions of the linearized model (including the source function) are obtained by using the Green function method. The method to be described here is based on Liam et al. where the solutions of the linearized model are obtained in a general way for dispersive wave models. The source function will be derived for linear dispersive wave equations, but for the examples in this thesis, this linear generation approach is also accurate enough for nonlinear wave propagation.

We use the following notational conventions. For 1D we use x as spatial coordinate and k for the wavenumber. In 2D we use $\mathbf{x} = (x, y)$ as coordinates, $\mathbf{k} = (k_x, k_y)$ as wave vector, and write $x = |\mathbf{x}|$ and $k = |\mathbf{k}|$ for the length of these vectors respectively. The dispersion relation of a dispersive wave model describes the relation between the wavenumber k (in 1D) or the wave vector $\mathbf{k}$ (in 2D) and the angular frequency ω. The dispersion relations of the Airy linear theory and the VBM are given in (1.21) and (1.22) respectively. We will write the dispersion relation of a dispersive wave model in 1D as well as in 2D as $\omega^2 = D$ with $D = \Omega^2$. The corresponding dispersive evolution can be written in 1D and 2D as a second order time equation for the surface elevation η as $\partial_t^2 \eta = -\mathcal{D}\eta$ and, equivalently, as the (Hamiltonian) system of two first order equations for η and ϕ as

$$\begin{cases} \partial_t \eta & = \frac{\mathcal{D}}{g}\phi \\ \partial_t \phi & = -g\eta \end{cases} \tag{2.18}$$

Here, $\mathcal{D}$ is the pseudo-differential operator that is related to D through spatial Fourier transformation. After Fourier transform, the system (2.18) reads

$$\begin{cases} \partial_t \hat{\eta} & = \frac{D(k)}{g}\hat{\phi} \\ \partial_t \hat{\phi} & = -g\hat{\eta} \end{cases} \tag{2.19}$$

The general solution of the initial value problem of this Hamiltonian system is given by

$$\begin{pmatrix} \hat{\eta} \\ \hat{\phi} \end{pmatrix} = \begin{pmatrix} \cos(\Omega t) & \frac{\Omega}{g}\sin(\Omega t) \\ -\frac{g}{\Omega}\sin(\Omega t) & \cos(\Omega t) \end{pmatrix} \begin{pmatrix} \hat{\eta}_0 \\ \hat{\phi}_0 \end{pmatrix} \tag{2.20}$$

Since the model is linear, it is possible to apply the superposition principle for homogeneous solutions (2.20). To construct an embedded influxing, we extend these equations by adding a source function of time and position in the dynamic equation. From the superposition principle, a particular solution of the inhomogeneous equation can be added to the general solution of the homogeneous equation. In other words, waves that are generated by embedded influxing will not affect the wave field of the homogeneous system.

The problem in the embedded influxing approach is to determine the source function such that at specified points in the domain (the influx location), the specified excitation is applied. More precisely, for an influx area denoted by B, let at each point $b \in B$ an excitation signal $s(t, b)$ be given. Then a source has to be found such that the wave field that is generated has the prescribed surface elevation: $\eta_p(b, t) = s(t, b)$.

Since superposition of source functions is possible by linearity of the model, it is sufficient to consider a single excitation point, e.g. $\mathbf{x} = \mathbf{0}$. Then, for forcing in the continuity equation, we will look for a source function $F_0(\mathbf{x},t)$ such that the solution $\zeta(\mathbf{x},t)$ of

$$\begin{aligned}\partial_t \zeta &= \frac{D}{g}\psi + F_0(\mathbf{x},t) \\ \partial_t \psi &= -g\zeta\end{aligned}$$

satisfies $\zeta(\mathbf{0},t) = s_0(t)$, where s_0 is the desired elevation at $\mathbf{x} = \mathbf{0}$. Here, ζ is the fundamental solution for a single point excitation at position $\mathbf{x} = \mathbf{0}$. By knowing F_0, the source for multiple excitation problem will then be given by a superposition

$$F(\mathbf{x},t) = \int_B F_0(\mathbf{x} - b, t)\, db \tag{2.21}$$

with corresponding wave field $\eta_{generated}(\mathbf{x},t) = \int \zeta(\mathbf{x} - b, t)\, db$.

For the applications in this thesis, we consider source functions $F(\mathbf{x},t)$ of the form

$$F(\mathbf{x},t) = \gamma(\mathbf{x})\, f(t) \tag{2.22}$$

with $\gamma(\mathbf{x})$ a spatially dependent function and $f(t)$ a time dependent function. Point source generation is obtained when $\gamma(\mathbf{x}) = \delta_{Dir}(\mathbf{x})$, is the Dirac delta function; other cases will have a smooth function $g(\mathbf{x})$ for a spatially extended source function with $\gamma(\mathbf{x}) = g(\mathbf{x})$.

The system for the forced inhomogeneous equation can be written down in 1D and 2D as

$$\begin{aligned}\partial_t \zeta &= \frac{D}{g}\psi + F(\mathbf{x},t) \\ \partial_t \psi &= -g\zeta\end{aligned}$$

After spatial Fourier transformation, the system can be written as

$$\begin{aligned}\partial_t \hat{\zeta} &= \frac{D}{g}\hat{\psi} + \hat{F}(\mathbf{k},t) \\ \partial_t \hat{\psi} &= -g\hat{\zeta}\end{aligned} \tag{2.23}$$

The solution is obtained from the variation of constants formula using the homogeneous solutions (2.20). For ζ there results in Fourier space :

$$\hat{\zeta}(\mathbf{k},t) = \int_0^t \cos\left(\Omega(k)(t-\tau)\right) \hat{F}(\mathbf{k},t)\, d\tau \tag{2.24}$$

Inverse spatial Fourier transformation leads to

$$\zeta(\mathbf{x},t) = \int_0^t \int_{-\infty}^{\infty} \cos\left(\Omega(k)(t-\tau)\right) \hat{F}(\mathbf{k},t) \exp(i\mathbf{k}\cdot\mathbf{x})\, d\tau d\mathbf{k}$$

Taking the condition $\zeta(\mathbf{x}=\mathbf{0},t) = s_0(t)$, we have the required relation between the known prescribed excitation signal $s_0(t)$ and a source function to be found

$$s_0(t) = \int_0^t \int \cos(\Omega(k)(t-\tau))\,\hat{F}(\mathbf{k},\tau)\,d\tau d\mathbf{k} \tag{2.25}$$

The essential steps to construct from this the source function are the same in 1D and 2D. But since the details are a bit different, we will first consider 1D and then 2D.

2.2.1 Generation in 1D

In this subsection we consider the 1D case of internal wave generation for a spatially extended source generation and a point source. By using (2.22) as the form of the source function $F(x,t)$, the relation (2.25) between excitation and source function can be rewritten as

$$s_0(t) = \int_0^t f(\tau) \int_{-\infty}^{\infty} \cos(\Omega(k)(t-\tau))\,\hat{\gamma}(k)\,d\tau dk \tag{2.26}$$

where $\hat{\gamma}(k)$ is the spatial Fourier transformation of $\gamma(x)$. In order to make it possible to exchange spatial and temporal information in Fourier space, we will change from the integration variable k to ω. Since wavenumber k and angular frequency ω are related by the dispersion relation $\omega = \Omega(k)$, it follows that $d\omega = V(\omega)\,dk$, where $V(\omega) = V_g(K(\omega))$, with $V_g(K(\omega)) = d\Omega/dk$ the group velocity. Here, $K(\omega)$ is the inverse of Ω:

$$k = K(\omega)\,, \quad \text{for } \omega = \Omega(k)$$

Changing the variable k to ω and assuming $\gamma(x)$ is even function, the relation between excitation and source function (2.26) reads

$$s_0(t) = \int_0^t f(\tau)\exp(i\omega\tau) \int_{-\infty}^{\infty} \exp(-i\omega t)\,\frac{\hat{\gamma}(K(\omega))}{V(\omega)}\,d\tau d\omega \tag{2.27}$$

By extending the integration of τ over the whole real axis, we obtain

$$s_0(t) = 2\pi \int_{-\infty}^{\infty} \check{f}(\omega)\,\frac{\hat{\gamma}(K(\omega))}{V(\omega)}\exp(-i\omega t)\,d\omega$$

where we use the temporal Fourier transformations of $f(t)$ given by

$$\check{f}(\omega) = \frac{1}{2\pi}\int_{-\infty}^{\infty} f(t)\exp(i\omega t)\,dt. \tag{2.28}$$

Hence, we arrive at the expression for the source function

$$F(x,t) = \gamma(x)\,f(t)\,, \quad \text{with } \check{f}(\omega) = \frac{V(\omega)}{2\pi\hat{\gamma}(K(\omega))}\check{s}(\omega) \tag{2.29}$$

This result holds for any choice of the function $\gamma(x)$. For the applications in this thesis, we use mainly a special case, namely: a point source generation. For point source generation, we take $\gamma(x) = \delta_{Dir}(x)$, where $\delta_{Dir}(x)$ is the Dirac delta function. Then $\hat{\gamma}(k) = 1/2\pi$ and the source function is given by

$$F_p(x,t) = \delta_{Dir}(x) . f(t), \quad \text{with } \check{f}(\omega) = V(\omega)\check{s}(\omega) \tag{2.30}$$

For extended function $\gamma(x)$, one special case is when the influx $f(t) = s(t)$, i.e. $f(t)$ is the original influx signal. Then from (2.29) it follows that

$$F_a(x,t) = \gamma(x) . s(t), \quad \text{with } \hat{\gamma}(k) = \frac{V_g(k)}{2\pi} \tag{2.31}$$

An illustration for the the extended function $\gamma(x)$ for the area generation is shown in Figure 2.4. In this illustration, $\gamma(x - x_0)$ with $x_0 = 10$ m from the OVBM with one (indicated by solid line) and three (indicated by solid with circle) profiles are compared.

To conclude the description of the 1D influx method, it should be noted that the influxing described here generates waves propagating symmetrically to the right and to the left, see Figure 2.5. This is because this forcing produces zero-velocity at the influx point. Hence the waveheight of the right-travelling wave will be half of the value as prescribed by the signal function $s_0(t)$. Stated differently, to influx a harmonic wave of amplitude 1 to the right, we should take for $s_0(t)$ the harmonic signal with amplitude 2.

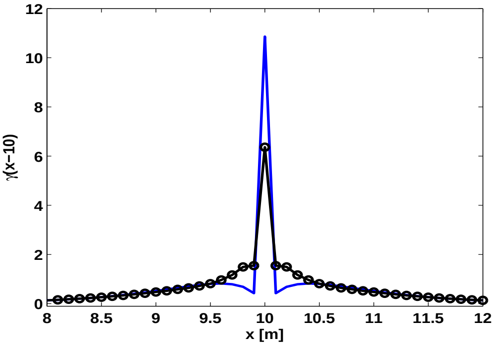

Figure 2.4: *An illustration for the extended function $\gamma(x - x_0)$ for the area generation function that is obtained for the dispersion relation of 1D OVBM with one profile (solid line) with $\kappa = 3.16$ and three profiles (solid with circle) with $\kappa_1 = 2.58$, $\kappa_2 = 11.24$ and $\kappa_3 = 21.45$ above $h = 1$ m.*

2.2.2 Generation in 2D

For the 2D case, we consider influx from a line source function. To simplify the problem, we consider the case of excitation at the y-axis of a monochromatic wave with frequency ω_0 under a fixed angle θ_0. The method to be described here can be generalized for broad spectrum waves by superposition.

Let k_0 denote the wavenumber related to ω_0 and $k_y^0 = k_0 \sin(\theta_0)$, $k_x^0 = k_0 \cos(\theta_0)$, with θ_0 the angle with the x-axis. Then the excitation at $x = 0$ is

$$s(y,t)\,|_{x=0} = a \exp\left(i\left(yk_y^0 - \omega_0 t\right)\right) \tag{2.32}$$

We will now determine a source function $F\left(\mathbf{x},t\right)$ of the form

$$F\left(\mathbf{x},t\right)=D\exp\left(i\left(yk_y^0-\omega_0 t\right)\right).g\left(x\right) \tag{2.33}$$

where $g\left(x\right)$ can be spatially extended in the x direction; a line source at the y-axis is obtained by taking $g\left(x\right)=\delta_{Dir}\left(x\right)$: so that

$$F\left(\mathbf{x},t\right)=D\exp\left(i\left(yk_y^0-\omega_0 t\right)\right).\delta_{Dir}\left(x\right) \tag{2.34}$$

Now the problem is to determine an expression for D.

The spatial Fourier transformation of the source function (2.33) is given by

$$\begin{aligned}\hat{F}\left(\mathbf{k},t\right)&=\left(\frac{1}{2\pi}\right)^2 D\exp\left(-i\omega_0 t\right)\int\int g\left(x\right)\exp\left(iyk_y^0\right).\exp\left(-i\mathbf{k}\cdot\mathbf{x}\right)d\mathbf{x}\\&=\left(\frac{1}{2\pi}\right)^2 D\exp\left(-i\omega_0 t\right).2\pi.\hat{g}\left(k_x\right)\int\exp\left(-iy\left(k_y-k_y^0\right)\right)dy\\&=D\exp\left(-i\omega_0 t\right).\hat{g}\left(k_x\right).\delta_{Dir}\left(k_y-k_y^0\right)\end{aligned} \tag{2.35}$$

In the second and third line we use $\hat{g}\left(k_x\right)=\frac{1}{2\pi}\int g\left(k_x\right)\exp\left(-ik_x.x\right)dx$ and $\delta_{Dir}\left(k_y-k_y^0\right)=\frac{1}{2\pi}\int\exp\left(-iy\left(k_y-k_y^0\right)\right)dy$, respectively. The relation between excitation and source function can be written as

$$\begin{aligned}a\exp\left(i\left(yk_y^0-\omega_0 t\right)\right)=&\int_0^t D\exp\left(-i\omega_0\tau\right)\int_0^\infty\int_0^\infty\cos\left(\Omega\left(t-\tau\right)\right)\\&\hat{g}\left(k_x\right).\delta_{Dir}\left(k_y-k_y^0\right)\exp\left(iyk_y\right)dk_x dk_y d\tau\end{aligned}$$

Extending the time integration interval to the whole real axis, there results

$$\begin{aligned}a\exp\left(-i\omega_0 t\right)&=\int_{-\infty}^\infty D\exp\left(-i\omega_0 t\right)\int_0^\infty\cos\left(\Omega_0\left(k_x\right)\left(t-\tau\right)\right).\hat{g}\left(k_x\right)dk_x d\tau\\&=\int_{-\infty}^\infty D\exp\left(-i\omega_0 t\right)\int_{-\infty}^\infty\frac{1}{2}\exp\left(-i\Omega_0\left(k_x\right)\left(t-\tau\right)\right).\hat{g}\left(k_x\right)dk_x d\tau\\&=\frac{1}{2}\int_{-\infty}^\infty\int_{-\infty}^\infty D\exp\left(-i\left(\Omega_0-\omega_0\right)\tau\right)\exp\left(-i\Omega_0 t\right).\hat{g}\left(k_x\right)dk_x d\tau\\&=\frac{1}{2}.2\pi D\int_{-\infty}^\infty\delta_{Dir}\left(\Omega_0-\omega_0\right)\exp\left(-i\Omega_0 t\right).\hat{g}\left(k_x\right)dk_x\end{aligned} \tag{2.36}$$

where $\Omega_0\left(k_x\right)=\Omega\left(\sqrt{k_x^2+\left(k_y^0\right)^2}\right)$. In the second line of (2.36), the factor 1/2 appears in the process to write the integral over the whole real axis. In the fourth line of (2.36), the property of the delta Dirac function is used. With

$$\frac{\partial\Omega}{\partial k_x}=V\left(\omega\right)\frac{k_x}{\sqrt{k_x^2+\left(k_y^0\right)^2}}$$

we can rewrite (2.36) by change of integration variable k_x to ω

$$\begin{aligned} a\exp\left(-i\omega_0 t\right) &= \pi D\int_{-\infty}^{\infty}\delta_{Dir}\left(\omega-\omega_0\right)\exp\left(-i\omega t\right).\hat{g}\left(k_x\right)\frac{\partial k_x}{\partial\Omega_0}d\omega \\ &= \pi D\exp\left(-i\omega_0 t\right)\frac{\hat{g}\left(k_x^0\right)}{V\left(\omega_0\right)\cos\left(\theta_0\right)} \end{aligned}$$

From this follows that the source function is given by (2.33) with D given by

$$D=\frac{a\exp\left(-i\omega_0 t\right).V\left(\omega_0\right)\cos\left(\theta_0\right)}{\hat{g}\left(k_x^0\right).\pi}.$$

The y-axis is a line source if we choose $g\left(x\right)=\delta_{Dir}\left(x\right)$. Then the force function for line generation is given by

$$F_{L0}\left(x,t\right)=2a\exp\left(-i\omega_0 t\right).V\left(\omega_0\right)\cos\left(\theta_0\right).\delta_{Dir}\left(x\right) \tag{2.37}$$

The force function (2.37) is the same as given by Kim et al. [2007] which was derived by using the Green function method.

The force function (2.37) can be generalized for a (broad band) spectrum, e.g. waves with frequency $\omega_0\in[0,\omega_{max}]$, as

$$F_{S0}\left(x,t\right)=2\int_0^{\omega_{max}}a(\omega_0)\exp\left(-i\omega_0 t\right).V\left(\omega_0\right)\cos\left(\theta_0\right).\delta_{Dir}\left(x\right)d\omega_0 \tag{2.38}$$

where $a(\omega_0)$ is the amplitude of waves with frequency ω_0.

In the next subsection we apply the method of embedded influxing for 1D with the area generation (2.31), and 2D with the line influxing (2.37) for a Finite Element implementation of OVBM.

2.2.3 Finite Element implementation for Embedded Influxing

For 1D OVBM with a point source excitation at $x=x_0$, the dynamic equations of the OVBM in (1.20) are given by

$$\begin{cases}\partial_t\eta &= -\partial_x\left[\left(h+\eta\right)\partial_x\phi\right]-\partial_x\left[\beta\cdot\Psi\right]+2\gamma(x-x_0)f\left(t\right)\\ \partial_t\phi &= -g\eta-\left(\partial_x\phi\right)^2/2\end{cases} \tag{2.39}$$

For point source generation, $\gamma(x-x_0)=\delta_{Dir}(x-x_0)$, the function f is given by $\check{f}\left(\omega\right)=V\left(\omega\right).\check{s}\left(\omega\right)$, while for 1D area generation with $f(t)=s(t)$, $\gamma(x)$ is given by $\hat{\gamma}(k)=V_g(k)/2\pi$.

We will illustrate the Finite Element implementation for 1D area generation for OVBM (2.39). The resulting matrix system is then given by

$$\begin{cases}M\partial_t\bar{\eta} &= \mathbf{D}\bar{\phi}+\bar{b}\left(\bar{\eta},\bar{\phi}\right)+B\left(\beta\right)\cdot\underline{\Psi}+2M\bar{\gamma}.s\left(t\right)\\ M\partial_t\bar{\phi} &= -gM\eta-\bar{v}\left(\bar{\phi}\right)\end{cases} \tag{2.40}$$

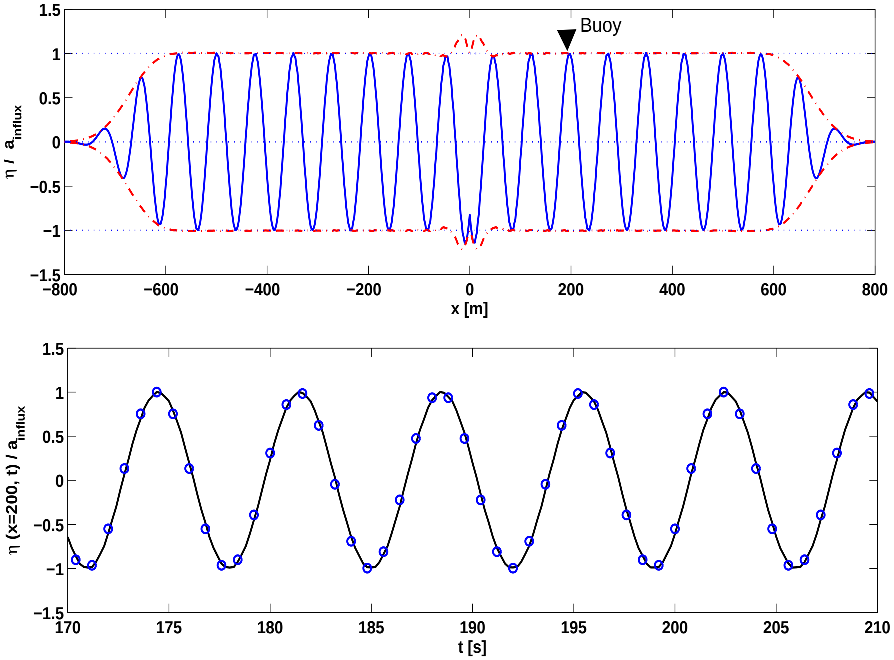

Figure 2.5: *An illustration of area generation for 1D OVBM. In the upper plot, a snapshot is shown of monochromatic waves with period of* 7 *s that are generated at* $x = 0$ *m above constant bottom* $h = 30$ *m. In the lower plot, the comparison of the signal of the simulation (solid) and of the analytical solution (dots) at* $x = 200$ *m is shown. Notice that the surface elevation* η *above is normalized with the amplitude of input signal* a_{influx}.

where $\bar{\gamma}$ is the vector of the discretized function $\gamma(x)$.

In the upper plot of Figure 2.5, a snapshot of the influxing of monochromatic waves with period of 7 s that are generated using the area generation (2.39) at $x = 0$ m above a constant bottom $h = 30$ m, is shown. The waves are damped in the damping zones at $x \in [-800, -600]$ and $x \in [600, 800]$. In the lower plot of Figure 2.5, the measured signal from the simulation is compared with the solution at $x = 200$ m. From this plot, it can be seen that the amplitude and period of the simulation agree very well with the solution.

Implementation of the embedded influxing method in 2D OVBM is similar with the 1D version. For a given initial signal at $y = y_0$, the 2D line source generation for the OVBM is given by

$$\begin{cases} \partial_t \eta & = -\nabla\left[(h+\eta)\nabla\phi\right] - \nabla\left[\beta\cdot\nabla\Psi\right] + F_L \\ \partial_t \phi & = -g\eta - \left|\nabla\phi\right|^2/2 \end{cases} \tag{2.41}$$

where $F_L = \int_B F_{L0}(x-b,t)\,db$, with $b \in B$, where B is the (part of) the y-axis line influxing and F_{L0} is defined in (2.37). The Finite Element implementation in 2D is then given by

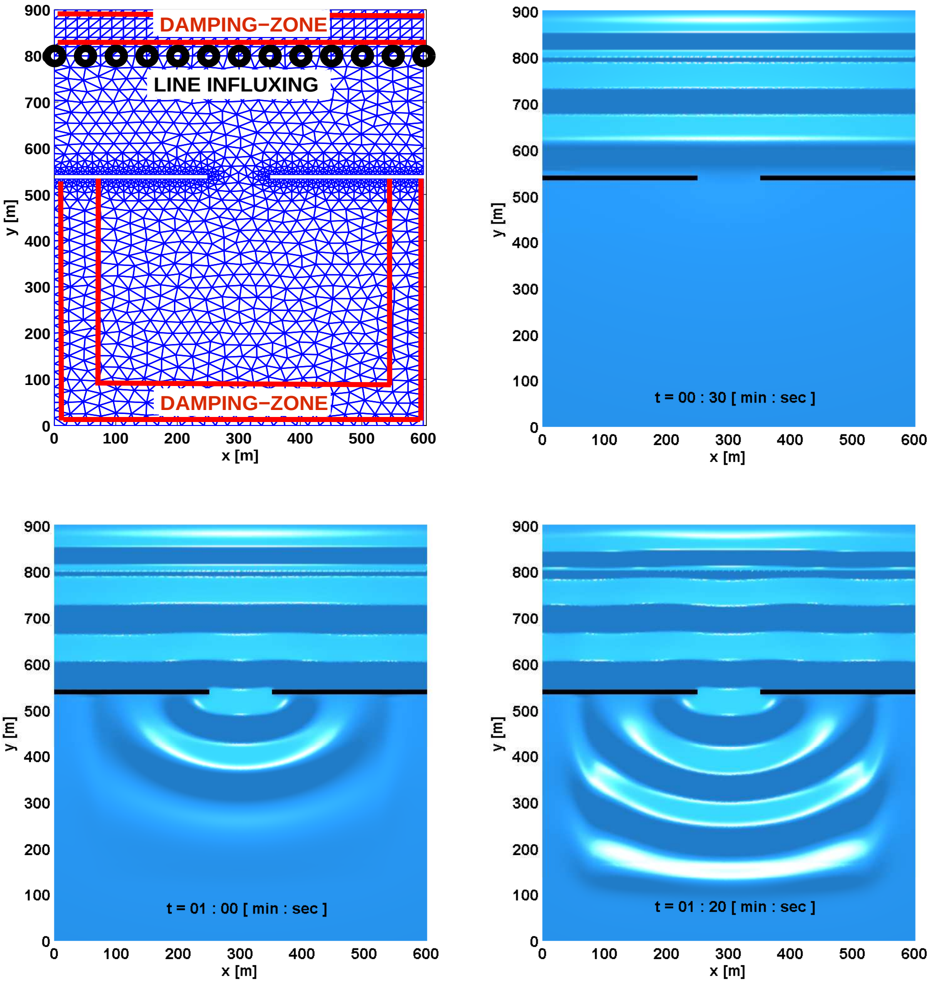

Figure 2.6: *The numerical setting for simulations of 2D OVBM is indicated in the upper left plot, for line influxing at* $y = 800$ *m. Snapshots of the simulations at* $t = 30$ *s (upper right),* 60 *s (lower left),* 80 *s (lower right).*

$$\begin{cases} M\partial_t\bar{\eta} & = \mathbf{D}\bar{\phi} + \bar{b}\left(\bar{\eta}, \bar{\phi}\right) + B\left(\beta\right) \cdot \underline{\Psi} + M^1\bar{F}_L \\ M\partial_t\bar{\phi} & = -gM\eta - \bar{v}\left(\bar{\phi}\right) \end{cases} \tag{2.42}$$

with M^1 is the mass-matrix in 1D with elements $M^1_{ij} = \int T_i\left(x\right) T_j\left(x\right) dx$.

We illustrate the line influxing 2D OVBM for wave propagation through a slit in Figure 2.6. This example shows that reflections from the wall do not influence the generation mechanism. Monochromatic waves with period of $T = 10$ s are influxed uniformly with a line generation at $y = 800$ m above a constant bottom $h = 20$ m. In the upper left plot of Figure 2.6, the numerical setting for the simulation is indicated: damping-zones are placed at the north-side of the line to damp also the reflected waves from fully reflective wall at $y = 530$ m, and inside the rectangle domain below the wall at all sides. Since the wavelength of the generated waves is 121 m, for the simulations a grid size of approximately 10 m is used. This grid size is finer than indicated in upper left plot of Figure 2.6. In the upper right plot and lower plots of Figure 2.6, snapshots of simulations at $t = 30$, 60 and 80 s are shown. From these plots, the diffraction pattern is clearly seen after the waves propagate through the slit.

The performance of the 2D-code in representing effects of diffraction, refraction and shoaling will be shown in Chapter 4. In that chapter, the 2D-code is tested against the experiment of Berkhoff et al. [1982]. Illustrations for influxing more complicated waves in 2D under an angle will be shown in Chapter 5.

Appendix 2.A

A basis function for a 2D Finite Element triangular grid is illustrated in the right plot of Figure 2.1. Now we will describe an explicit expression for the basis function $T_i(\mathbf{x})$. Note that $T_i(\mathbf{x})$ has a strict local character, i.e. it has value one at node-i and zero at other points. In order to construct a linear polynomial which is defined on each triangle we need three parameters. A natural choice is to use the function values in the three vertices (nodes) of the triangles, e.g. (x_1, y_1), (x_2, y_2) and (x_3, y_3) . The linear polynomial is defined by

$$T_i(\mathbf{x}) = \frac{a_i + b_i x + c_i y}{2\Delta} \tag{2.43}$$

where

$$\Delta = \frac{1}{2}\begin{vmatrix} 1 & x_1 & y_1 \\ 1 & x_2 & y_2 \\ 1 & x_3 & y_3 \end{vmatrix} = \frac{1}{2}\left[(x_2 - x_1)(y_3 - y_2) - (y_2 - y_1)(x_3 - x_2)\right]$$

is the area of the triangle. To obtain an explicit expression for $T_i(\mathbf{x})$, the three unknowns: a_i, b_i and c_i in (2.43) has to be determined from three points: (x_1, y_1), (x_2, y_2) and (x_3, y_3). By assuming $T_i(\mathbf{x} = (x_1, y_1)) = 1$ and zero at the other vertices, we have

$$\begin{aligned} 1 &= a_i + b_i x_1 + c_i y_1 \\ 0 &= a_i + b_i x_2 + c_i y_2 \\ 0 &= a_i + b_i x_3 + c_i y_3 \end{aligned}$$

Then the values of the the coefficients a_i, b_i and c_i are given by

$$\begin{aligned} a_i &= x_2 y_3 - x_3 y_2 \\ b_i &= y_2 - y_3 \\ c_i &= x_3 - x_2 \end{aligned}$$

This provides the explicit expression for $T_i(\mathbf{x})$.

Chapter 3

Optimized Variational 1D Boussinesq modelling of coastal waves propagating over a slope[1]

Abstract

The Variational Boussinesq Model (VBM) for waves is based on the essential property that wave phenomena can be exactly described as a Hamiltonian system. In the VBM, the fluid potential in the expression of the kinetic energy is approximated by its value at the free surface plus a linear combination of vertical potential profiles with horizontal spatially dependent functions as coefficients. The vertical potential profiles are chosen a priori and determine completely the dispersive properties of the model. For signalling problems above varying bottom we show how to optimize the wave number of one or more Airy functions as vertical profiles, by minimizing the kinetic energy functional for the given influx signal. The performance of a finite element implementation with piecewise linear basis functions is investigated by comparing simulations with experimental data from MARIN hyrodynamic laboratory for bichromatic and irregular waves running over a sloping bottom. The conclusion is that this code is robust and remarkably accurate and efficient.

---

[1] Published as:
D. Adytia and E. van Groesen. Optimized Variational 1D Boussinesq modelling of coastal waves propagating over a slope. *Coast. Eng.*, 64:139-150, 2012.

3.1 Introduction

Modern day activities in the near shore area require reliable simulations of the waves coming from the deep ocean or sea to the shallower parts near the coast. Among these activities are gas and oil exploitation, fields of wind mills, with offshore constructions that have to be designed and constructed to be able to withstand wave forces that can be calculated once the waves have been modelled. For sustainable development of the coastal area, the effects have to be calculated of waves on sedimentation and coastal erosion and for the design of harbours. But simulations of waves in coastal area are not easy, since three major physical effects are involved and interact with each other in a complicated way: effects of nonlinearity, of dispersion and of the bathymetry. In this paper we will formulate and test a Finite Element implementation of a variational wave model that will be shown to be capable to perform such simulations.

Many surface water waves models used in coastal engineering applications are Boussinesq type models. Since the idea was introduced by Boussinesq [1872], the main challenges still remain the same until now: the accuracy in dispersiveness and nonlinearity. The most common way to derive such Boussinesq-type models is by introducing small parameter expansion techniques in the full set of water wave equations (see Kirby [1997] and Madsen and Fuhrman [2010] for reviews). The higher-order expansion leads to higher-order derivatives (at least third-order) in a resulting Boussinesq-type model. As a consequence, the numerical implementation becomes more complex. A rather different approach in deriving Boussinesq-type models is via the variational formulation for surface water waves. One of them is the Variational Boussinesq Model (VBM) that was introduced by Klopman et al. [2005, 2007, 2010].

The VBM is based on the essential property that wave phenomena can be exactly described as a Hamiltonian system in variables at the free surface. As introduced in Klopman et al. [2005, 2007, 2010], Boussinesq-type equations can be obtained by taking an approximation for the fluid potential using its value at the free surface plus a linear combination of vertical potential profiles with horizontal spatially dependent functions as coefficients. The vertical potential profiles are chosen a priori while the horizontal functions have to satisfy a system of linear elliptic equations which have to be solved together with the dynamic equations. Boussinesq equations for which additional elliptic equations have to solved are not new, as can be found in Whitham [1997], Broer [1975].

Despite the fact that an additional elliptic equation has to be solved, the resulting model is quite simple because the highest derivatives are of second-order and no mixed temporal-spatial derivatives appear. As a consequence, the numerical implementation is much easier than the implementation of higher-order Boussinesq-type models, e.g. Wei et al. [1995], Agnon et al. [1999], Madsen et al. [2003] and Lynett and Liu [2004b]. Moreover, since the VBM is derived in a consistent way from the variational structure, the VBM energy is conserved and given by a positive Hamiltonian (see Klopman et al. [2010]). Non-positivity of the Hamiltonian may lead to instabilities (see Broer [1974], Broer et al. [1976], Milder [1990] and Yoon and Liu [1994]).

For the applications treated in Klopman et al. [2010], such as periodic waves and confined wave groups propagating over a flat or sloping bottom, it turns out that one vertical profile is sufficient to capture the essential phenomena. In Lakhturov, Adytia, and van Groesen [2012], for wave fields with a broad spectrum, such as a focusing wave group propagating over a flat bottom, it was shown that one vertical potential profile is not good enough to describe the propagation accurately. Therefore, for such applications the VBM with multiple vertical potential profiles was used and an optimization criterion was formulated to select profiles that lead to the best possible dispersive properties.

In this paper, we show the general form of the VBM with multiple vertical profiles and a criterion to optimize such profiles for propagation above a sloping bottom. This variant will be called Optimized VBM for sloping bottom. Consistent with the derivation of the model via the variational formulation, this model will be implemented in a Finite Element method.

To show the performance of the model we simulated two test cases: bichromatic and irregular waves which propagate over a 1/20 slope from a water depth of $30m$ to $15m$. Accurate data are available of experiments performed at MARIN hydrodynamics laboratory in Wageningen, The Netherlands. For the bichromatic case with narrow spectrum accurate numerical simulations with only one vertical potential profile will be presented. For the irregular wave with broad spectrum, we will show that results of VBM with one profile are rather poor, but much better for simulations with two optimal profiles.

In section 2, we describe the derivation of the VBM with multiple vertical potential profiles and an optimization criterion to get the optimal Airy profiles for a sloping bottom. In section 3, the finite element implementation for the model will be described. The simulations results of the model for both test cases are described in section 4. Section 5 provides some conclusions and comments.

3.2 Variational Boussinesq Model

3.2.1 Vertical structure in the variational principle

The VBM is based on the variational principle for water waves in Luke [1967], and leads to equations in Hamiltonian form as discovered earlier Zakharov [1968], Broer [1974], Miles [1977], see also Milder [1977]. In the VBM introduced in Klopman et al. [2005, 2007, 2010] the vertical structure of the flow in the kinetic energy of the Hamiltonian is approximated by a (series of) vertical shape function(s) that have to be chosen in advance. The Hamiltonian is the total energy, which is the sum of the kinetic energy

$$K\left(\phi,\eta\right)=\int_{\mathbf{x}}\int_{-h}^{\eta}\frac{1}{2}\left|\nabla_3\Phi\right|^2 dzd\mathbf{x} \tag{3.1}$$

and the potential energy

$$P=\frac{1}{2}\int g\eta^2 d\mathbf{x} \tag{3.2}$$

where $\eta(\mathbf{x},t)$ is the surface elevation, $\Phi\left(\mathbf{x},z,t\right)$ is the fluid potential in the interior of the fluid layer and $h\left(\mathbf{x}\right)$ is the water depth. The horizontal and vertical coordinates are $\mathbf{x}=\left(x_1,x_2\right)^T$ and z, respectively. We use as canonical variables to describe the dynamics of the flow the surface elevation $\eta\left(\mathbf{x},t\right)$ and the fluid potential at the free surface $\phi\left(\mathbf{x},t\right)$.

Luke's variational principle Luke [1967] uses the Lagrangian $\mathcal{L}\left(\eta,\Phi\right)$

$$\mathcal{L}(\eta,\Phi) = -\int\int\left\{\int_{-h}^{\eta}\partial_t\Phi + \frac{1}{2}\left|\nabla_3\Phi\right|^2 + \frac{1}{2}gzdz\right\}d\mathbf{x}dt.$$

By using Leibniz integral rule, and neglecting dynamically uninteresting terms, there results a Lagrangian that depends on the surface variables

$$\mathcal{L}(\eta,\phi) = \int\left[\int\int\left(\phi\partial_t\eta\right)d\mathbf{x} - H\left(\phi,\eta\right)\right]dt \tag{3.3}$$

with $H = K(\phi,\eta) + P(\eta)$, see Miles [1977]. By taking variations with respect to ϕ and η, the Hamiltonian equations are found

$$\partial_t\eta = \delta_\phi H\left(\phi,\eta\right), \partial_t\phi = -\delta_\eta H\left(\phi,\eta\right), \tag{3.4}$$

where $\delta_\phi H$ and $\delta_\eta H$ denote the variational derivatives of H with respect to ϕ and η respectively. These equations describe the dynamics of the water waves. The exact formulation will be obtained if we could assure that the fluid potential Φ satisfies the Laplace equation in the fluid interior, the impermeability condition at the bottom $z = -h(\mathbf{x})$ and the condition $\Phi = \phi$ at the free surface $z = \eta$. Unfortunately it is not easy to express K explicitly in the surface variables η and ϕ. Nevertheless, the steps above make it possible to take an approximation for the Hamiltonian. By inserting the approximation into the Lagrangian (3.3), we obtain a consistent approximation while keeping the consequences of the exact formulation, such as energy conservation.

In the VBM as described in Klopman et al. [2010], the vertical structure of the fluid potential Φ in the kinetic energy (3.1) is approximated by its value at the surface and multiple expansion terms as :

$$\Phi\left(\mathbf{x},z,t\right) \approx \phi\left(\mathbf{x},t\right) + \Sigma_m F_m(z)\psi_m(\mathbf{x},t) = \phi\left(\mathbf{x},t\right) + F(z)\cdot\Psi(\mathbf{x}) \tag{3.5}$$

where F and Ψ are vector functions. Note that the condition $\phi(\mathbf{x},t) = \Phi(\mathbf{x},z=\eta,t)$ has to be assured to keep the canonical structure of the Hamiltonian. As a consequence, it is required that $F_m(z=\eta) = 0$. Also, to satisfy the bottom impermeability condition, we assume the bottom is slowly varying, so that the requirement $F_m^{'}(z=-h) = 0$ is sufficiently accurate. The vertical profile functions $F_m(z)$ have to be chosen in advance and $\psi_m(\mathbf{x})$ are functions that have to satisfy the optimality condition of vanishing of the variation of the kinetic energy with respect to ψ_m. This variation leads to a system of linear elliptic equations that has to be solved together with the dynamics for the variables η and ϕ, as we shall see below. Notice that the expansion (3.5) is different from the Green-Naghdi theory, as described in Green and Naghdi [1976], where a polynomial expansion is used to describe the vertical flow. In that method, the flow is allowed to be rotational while for VBM we restrict to irrotational motions.

Since this paper will only consider test cases for 1D, we restrict the equations to 1D from now on. By substituting the approximation (3.5) into the kinetic energy (3.1), we obtain

$$\begin{aligned} K_{vbm} &= \frac{1}{2}\int\int_{-h}^{\eta} [\partial_x\phi + \partial_x(F\cdot\Psi)]^2 + (F'\cdot\Psi)^2 dz dx \\ &\approx \frac{1}{2}\int\int_{-h}^{\eta} [\partial_x\phi + F\cdot\partial_x\Psi]^2 + (F'\cdot\Psi)^2 dz dx \\ &= \frac{1}{2}\int \left[(h+\eta)(\partial_x\phi)^2 + 2\partial_x\phi\beta\cdot\partial_x\Psi + \partial_x\Psi\cdot\alpha\partial_x\Psi + \Psi\cdot\gamma\Psi\right] dx \end{aligned} \tag{3.6}$$

In the second line, to simplify the problem, we assume that the vertical profile F_m is slowly varying with respect to η and h so that the contribution of the term $\Psi\cdot\partial_x F$ is small and can be neglected; in Klopman et al. [2005], the resulting equations are called *weakly-nonlinear*. In the last expression, we introduced the matrices α and γ, and the vector β which have elements that depend on the vertical profiles F_m

$$\alpha_{ij} = \int_{-h}^{\eta} F_i F_j dz; \quad \gamma_{ij} = \int_{-h}^{\eta} F_i' F_j' dz; \quad \beta_i = \int_{-h}^{\eta} F_i dz \tag{3.7}$$

The explicit expressions for these coefficients are given in the Appendix. With the kinetic energy expression (3.6), variations of the Lagrangian with respect to ϕ, η, and ψ_m give rise to the following system of PDE

$$\begin{cases} \partial_t\eta & = -\partial_x((h+\eta)\partial_x\phi) - \partial_x(\beta\cdot\partial_x\Psi) \\ \partial_t\phi & = -g\eta - \frac{1}{2}\partial_x\phi^2 \\ -\partial_x(\alpha\partial_x\Psi) + \gamma\Psi & = \partial_x(\beta\partial_x\phi) \end{cases} \tag{3.8}$$

As it turns out, the quality of the model is highly determined by the choice of the vertical profile functions. In Klopman et al. [2010], the VBM was characterized by two choices of the vertical profiles. The first one is parabolic profile which is sufficiently good for relatively long wave. A second choice is a profile as in Airy linear potential theory, a cosine hyperbolic function:

$$F_m\left(z;\eta,h\right) = \frac{\cosh(\kappa_m\left(z+h\right))}{\cosh\left(\kappa_m\left(\eta+h\right)\right)} - 1 \tag{3.9}$$

which has exact phase and group velocities for infinitesimal waves with wavenumber κ_m. Therefore, for periodic waves, Airy profile is the best choice by choosing κ the same as the wavenumber of the periodic wave. But for a broad spectrum such as focusing wave group or irregular waves, the form (3.9) can at best be approximative. In the rest of this paper, we will only use this type of profiles and refer to them as Airy profiles.

The exact dispersion of linear surface waves is given by

$$\Omega\left(k\right) = sign\left(k\right)\sqrt{gk\tanh\left(kh\right)} \tag{3.10}$$

where $\Omega(k) = \omega$ denotes the angular frequency [Rad/s] and k the wavenumber. The dispersion relation of the linearized VBM (3.8) above flat bottom can be calculated and is given by

$$\Omega_{vbm}\left(k\right) = kc_0\sqrt{\left[1 - \frac{k^2}{h}\beta\cdot\left(\alpha k^2+\gamma\right)^{-1}\beta\right]} \tag{3.11}$$

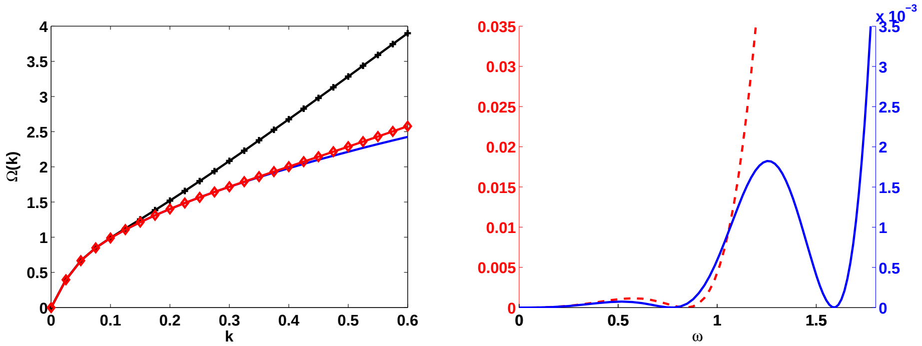

Figure 3.1: *The dispersion relation of the VBM with one vertical profile (denoted by solid line with cross), two vertical profiles (denoted by solid line with diamonds) and the exact dispersion (solid line) are compared in the left plot at a depth $h = 30m$. The right plot shows the difference between the dispersion relation of the VBM with one vertical profile and the exact dispersion (dashed line, left hand axis) and the VBM with two vertical profiles and the exact dispersion (solid line, right hand axis). These plots are, by way of example, for the optimal choices of vertical profiles for the test case of irregular waves to be shown in section 3.4 and are obtained from the optimization criterion to be described in subsection 2.2.*

where $c_0 = \sqrt{gh}$ is the speed of long waves. Here, it is assumed that all values κ_m are different so that the matrix $\alpha k^2 + \gamma$ is invertible.

Besides the choice of κ_m in the Airy profiles (3.9), the number of vertical potential profiles in the approximation of the VBM (3.5) plays a significant role in the dispersive quality of the model. This is illustrated in Figure 3.1, showing the VBM dispersion relation with one and two vertical profiles compared to the exact dispersion relation. In this illustration, the values of κ_m for the Airy profiles are $\kappa = 0.074$ (or $\omega = 0.84$) for the one vertical profile VBM, and $\kappa_1 = 0.064$ and $\kappa_2 = 0.26$ (or $\omega_1 = 0.77$ and $\omega_2 = 1.59$) for the two vertical profiles VBM, at a depth $h = 30m$. When dealing with a wave with broad spectrum with frequency $\omega \in [0, 1.5]$, using two vertical profiles already gives a 10 times more accurate dispersion relation compared to the VBM with one vertical profile, as is shown in the right plot of Figure 3.1.

The approximation of the fluid potential Φ in (3.5) with Airy profiles (3.9) is not new. Similar expansions have been used in Nadaoka et al. [1997], Athanassoulis and Belibassakis [1999] and Belibassakis and Athanassoulis [2011] to obtain Boussinesq-type models. But the way how to derive the model and to choose the wavenumber(s) for the Airy profiles (3.9) is different.

3.2.2 Optimization of the vertical profiles

Since we consider signalling problems in this paper, we can exploit the information from the initial signal to find optimal values for κ in the Airy profile(s). Here, we simplify the problem to be linear and the bottom to be constant; hereafter we will show the application of the method for a varying bottom. Following Lakhturov et al. [2012], we observe that the kinetic energy functional at a certain depth $h = h_0$ can be written for any linear dispersion wave equation as

$$K(\phi) = \frac{1}{2g}\int |\Omega\phi|^2\, dx = \frac{1}{4\pi g}\int \left|\Omega\hat{\phi}\right|^2 dk \tag{3.12}$$

where $\hat{\phi}$ is the spatial Fourier transform of ϕ. Now, let an input signal $\eta_0 = \eta(x_0, t)$ at the influx point x_0 be given, and let $\widehat{\eta_0}(k)$ denote its spatial Fourier transform. The uni-directional evolution of the waves is given by $\partial_t\phi = -i\Omega\phi$. Combined with the dynamic equation $\partial_t\phi = -g\eta$, we obtain a relation between the initial surface elevation and the initial surface potential $\widehat{\phi_0}$

$$i\Omega(k)\,\widehat{\phi_0}(k) = g\widehat{\eta_0}(k)$$

It follows that we can express the kinetic energy (3.12) as

$$K = \frac{g}{4\pi}\int |\widehat{\eta_0}(k)|^2 dk \tag{3.13}$$

For uni-directional propagation, it holds that

$$\eta(x,t) = \int \widehat{\eta_0}(k)\, e^{i(kx-\Omega(k)t)} dk = \int \widetilde{\eta_0}(\omega)\, e^{i(\Omega^{-1}(\omega)x-\omega t)} d\omega \tag{3.14}$$

where $\widetilde{\eta_0}(\omega)$ is the temporal Fourier transform of η and $\Omega^{-1}(\omega)$ denotes the inverse of function $\Omega(k)$. Since $d\omega = V(k)\,dk$, where $V(k) = d\Omega(k)/dk$ is the group velocity, we get $\widehat{\eta_0} = V(k)\widetilde{\eta_0}(\omega)$, and the kinetic energy (3.13) can be rewritten as

$$K = \frac{g}{4\pi}\int |\widetilde{\eta_0}(\omega)|^2 V(\omega)\, d\omega = \frac{g}{2}\int S(\omega)\, V(\omega)\, d\omega \tag{3.15}$$

where

$$S(\omega) = \frac{\widetilde{\eta_0}(\omega)\cdot \widetilde{\eta_0^*}(\omega)}{2\pi} \tag{3.16}$$

is the power spectrum.

As a direct consequence of the minimization property of the kinetic energy:

$$K(\phi) = \min_{\Phi=\phi \text{ at } z=0} \frac{1}{2}\int\int |\nabla\Phi|^2 dz dx$$

the kinetic energy functional for exact dispersion will always be less than any approximation. For the VBM approximation with parameters κ_m in the vertical profiles, the kinetic energy for the VBM is given by

$$K_{vbm}(\kappa_m) = \frac{g}{2}\int S(\omega)\, V(\omega, \kappa_m)\, d\omega$$

where $V(\omega;\kappa_m)$ is the group velocity corresponding to (3.11). To obtain a model with the best possible dispersion, we minimize $K_{vbm}(\kappa_m)$ with respect to all possible κ_m, or equivalently :

$$\min_{\kappa_m}[K_{vbm} - K_{ex}] = \min_{\kappa_m}\left\{\frac{g}{2}\int S(\omega)\left[V(\omega,\kappa_m) - V_{ex}(\omega)\right] d\omega\right\}$$

For varying bottom, the minimization above should be applied for every depth since the group velocity depends on the depth

$$\min_{\kappa_m}\left[K_{vbm}(h) - K_{ex}(h)\right] = \min_{\kappa_m}\left\{\frac{g}{2}\int S(\omega)\left[V(\omega,\kappa_m,h) - V_{ex}(\omega,h)\right]d\omega\right\} \qquad (3.17)$$

Although the spectrum $S(\omega)$ actually changes with depth, we will neglect that in the following. This optimized variant of the VBM will be called the Optimized VBM (OVBM).

3.3 Numerical implementation

Consistent with the derivation of the model via the variational formulation, OVBM will be implemented in a finite element method. In this implementation, we discretize the solutions in space, leading to a matrix system of ordinary differential equations (ODEs) which are solved in time using a Runge-Kutta method as ODE-solver in MATLAB. The system of linear elliptic equations for Ψ (3.8) has to be solved at each time level.

We start with the discretization of the variables on a grid of n points $\{x_k\}$ using piecewise linear local basis functions; this is possible, since the highest spatial derivatives in (3.6) are of first order. The expression of these tent functions is given by $T_k(x) = \max\{|x - x_k|/\Delta x, 0\}$ where Δx is the grid size. To discretize the variables in space, the coefficients will depend on time, i.e. $\eta(x,t) \approx \Sigma_{i=1}^{n}\eta_i(t)\,T_i(x) = \bar\eta(t)\cdot T(x)$, where $\bar\eta$ and T are vector functions. Similar notation is used for ϕ and Ψ.

Now, we substitute these approximations directly into the action principle (3.3) with the Hamiltonian for VBM:

$$\mathcal{L}_{vbm} = \int\left[\int(\phi\partial_t\eta)\,dx - H_{vbm}(\eta,\phi,\Psi)\right]dt \qquad (3.18)$$

where $H_{vbm}(\eta,\phi,\Psi) = P + K_{vbm}$ is given by (3.2) and (3.6). The first term in (3.18) becomes

$$\int(\phi\partial_t\eta)dx \approx \sum_{i,j}\phi_i\dot\eta_j M_{i,j} = M\bar\phi\cdot\partial_t\bar\eta \qquad (3.19)$$

where M is the so-called *mass matrix* with elements $M_{i,j} = \int T_i(x)T_j(x)dx$, and $\dot\eta_j$ denotes the derivative of η_j with respect to t. The second term in (3.18) becomes

$$\begin{aligned}\bar H_{vbm}(\bar\eta,\bar\phi,\underline{\Psi}) = {} & \frac{1}{2}gM\bar\eta\cdot\bar\eta + \frac{1}{2}\mathbf{D}\bar\phi\cdot\bar\phi + \bar H_3(\bar\eta,\bar\phi) + \mathbf{B}\cdot\underline{\Psi} \\ & + \frac{1}{2}\mathbf{A}\underline{\Psi}\cdot\underline{\Psi} + \frac{1}{2}\mathbf{G}\underline{\Psi}\cdot\underline{\Psi}\end{aligned}$$

where $\mathbf{D}$ and $\mathbf{A}$ are so-called *stiffness-matrices* with elements depend on h and α respectively: $\mathbf{D}_{i,j} = \int h(x)T_i^{'}(x)T_j^{'}(x)$, $\mathbf{A}_{i,j} = \int \alpha(x)T_i^{'}(x)T_j^{'}(x)dx$. $\mathbf{G}$ is the mass matrix that depends on γ: $\mathbf{G}_{i,j} = \int\gamma(x)T_i(x)T_j(x)dx$. $\mathbf{B}$ is the column vector :

$$\mathbf{B} = \left[B(\beta_1)\bar\phi, B(\beta_1)\bar\phi, \cdots, B(\beta_N)\bar\phi\right], \text{ with } B(\beta_i) = \int\beta_i(x)T_i^{'}(x)T_j^{'}(x)dx$$

and $\bar{H}_3(\bar{\eta},\bar{\phi})$ is the nonlinear cubic term:

$$\bar{H}_3(\bar{\eta},\bar{\phi}) = \frac{1}{2}\sum_{i,j,k}\eta_i\phi_j\phi_k C_{ijk}, \text{ with } C_{ijk} = \int T_i(x)T_j^{'}(x)T_k^{'}(x)dx$$

Now the Lagrangian (3.18) becomes a Lagrangian with vector state variables $(\bar{\eta},\bar{\phi},\underline{\Psi})$:

$$\int \left[M\bar{\phi}\cdot\partial_t\bar{\eta} - \bar{H}(\bar{\eta},\bar{\phi},\underline{\Psi})\right] dt \tag{3.20}$$

From this we find the Hamiltonian equations as the matrix system

$$\begin{aligned} M\partial_t\bar{\eta} &= \partial_{\bar{\phi}}\bar{H}_{vbm} = \mathbf{D}\bar{\phi} + \bar{b}(\bar{\eta},\bar{\phi}) + B(\beta)\cdot\underline{\Psi} \\ M\partial_t\bar{\phi} &= -\partial_{\bar{\eta}}\bar{H}_{vbm} = -gM\bar{\phi} - \bar{v}(\bar{\phi}) \end{aligned} \tag{3.21}$$

and an additional matrix system of linear elliptic equations from $\partial_{\underline{\Psi}}\bar{H}_{vbm} = 0$:

$$[\mathbf{A}+\mathbf{G}]\underline{\Psi} = -\mathbf{B} \tag{3.22}$$

Above, $\bar{b}(\bar{\eta},\bar{\phi})$ and $\bar{v}(\bar{\phi})$ are column vectors with elements

$$\begin{aligned} b_j(\bar{\phi},\bar{\eta}) &= \partial_{\phi_j}\bar{H}_3(\bar{\eta},\bar{\phi}) = \sum_{i,k}\eta_i\phi_k C_{ijk} \\ v_j(\bar{\phi}) &= \partial_{\eta_j}\bar{H}_3(\bar{\eta},\bar{\phi}) = \frac{1}{2}\sum_{i,k}\phi_i\phi_k C_{jik} \end{aligned}$$

The algorithm to obtain numerical solutions for the system (3.21) and (3.22) by time stepping can be described as follows. For given initial conditions η_0 and ϕ_0, we calculate Ψ_1 by solving the elliptic system in (3.22). Then by using the new Ψ_1, we solve the dynamic system in (3.21) using a time integrator, a Runge-Kutta method (or ODEsolver in MATLAB) to obtain new η_1 and ϕ_1. These steps can be repeated until the desired end-time.

Note that the matrix system (3.22) can become very large if many vertical profiles and many grid points are used. But since we use a finite element implementation with simple local basis functions, the resulting system is very sparse and can be solved fast. As illustration, for a rather small system, i.e. small number of elements, a direct method such as the LU-decomposition can be used. The time to solve the elliptic system takes 10% to 20% of the total computing time. For larger systems, or for 2D variants of the code, an iterative method such as preconditioned conjugate gradient has been applied to solve the elliptic system. This step then cost 20% to 40% of the total computing time. In all cases, a good initial guess of Ψ is available from the previous time steps.

For dealing with an influx (signalling) problem, the algorithm above can still be applied. For simulations of OVBM which are performed in the next section, we use the internal wave generation that similar with a method of Wei et al. [1999] and Kim et al. [2007]. Here, the influx signal at position x_0 is added as a source function in the dynamic equations, but weighted with $\breve{V}(x-x_0)$, where

$$\breve{V}(x) = \int V(k)e^{-ikx}dk$$

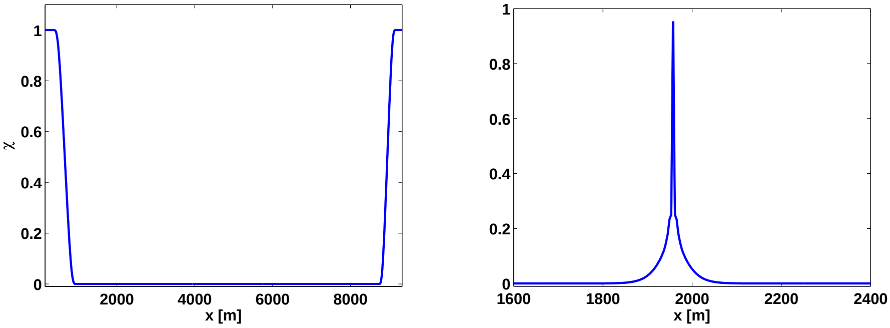

Figure 3.2: *At the left, the characteristic function* χ *is shown. At the right, the embedded force function* $\breve{V}(x - x_0)$ *of the OVBM with two vertical profiles is shown.*

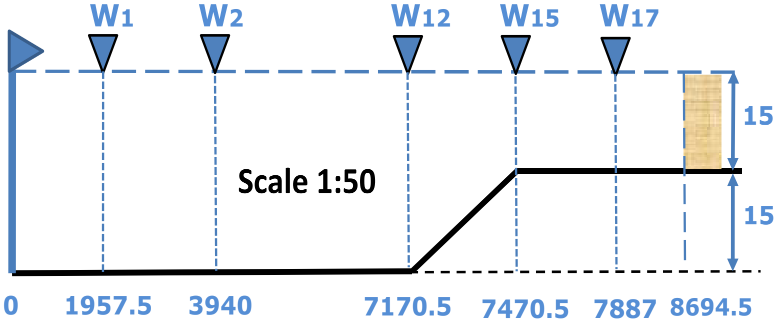

Figure 3.3: *The situation of the experiment scalled-up* $(1:50)$ *to coastal dimensions (units in meter). The waves are generated by a wave flap in the laboratory and measured at several positions;* W_1*,* W_2*,* W_{12}*,* W_{15}*, and* W_{17}*. Note that the horizontal distances between these positions are not in scale.*

is the inverse Fourier transform of the group velocity $V(k)$ of the model. The resulting dynamic equations (3.8) including this source function become

$$\begin{cases} \partial_t \eta &= -\partial_x((h+\eta)\partial_x\phi) - \partial_x(\beta \cdot \partial_x \Psi) + 2\breve{V}(x-x_0)s(t) \\ \partial_t \phi &= -g\eta - \frac{1}{2}\partial_x \phi^2 \end{cases}$$

where $s(t)$ is the influx signal.

Instead of using transparent/radiation boundary conditions to limit the domain of computation, we use a damping-zone to damp the waves outside the computational window. We defined a smoothened characteristic function χ near both ends of the interval, and vanishing in the area of the domain of interest, leading to

$$\begin{cases} \partial_t \eta &= -\partial_x((h+\eta)\partial_x\phi) - \partial_x(\beta \cdot \partial_x \Psi) + 2\breve{V}(x-x_0)s(t) - a\chi\eta \\ \partial_t \phi &= -g\eta - \frac{1}{2}\partial_x \phi^2 - a\chi\phi \end{cases}$$

An illustration of this characteristic function $\chi(x)$ and the function $\check{V}(x)$ are shown in Figure 3.2 for the applications in this paper. The choice of the damping coefficient a and the length of the damping zone are coupled. The exponential decay e^{-at} is sufficient for $a = 1$ when the length of damping zone such that the traveling time of the (longest) wave is long enough to obtain an attenuation factor of 10^{-6}.

3.4 Numerical simulations

3.4.1 Laboratory experiments

In this paper we consider two cases for which experimental data from the hydrodynamic laboratory MARIN (the Maritime Research Institute Netherlands) are available to test the performance of the OVBM. The first case is a bichromatic wave, MARIN test number 305002, and the other case is an irregular wave, MARIN test number 103001. The experiments were performed in a wave tank of $180m$ length and $0.6m$ water depth. At a certain location of the tank there is a 1/20 slope from $0.6m$ to $0.3m$ water depth. This geometry in laboratory dimension was designed to represent a realistic situation in the coastal area which has a scale of 1 : 50. The coastal dimensions related to laboratory scale are shown in Figure 3.3. A wave absorber in the laboratory as artificial beach is placed at the end (at the right) of the wave tank. For the simulations we use the scaled situation as in Figure 3.3 for both cases.

For numerical simulations, we use the signal that was measured at $W_1 = 1957.5m$ as influx signal. At this position, the signal contains bound waves that are generated during the propagation from the wave flap to W_1. Therefore, we filtered the signal by neglecting contributions of long and short waves in the spectrum at W_1. For both cases, we compare the signals of the simulations of the OVBM with the measurements at positions indicated in Figure 3.3; $W_2 = 3940m$, $W_{12} = 7170.5m$ (at the foot of the slope), $W_{15} = 7470.5m$ (at the top of the slope), and $W_{17} = 7887m$ (at the shallow area).

3.4.2 Simulation of bichromatic waves

The experiment of the bichromatic waves was executed for a time interval that corresponds after scaling to $6000s$. In this paper, we show results of a simulation for one hour since the rest of the simulation showed the same behaviour. The measured signal at W_1 and its amplitude spectrum as a function of frequency [Hz] are shown in Figure 3.4. The peak frequency of this case is $0.076Hz$ ($\omega_{peak} = 0.4814$); this corresponds to waves of wavelength $197.3m$ in the deep area ($h = 30m$) and $148.9m$ in the shallow area ($h = 15m$). From the spectrum of the influx signal shown in Figure 3.4 we see that second order waves have frequency $0.165Hz$. Taking 8 points to represent the shortest waves, we choose $dx = 4m$ for the simulation. This is accurate enough to represent all the waves (including second order waves) for which the dispersion error is less than 10^{-3} (see Figure 3.5). The maximal wave steepness reached during the experiment of this case is 0.001 in the shallow area ($h = 15m$).

The bichromatic case has a narrow spectrum as shown in Figure 3.4. Here and in the following, in 'spectrum plots' we show vertically the square root of the power spectrum

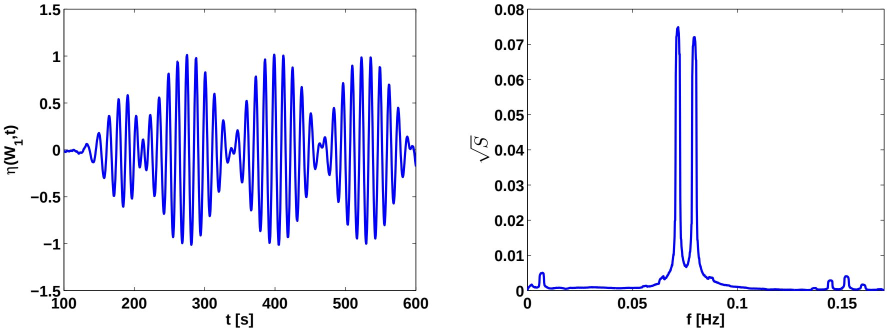

Figure 3.4: *At the left is shown the measured signal at W_1 of the bichromatic waves for a short time interval (of the total 1 hour), and at the right the amplitude spectrum (square root of the spectrum defined in (3.16), i.e. the absolute value of the complex spectrum of the signal) as a function of frequency [Hz].*

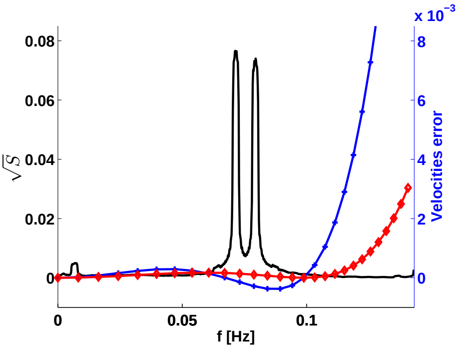

Figure 3.5: *The amplitude spectrum (solid line, left hand axis) is plotted together with velocity errors: the group velocity error (solid line with plus sign, right hand axis) and the phase velocity error (solid line with diamond, right hand axis) as function of frequency [Hz] for the one vertical profile OVBM with calculated optimal value* $\nu = 0.612$ *(corresponding to* $0.0974Hz$*) above the depth at* W_1 *(*$h = 30m$*).*

defined in (3.16), i.e. the absolute value of the complex spectrum of the signal; this representation shows more clearly than a plot of the power spectrum the long and short wave contributions. it turns out that for this reason sufficiently good simulation results are found by using only one vertical profile. This can also be seen from the plot in Figure 3.5 of the group velocity error $V_{vbm} - V_{ex}$ and the phase velocity error $C_{vbm} - C_{ex}$.

Here, we use a notation $\nu = \Omega_{vbm}(\kappa)$ for the optimal frequency that corresponds to the optimal wavenumber κ for the Airy profile (3.9). The optimal value ν is obtained by minimizing the kinetic energy error (3.17). The plot of the kinetic energy error as a function of ν is shown in the left plot of Figure 3.6 at the deep part of the water; the position of the lowest value produces the optimal value ν. The optimal values above the other depths are shown at the right.

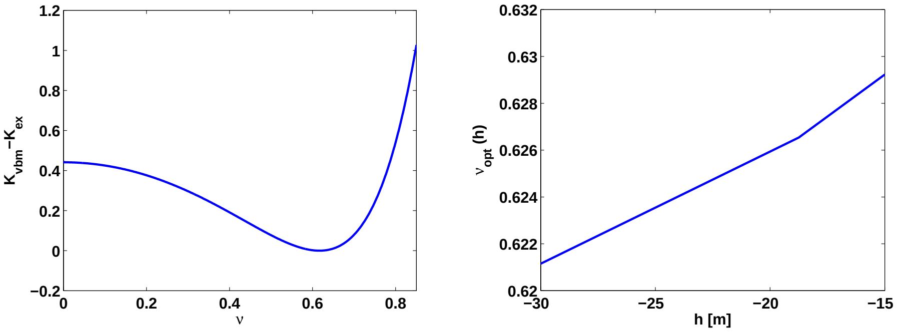

Figure 3.6: *At the left a plot of the kinetic energy error ($K_{vbm} - K_{ex}$) as function of ν for $h = 30m$, and at the right the optimal values ν for each depth above the slope.*

Part of the signals of the simulation at positions W_2, W_{12}, W_{15}, and W_{17} are compared with the measurements in Figure 3.7. The phasing and form of the simulated and measured waves agree quite well. Amplitude spectrum of the simulation and measurement are compared at positions W_{12} and W_{17} in Figure 3.8; comparing the long and short wave components in the spectrum, the simulation of nonlinear effects seems to be quite accurate. In subsection 4.4 we provide additional quantitative information about the quality of the simulated waves.

3.4.3 Simulation of Irregular waves

The experiment and the simulation of the irregular waves were executed for a time interval that corresponds after scaling to $12500s$ (approximately 3.5 hours). The measured signal at W_1 and its amplitude spectrum as function of frequency [Hz] is shown in Figure 3.9. The irregular waves are generated by using JONSWAP-type of spectrum with random phases. Here, the generated spectra has significant waveheight $3.12m$ in the coastal dimension. The peak frequency of this case is $0.0831Hz$ ($\omega_{peak} = 0.522$); this corresponds to waves of wavelength $177.6m$ in the deep area ($h = 30m$) and $135.7m$ in the shallow area ($h = 15m$). From the amplitude spectrum, we observed that the shortest waves have frequency $0.318Hz$, corresponding to waves with wavelength $15.4m$. Based on this reasoning, and taking 8 points to represent the shortest waves, we choose $dx = 2m$ for the simulation. The maximal wave steepness reached during the experiment and simulation of this case is 0.037. The steepest waves appear near $x = 5000m$ (in coastal dimension) as shown in Figure 3.14.

Different from the previous test case, the irregular waves has a broad spectrum as shown in Figure 3.9; it turns out that for this reason the simulation with one vertical profile will not be sufficient. This can already be anticipated from the plots in Figure 3.10 of the velocity errors of the one vertical profile OVBM (in the left plot) and the two vertical profiles OVBM (in the right plot). Using one vertical profile, the velocity errors are quite large for the main frequencies of the waves, while with two vertical profiles the errors are 10 times less. Therefore, we used two vertical profiles OVBM to get good results for the simulation of these irregular waves, but we will also present some

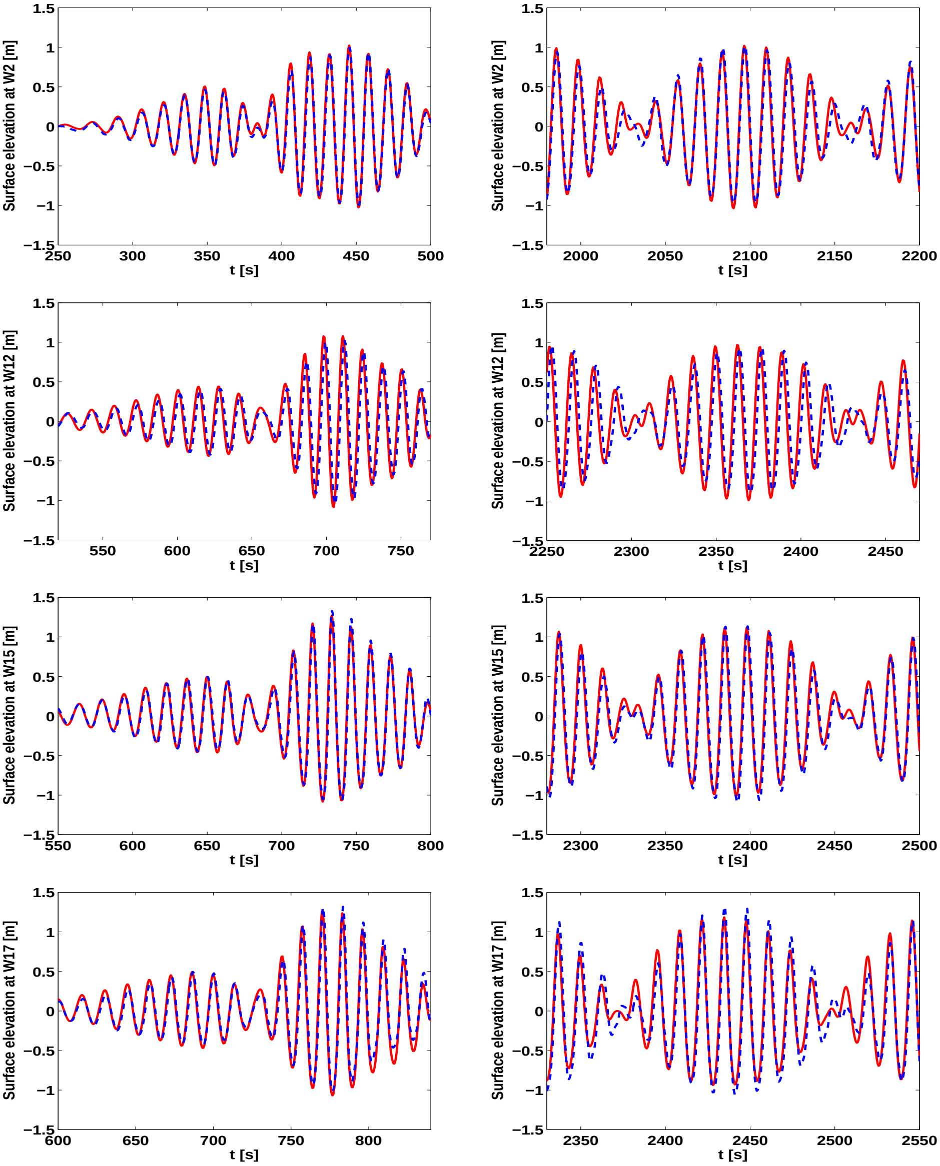

Figure 3.7: *The simulated (solid line) and measured (dashed line) signals of the bichromatic waves are compared at positions* W_2 *(first row),* W_{12} *(second row),* W_{15} *(third row), and* W_{17} *(fourth row). In the shallow area,* W_{15} *and* W_{17}*, nonlinear effects can be observed in the simulations and measurements.*

quantitative information about the results of simulations with one vertical profile.

The optimal frequencies ν_m, leading to corresponding optimal wavenumbers κ_m for

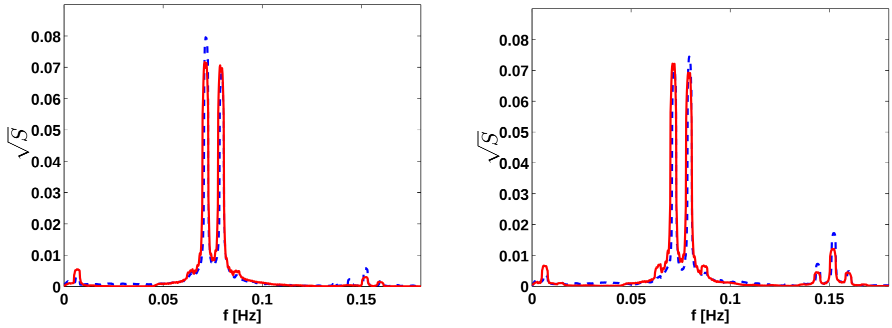

Figure 3.8: *Plot of the amplitude spectrum of the simulations (solid line) and the measurements (dash line) at W_2 (left) and W_{17} (right) as function of frequency [Hz]. The short and long wave components become larger in the shallow area.*

the Airy profiles (3.9) are obtained by minimizing the kinetic energy error (3.17). The plot of the kinetic energy error for the two vertical profiles as a function of ν_1 and ν_2 is shown in the left plot of Figure 3.11 at the deep part of the water; the lowest value produces the optimal values ν_1 and ν_2. For other depths the optimal values are shown at the right.

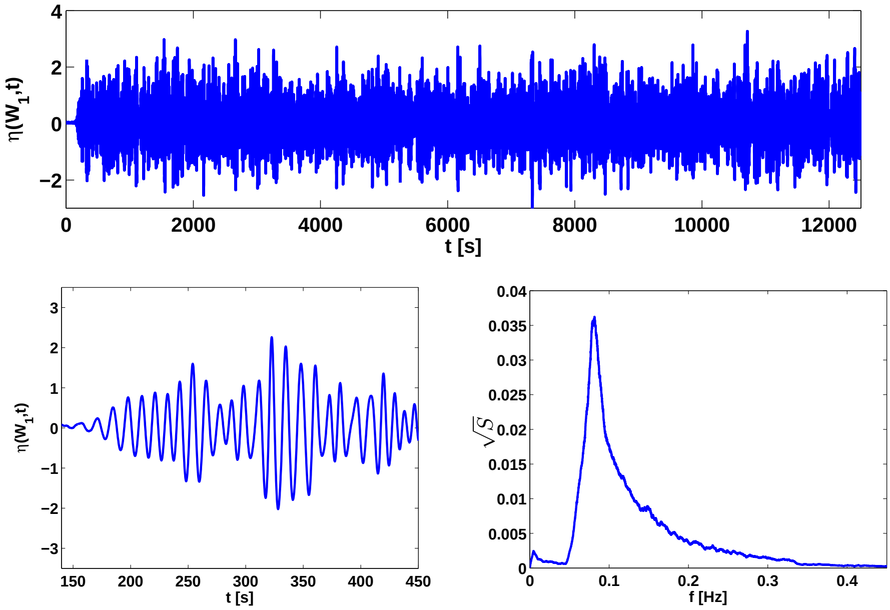

Figure 3.9: *At the top and lower left are shown the measured time signals at W_1 of the irregular waves, and at the lower right the amplitude spectrum (of the total time signal) as a function of frequency [Hz].*

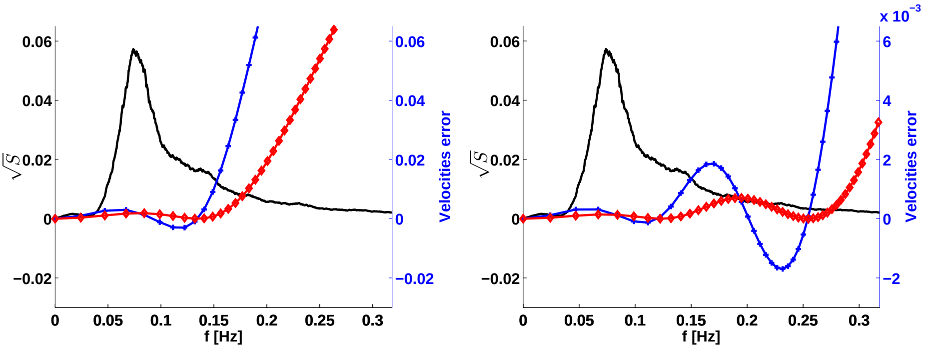

Figure 3.10: *The amplitude spectrum (solid line, left hand axis) of the irregular waves is plotted together with the group velocity error (solid line with plus sign, right hand axis) and the phase velocity error (solid line with diamond, right hand axis) as functions of frequency [Hz] above the depth* $h = 30m$*. At the left for the OVBM case with one vertical with calculated optimal value* $\nu = 0.84$ *(corresponds to* $0.133Hz$*), at the right for two vertical profiles with calculated optimal values* $\nu_1 = 0.77$ *and* $\nu_2 = 1.59$ *(corresponds to* $0.122Hz$ *and* $0.253Hz$*).*

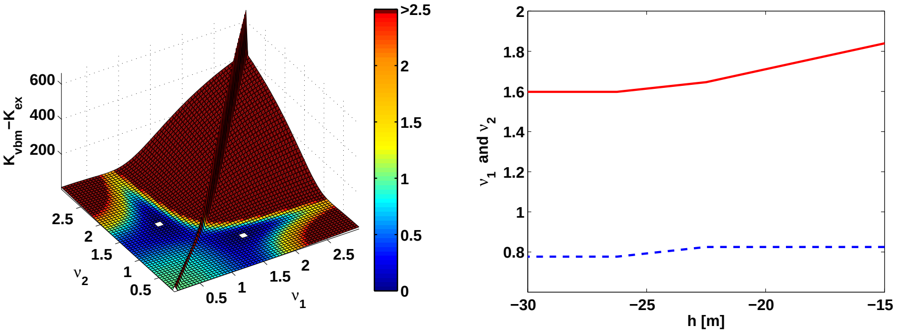

Figure 3.11: *At the left the plot of the kinetic energy error* $(K_{vbm} - K_{ex})$ *as function of* ν_1 *and* ν_2 *for* $h = 30m$*, and at the right the optimal* ν_1 *(dashed line) and* ν_2 *(solid line) for each depth above the slope.*

As in the previous case, the signals of the simulation at positions W_2, W_{12}, W_{15}, and W_{17} are compared with the measurements in Figure 3.12 and 3.13. The phasing and form of the simulated and measured waves agree quite well even after $10000s$ of simulation. Spectra of the simulation and measurement are compared at each position, shown at the right part of Figure 3.13. Comparing the long and short wave components in the spectrum, the simulation of nonlinear effects seems to be quite accurate.

In Figure 3.14 we show the curves of maximal and minimal temporal amplitude (MTA) (after $3.5hr$ of simulation) which are the highest and lowest points in the full time trace at each position. In the same figure, we also show a snapshot of the spatial wave profile at $t = 1999s$. As can be seen, at this time near position $x = 5106m$ appears a very high wave.

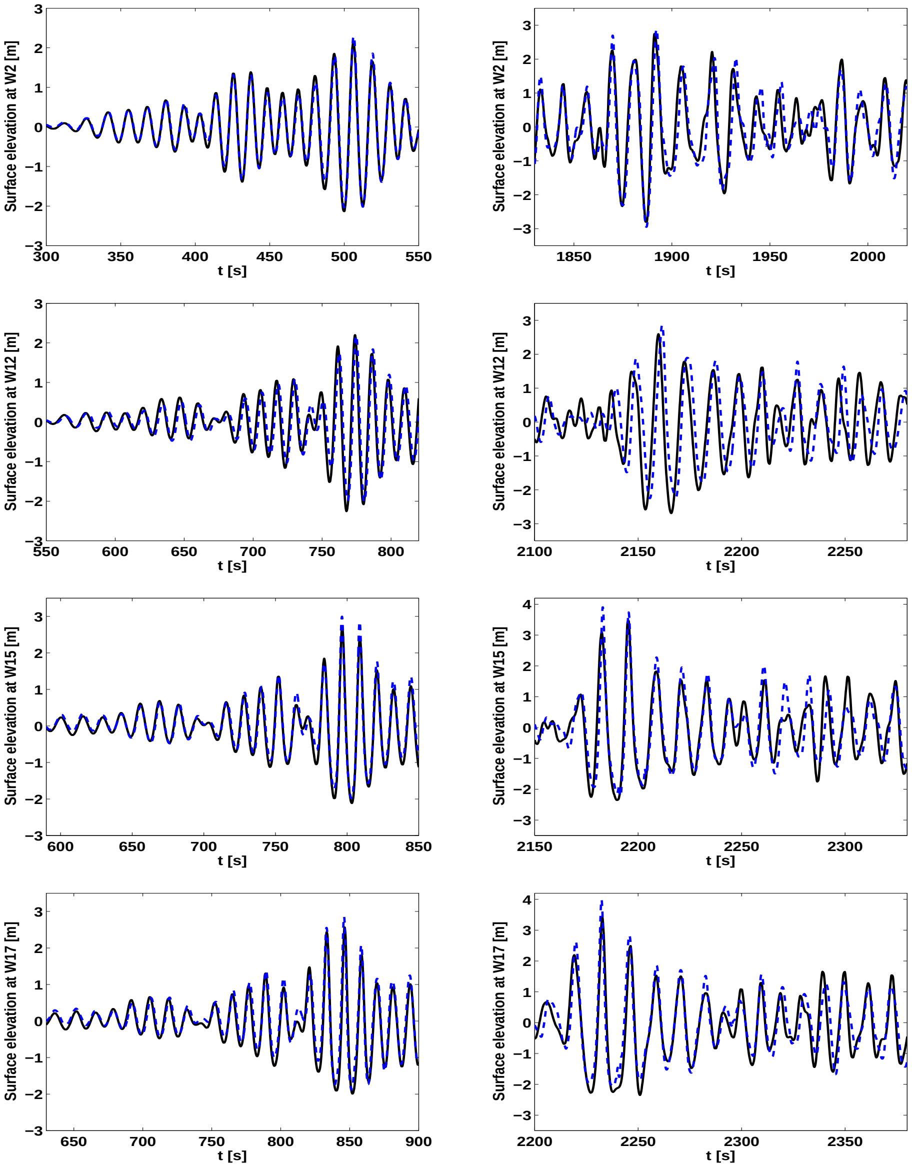

Figure 3.12: *The simulated (solid line) and measured (dashed line) signals of irregular waves compared at positions W_2 (first row), W_{12} (second row), W_{15} (third row), and W_{17} (fourth row).*

3.4.4 Correlation and variance-quotient

Besides comparing the plots of the signals and their amplitude spectra, we will now quantify the relation between the simulation and measurement by calculating the correlation

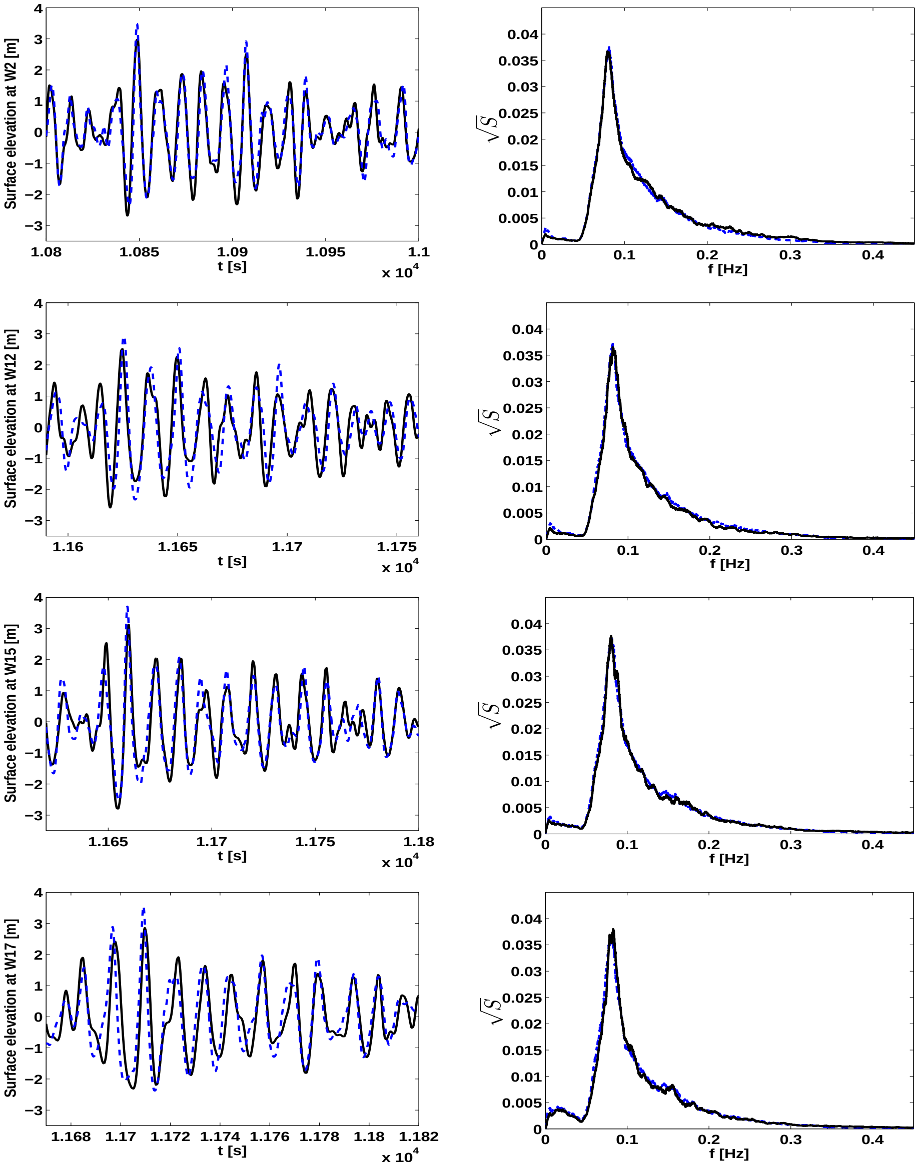

Figure 3.13: *The simulated (solid line) and measured (dashed line) signals of irregular waves at the left, and the comparison of the amplitude spectrum at the right at positions* W_2 *(first row),* W_{12} *(second row),* W_{15} *(third row), and* W_{17} *(fourth row) after* $10000s$ *of simulation.*

and variance-quotient; these are defined by

$$corr(S_1, S_2) = \frac{< S_1\left(t\right), S_2\left(t\right) >}{\left|S_1\left(t\right)\right| \left|S_2\left(t\right)\right|} \tag{3.23}$$

$$VQ(S_1, S_2) = \frac{\left|S_1(t)\right|^2}{\left|S_2(t)\right|^2} \tag{3.24}$$

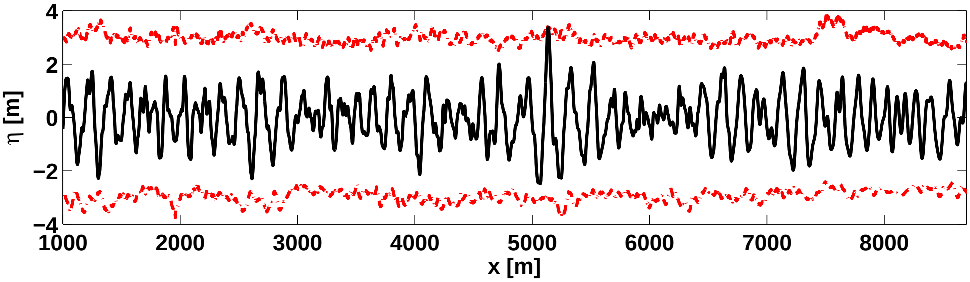

Figure 3.14: *MTA curves of maximal (upper curve) and minimal (lower curve) temporal amplitude (denoted by dot dashed line) after* $3.5hr$ *of simulation and a snapshot of the propagating wave (denoted by solid line) at* $t = 1999s$ *for the irregular waves.*

Position	BC (1-profile)		Irr (1-profile)		Irr (2-profiles)		Irr (ABvar)	
	corr	VQ	*corr*	VQ	*corr*	VQ	*corr*	VQ
W_2	0.98	0.99	0.86	1.02	0.90	1.02	0.96	1.05
W_{12}	0.84	1.04	0.29	1.05	0.62	1.04	0.72	1.13
W_{15}	0.96	0.94	0.66	1.00	0.86	0.99	0.93	1.00
W_{17}	0.95	0.91	0.64	1.03	0.85	1.02	0.92	1.03

Table 3.1: *Comparison of correlation (corr) and variance-quotient (VQ) for the bichromatic (BC) and the irregular (Irr) wave for one and two vertical profiles OVBM and the ABvar model.*

respectively, where $S_1(t)$ and $S_2(t)$ are the signals to be compared, $< \cdot, \cdot >$ represents the L^2-inner product, and $|\cdot|$ the L^2-norm. Note that $corr\,(S_1, S_2)$ is a number between -1 and 1, and has value one only when one signal is proportional to the other one; hence, this quantity will in particular given an indication of the phase-errors between the two signals. Note that we do *not* apply any time shift to improve the correlation. The variance-quotient gives an indication about the amplitude-errors between the two signals.

In Table 3.1 we present the values as calculated at the measurement positions for $1hr$ of simulations. We observe that for the bichromatic wave the simulation with one vertical profile gives very good correlation and variance-quotient values. For the irregular wave, the model with two vertical profiles gives much better correlation values compared to the one vertical profile model.

In Table 3.1, we also show the correlation and variance-quotient of simulation of irregular wave by another code which is based on the AB-equation of van Groesen and Andonowati [2007]. The ABvar-equation is a uni-directional model for uneven bottom with exact dispersion in first and second order, see van Groesen and van der Kroon [2012] for more details of that simulations.

Note that at position W_{12} both cases and models give lower correlation compared to the other positions. This is difficult to explain, since a gradual decrease of correlation in downstream direction would be expected, while at the shallow area W_{15} and W_{17} the correlation values are higher.

3.5 Conclusion and remarks

The numerical implementation of the OVB-model is remarkably simple because the highest spatial derivatives are of second order and there are no mixed spatial-temporal derivatives.

The simulations in the last section have shown that the use of multiple vertical profile functions and the optimization procedure, can greatly enhance the quality of the simulations. The number of profiles needed to get accurate results depends on the broadness of the spectrum, and should be determined a priori. As shown, for the narrow band bichromatic waves one profile was sufficient, for the broader $12s$ irregular waves we used two profiles; to simulate shorter $9s$ period irregular waves (not reported here), we needed 3 profiles.

The flexibility to choose the number of vertical profile functions and the possibility to optimize the vertical profile functions means that our model is case-dependent. This may seem impractical, but allows us to obtain depending on the input signal (or initial elevation) the best possible dispersion properties over the regime wavenumber interval. Hence, there is no fixed limit for relative depth kh as is the case for other Boussinesq models with dispersion that is derived from a rational asymptotic perturbation scheme.

Figure 3.11 shows that above varying bottom the optimized values of the parameters change substantially; as has been remarked, the use of the initial spectrum in the kinetic energy functional (3.15) is only approximate since, in fact, the spectrum will change with depth. This is still a topic of possible improvement.

The comparison in section 3.4 of the simulations with real-live measurements deserves some comments. Since a series of field data are difficult to obtain (and will contain 2HD pertubations), the scaled accurate measurements of MARIN have been used. Differences between the simulations and the measurements will be partly due to the imperfection of the simulation model. But a part can also be caused by reflections that have not been modeled, in particular reflections from the artificial beach and the end wall of the laboratory wave tank. These reflections, and just as well as the reflections from the slope, are included in the measured elevation at the point of influxing and will therefore perturb the influx signal. Such pertubations will contribute to the decreasing correlation downstream over a length of approximately 40 wave lengths.

The numerical code, programmed in MATLAB, is quite efficient; the computation time for the simulation of the bichromatic case with one vertical profile took 38% of the experiment time, while for the irregular waves with two vertical profiles it took 117% of the experiment time, for calculations done with a PC with 3GHz Intel dual core processor and 4GB of RAM.

The results of the second test case, the irregular waves, have been presented in a ”Benchmark workshop on numerical wave modelling” on November 25, 2010, held at MARIN. In the benchmark the challenge for widely invited participants was to show their simulation at the downstream positions W_2 and further, using the provided experimental data of the wave maker motion and the elevation measurement at W_1. Besides results of the OVBM code presented here, only results of the ABvar-code van Groesen and van der Kroon [2012] were presented.

The extension of the model to 2D has been developed in Klopman et al. [2007] for the spectral-implementation and in Adytia and van Groesen [2011] for the Finite Element-implementation. In these papers, the 2D VBM is tested to simulate the experiment of Berkhoff et al. [1982]. This experiment illustrates the accuracy of wave refraction, diffraction and shoaling over a complex bathymetry. The comparison between the model and measurements shows a good agreement. Moreover, the codes show a robustness for dealing with such a complex bathymetry.

Appendix 3.A

Using the notation $\xi = h + \eta$, the explicit expression for the coefficients α, γ, and β in (3.7) are given for $i = j$ by

$$\begin{aligned}
\alpha_{ii}(\kappa_i) &= -\frac{3}{2\kappa_i}\tanh(\kappa_i\xi) + \frac{\kappa_i\xi}{2\kappa_i\cosh^2(\kappa_i\xi)} + \xi \\
\gamma_{ii}(\kappa_i) &= \frac{\kappa_i\tanh(\kappa_i\xi)}{2} - \frac{\kappa_i^2\xi}{2\cosh^2(\kappa_i\xi)} \\
\beta_i(\kappa_i) &= \frac{\tanh(\kappa_i\xi)}{\kappa_i} - \xi
\end{aligned}$$

and for $i \neq j$ by

$$\begin{aligned}
\alpha_{ij}\left(\kappa_i,\kappa_j\right) = \{&\frac{\sinh\left(\left(\kappa_i+\kappa_j\right)\xi\right)}{\left(\kappa_i+\kappa_j\right)} + \frac{\sinh\left(\left(\kappa_i-\kappa_j\right)\xi\right)}{\left(\kappa_i-\kappa_j\right)} \\
&- \left(1/\kappa_i + 1/\kappa_j\right)\sinh\left(\left(\kappa_i+\kappa_j\right)\xi\right) \\
&+ \left(1/\kappa_i - 1/\kappa_j\right)\sinh\left(\left(\kappa_j-\kappa_i\right)\xi\right) + \xi[\cosh\left(\left(\kappa_i+\kappa_j\right)\xi\right) \\
&+ \cosh\left(\left(\kappa_i-\kappa_j\right)\xi\right)]\}/2\cosh\left(\kappa_i\xi\right)\cosh\left(\kappa_j\xi\right)
\end{aligned}$$

$$\gamma_{ij}\left(\kappa_i,\kappa_j\right) = \frac{\kappa_i\kappa_j}{2\cosh\left(\kappa_i\xi\right)\cosh\left(\kappa_2\xi\right)}\left[\frac{\sinh\left(\left(\kappa_i+\kappa_j\right)\xi\right)}{\left(\kappa_i+\kappa_j\right)} - \frac{\sinh\left(\left(\kappa_i-\kappa_j\right)\xi\right)}{\left(\kappa_i-\kappa_j\right)}\right]$$

Chapter 4

The Variational 2D Boussinesq model for wave propagation over a shoal[1]

Summary

The Variational Boussinesq Model (VBM) for waves (see e.g. Klopman et al. [2010]) is based on the Hamiltonian structure of gravity surface waves. In its approximation, the fluid potential in the kinetic energy is approximated by the sum of its value at the free surface and a linear combination of vertical profiles with horizontal spatially dependent functions as coefficients. The vertical profiles are chosen a priori and determine completely the dispersive property of the model. For coastal applications, the 1D version of the model has been implemented in a Finite Element(FE)-code with piecewise linear basis functions. Results of simulations have been been compared with experiments from MARIN hydrodynamic laboratory for a focusing wave group running above a flat bottom (Lakhturov, Adytia, and van Groesen [2012]) and for irregular waves running above a sloping bottom (this thesis, Chapter 3). The 2D version of the model has been derived and implemented using a pseudo-spectral method with a rectangular grid in Klopman et al. [2007, 2010]. A limitation of the later implementation is a lack of flexibility when the model deals with a complicated domain such as a harbour. Here, we will present an implementation of the model in a 2D FE-code which is consistent with the derivation of the model via the variational formulation. To illustrate the accuracy of wave refraction and diffraction over a complex bathymetry, the experiment of Berkhoff et al. [1982] is used to compare the FE results with measurements.

---

[1] This chapter is a slight extension of the published paper : D. Adytia and E. Van Groesen, The variational 2D Boussinesq model for wave propagation over a shoal, International Conference on Developments in Marine CFD, November 2011, Chennai, India. RINA. ISBN No. 978-1-905040-92-6, p.25-29.

4.1 Introduction

For coastal zone applications such as simulations of coastal waves in a harbour, besides the mild-slope equations, Boussinesq-type of equations have been favorite because of the ability to represent the physical phenomena of water waves such as non-linearity, dispersion and bathymetric effects. The standard Boussinesq equations which include the effect of bathymetry were first derived by Peregrine [1967], who used depth averaged velocity as dependent variable. But this model is restricted to shallow water because of its rather poor dispersion characteristics in intermediate and deep water. Since then, there have been many works to improve the dispersion quality of Boussinesq-type equations, e.g. Madsen and Sørensen [1992] and Nwogu [1993].

In order to achieve good dispersive characteristics, many of these Boussinesq-type equations include high order spatial (or mixed with time) derivatives; this makes them rather difficult for numerical implementations and for practical applications. In this Chapter, we will use a Boussinesq-type of equation that is derived from a variational formulation. This will lead to a system of equations with a much simpler numerical implementation since it only contains second order spatial derivatives without mixed time-space derivatives. In Section 4.2, we derive the 2D version of this model. Section 4.2.2 describes the Finite Element implementation of the model and in Section 4.3 the performance of this implementation is tested for the experiment of Berkhoff et al. [1982]. Section 4.4 provides conclusions of this Chapter.

4.2 Variational Boussinesq Model

4.2.1 Variational formulation for VBM

The variational principle for water waves was introduced by Luke in Luke [1967]. Related to the Hamiltonian equations in Zakharov [1968], Broer [1974], Miles [1977], the Lagrangian $\mathcal{L}$ in Luke's variational principle, which depend on fluid potential in the interior $\Phi(\mathbf{x}, z, t)$ and surface elevation $\eta(\mathbf{x}, t)$, can be reformulated in canonical variables at the free surface. These are the surface elevation η and the fluid potential at the free surface $\phi(x, t)$ as

$$\mathcal{L} = \int \left[\int \phi \partial_t \eta d\mathbf{x} - \mathcal{H}(\eta, \phi) \right] dt \tag{4.1}$$

Here $\mathcal{H}$ is the Hamiltonian or the total energy, which is the sum of the kinetic energy and the potential energy that are defined as

$$K = \frac{1}{2} \int_x \int_{-h}^{\eta} |\nabla_3 \Phi|^2 \, dz d\mathbf{x} \qquad \text{and } P = \frac{1}{2} \int_x g \eta^2 d\mathbf{x}$$

respectively, and $h(\mathbf{x})$ describes the bottom. By taking variations with respect to η and ϕ, the Hamiltonian equations are found

$$\partial_t \eta = \delta_\phi \mathcal{H} \qquad \text{and } \partial_t \phi = -\delta_\eta \mathcal{H}$$

where $\delta_\phi \mathcal{H}$ and $\delta_\eta \mathcal{H}$ denote the variational derivatives of $\mathcal{H}$ with respect to η and ϕ. The exact formulation will be obtained if we could assure that the potential velocity

Φ satisfies the Laplace equation in the interior, the impermeability condition at the bottom and the condition $\Phi = \phi$ at the free surface. The main difficulty in water wave modeling arises from the need to approximate the kinetic energy explicitly in the surface variables. Nevertheless, after finding an approximation for the kinetic energy, following the variational steps above, we obtain a consistent approximation that keeps the consequences of the Hamiltonian form, such as energy conservation.

As described in Klopman et al. [2005, 2007, 2010], Lakhturov et al. [2012] and Adytia and van Groesen [2012], the VBM is obtained by approximating the vertical structure of the fluid velocity Φ in the expression of K with its value at the surface ϕ and multiple expansion terms as

$$\Phi\left(\mathbf{x}, z, t\right) = \phi\left(\mathbf{x}, t\right) + \Sigma_m F_m\left(z\right)\psi\left(\mathbf{x}, t\right) = \phi + F \cdot \Psi$$

where F and Ψ are vector functions. In order to keep the canonical structure of the Hamiltonian, the condition $\Phi = \phi$ at the free surface has to be assured. As consequence, it is required that $F_m\left(z = \eta\right) = 0$. The vertical profile function $F_m\left(z\right)$ has to be chosen in advance, while $\psi_m\left(x\right)$ are functions that have to satisfy an optimality condition of vanishing of the kinetic energy with respect to variations in ψ_m. Such variations lead to a system of linear elliptic equations that has to be solved together with the dynamics for the variables η and ϕ. By substituting the approximation of Φ into K, we obtain the kinetic energy of VBM

$$\begin{aligned}
K_B &= \frac{1}{2}\int_{\mathbf{x}}\int_{-h}^{\eta}\left|\nabla\phi + \nabla\left(F\cdot\Psi\right)\right|^2 + \left(\partial_z F\cdot\Psi\right)^2 dz d\mathbf{x} \\
&\approx \frac{1}{2}\int_{\mathbf{x}}\int_{-h}^{\eta}\left|\nabla\phi + F\cdot\nabla\Psi\right|^2 + \left(\partial_z F\cdot\Psi\right)^2 dz d\mathbf{x} \\
&= \frac{1}{2}\int_{\mathbf{x}}\left[\left(h+\eta\right)\left|\nabla\phi\right|^2 + 2\nabla\phi\beta\cdot\nabla\Psi + \nabla\Psi\cdot\alpha\nabla\Psi + \Psi\cdot\gamma\Psi\right] d\mathbf{x}
\end{aligned}$$

In the second line, we use a *weakly-nonlinear* approximation (see Klopman et al. [2005] for details) where F is assumed to be slowly varying with respect to η and h. In the last expression, matrices α and γ, and a vector β are introduced with elements given by

$$\alpha_{ij} = \int_{-h}^{\eta} F_i F_j dz; \quad \gamma_{ij} = \int_{-h}^{\eta} \partial_z F_i \partial_z F_i dz; \quad \beta_i = \int_{-h}^{\eta} F_i dz$$

By substituting the expression of the kinetic energy above into the Lagrangian (1), we obtain

$$\mathcal{L} = \int\left[\int \phi\partial_t\eta d\mathbf{x} - \mathcal{H}_b\left(\eta, \phi, \psi_m\right)\right] dt \tag{4.2}$$

where $\mathcal{H}_b$ is the Hamiltonian for the VBM. Taking variations with respect to η, ϕ and ψ_m, we obtain a system of PDE

$$\begin{aligned}
\partial_t\eta &= -\nabla\cdot\left[\left(h+\eta\right)\nabla\phi\right] - \nabla\cdot\left[\beta\cdot\nabla\Psi\right] \\
\partial_t\phi &= -g\eta - \left|\nabla\phi\right|^2/2 \\
-\nabla\cdot\left[\alpha\nabla\Psi\right] + \gamma\Psi &= \nabla\cdot\left[\beta\nabla\phi\right]
\end{aligned} \tag{4.3}$$

The dispersive quality of the system above is highly determined by the choice of the vertical profile functions $F_m(z)$. In Klopman et al. [2010], it was suggested to choose a parabolic profile for rather long waves, or a cosine hyperbolic profile that is obtained from Airy's linear potential theory :

$$F(z;\eta,h) = \cosh(\kappa(z+h))\,/\cosh(\kappa(\eta+h)) - 1; \tag{4.4}$$

F has exact phase and group velocity (only) for the wave with wavenumber κ. For periodic waves, the latter profile is the best choice, since we can choose κ as the wavenumber of the waves to be simulated. For broad spectra such as for focusing wave groups and irregular (coastal) waves, the optimal choice of κ for the Airy profiles above can be obtained by minimizing the kinetic energy functional for a given initial influx signal as described in Lakhturov et al. [2012] and Adytia and van Groesen [2012].

4.2.2 Finite Element Implementation

The VBM is obtained from a variational formulation by minimizing the Lagrangian of VBM (4.2) with respect to η, ϕ and ψ_m. For this reason, it is quite natural to implement the VBM by using the Finite Element Method (FEM). Besides this, we can use piecewise linear local basis functions since the highest derivatives in (4.2) are of first order. In this implementation we discretize the solutions in space by using FEM which leads to a system of ordinary differential equations (ODEs) that is solved using an explicit time integrator such as a Runge-Kutta method.

We start the spatial discretization of the solutions η, ϕ and ψ_m into $\overline{\eta}$,$\overline{\phi}$ and $\overline{\Psi}$ by using standard 2D triangular basis functions $T(\mathbf{x})$, then substitute them into the Lagrangian of VBM (4.2). This leads to a Lagrangian with vector state variables

$$\overline{\mathcal{L}} = \int \left[M\overline{\phi}\cdot\partial_t\overline{\eta} - \overline{\mathcal{H}}_b\left(\overline{\eta},\overline{\phi},\overline{\psi}_m\right)\right] dt \tag{4.5}$$

with

$$\overline{\mathcal{H}}_b = \frac{1}{2}g\mathbf{M}\overline{\eta}\cdot\overline{\eta} + \frac{1}{2}\mathbf{D}\overline{\phi}\cdot\overline{\phi} + \overline{H}_3\left(\overline{\eta},\overline{\phi}\right) + \mathbf{B}\cdot\overline{\Psi} + \frac{1}{2}\mathbf{A}\overline{\Psi}\cdot\overline{\Psi} + \frac{1}{2}\mathbf{G}\overline{\Psi}\cdot\overline{\Psi}$$

Here $\mathbf{M}$ is the so-called *mass matrix* with elements $\mathbf{M}_{i,j} = \int T_i(\mathbf{x})\,T_j(\mathbf{x})\,d\mathbf{x}$, $\mathbf{D}$ and $\mathbf{A}$ are so-called *stiffness matrices* with elements

$$\mathbf{D}_{i,j} = \int h(\mathbf{x})\,\nabla T_i(\mathbf{x})\cdot\nabla T_j(\mathbf{x})\,d\mathbf{x} \quad\text{and}\quad \mathbf{A}_{i,j} = \int \alpha(\mathbf{x})\,\nabla T_i(\mathbf{x})\cdot\nabla T_i(\mathbf{x})\,d\mathbf{x}$$

respectively. $\mathbf{G}$ is the matrix with elements $\mathbf{G}_{i,j} = \int \gamma(\mathbf{x})\,T_i(\mathbf{x})\,T_j(\mathbf{x})\,d\mathbf{x}$, $\mathbf{B}$ is the column vector $\mathbf{B} = \left[B(\beta_1)\,\overline{\phi},\cdots,B(\beta_{N1})\,\overline{\phi}\right]$ with $B(\beta_i) = \int \beta_i(\mathbf{x})\,\nabla T(\mathbf{x})\cdot\nabla T(\mathbf{x})\,d\mathbf{x}$, and $\overline{H}_3\left(\overline{\eta},\overline{\phi}\right)$ is the nonlinear cubic term :

$$\overline{H}_3(\eta,\phi) = \frac{1}{2}\Sigma_{i,j,k}\eta_i\phi_j\phi_k C_{ijk}$$

with $C_{ijk} = \int T_i\nabla T_j(\mathbf{x})\cdot\nabla T_k(\mathbf{x})\,d\mathbf{x}$. Now, from the Lagrangian (4.5), we obtain the Hamiltonian equations as the following matrix system

$$\begin{aligned}
\mathbf{M}\partial_t\overline{\eta} &= \partial_{\overline{\phi}}\overline{H}_b = \mathbf{D}\overline{\phi} + \overline{b}\left(\overline{\eta},\overline{\phi}\right) + \mathbf{B}(\beta)\cdot\overline{\Psi}\\
\mathbf{M}\partial_t\overline{\phi} &= -\partial_{\overline{\eta}}\overline{H}_b = -g\mathbf{M}\overline{\phi} - \overline{\nu}\left(\overline{\phi}\right)
\end{aligned} \tag{4.6}$$

and an additional matrix system of linear elliptic equations from $\partial_{\overline{\Psi}} \overline{H}_b = 0$

$$[\mathbf{A} + \mathbf{G}]\, \overline{\Psi} = -\mathbf{B} \tag{4.7}$$

where $\overline{b}\left(\overline{\eta}, \overline{\phi}\right)$ and $\overline{\nu}\left(\overline{\phi}\right)$ are column vectors with elements

$$b_j = \partial_{\phi_j} \overline{H}_3 = \Sigma_{i,k} \eta_i \phi_k C_{ijk} \quad \text{and } \nu_j = \partial_{\eta_j} \overline{H}_3 = \frac{1}{2} \Sigma_{i,j} \phi_i \phi_k C_{ijk}$$

The algorithm to obtain numerical solutions for the system (4.6) and (4.7) by time stepping can be described as follows. For given initial conditions η_0 and ϕ_0, we calculate ψ_0 by solving the elliptic system in (4.7). Then by using the new ψ_1, we solve the dynamic system in (4.6) using a time integrator, a Runge-Kutta method (or ODEsolver in MATLAB) to obtain new η_1 and ϕ_1. These steps can be repeated until the desired end-time. In the calculation of the elliptic system in (4.7), we use an iterative method, i.e a preconditioned conjugate gradient method with a preconditioner obtained from an incomplete Cholesky factorization. This iterative method only needs 1-4 steps since we have an appropriate initial guess for ψ from the previous time step. Besides that, the matrices in (4.6) and (4.7) are very sparse since we use local basis functions for FEM, so the calculation is quite efficient.

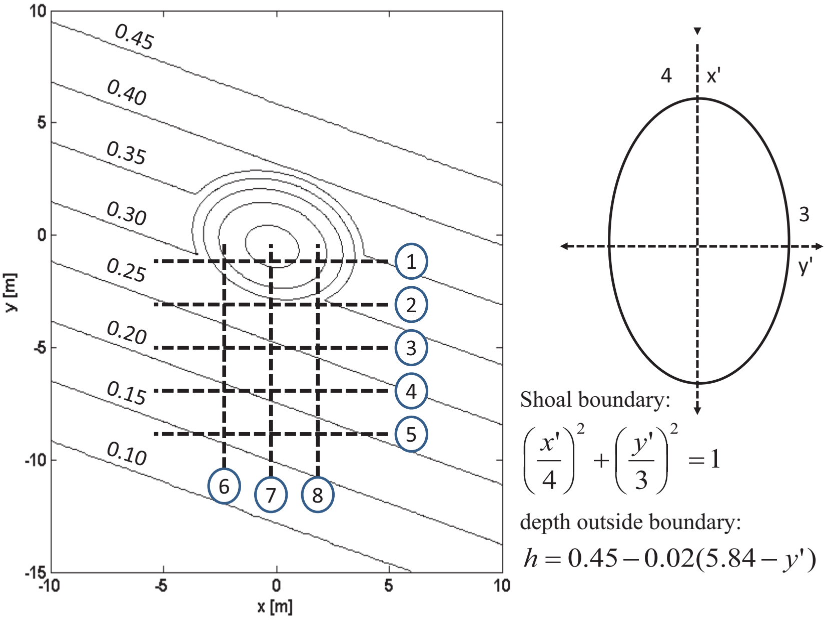

Figure 4.1: *Bottom configuration for the experiment of Berkhoff et al. [1982]. Dashed lines (labeled from 1 to 8) indicate sections where measurement data are available.*

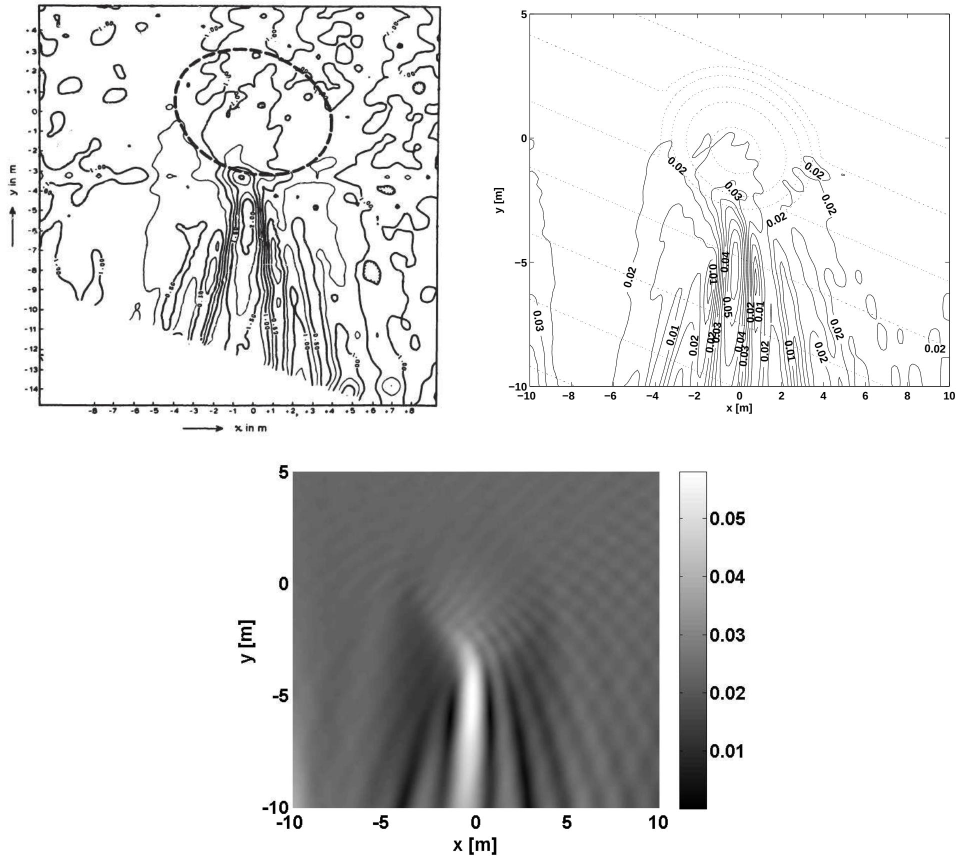

Figure 4.2: *Measured (upper left plot) and computed (upper right plot) amplitude contours (solid lines). In the lower plot the average of the computed maximal wave amplitude is shown.*

4.3 Wave propagation over a shoal

To show the performance of the 2D implementation of the model above, we perform a simulation of a monochromatic wave propagating above an elliptic shoal on a slope as in the experiment of Berkhoff et al. [1982]. This case is often used to demonstrate the stability, accuracy and efficiency of a model and its numerical implementation, since the waves are affected by shoaling, refraction, diffraction and non-linearity (Kirby and Dalrymple [1984]).

The laboratory setup for this experiment and the measurement sections are shown in Figure 4.1. An elliptic shoal is placed above 1/50 sloping bottom and turned at an angle 20^0 with the x-axis. The thickness of the shoal is

$$d = -0.3 + 0.5\sqrt{1 - (x'/5)^2 - (y'/3.75)^2}$$

Monochromatic waves with period 1 s and amplitude 2.32 cm are generated at the

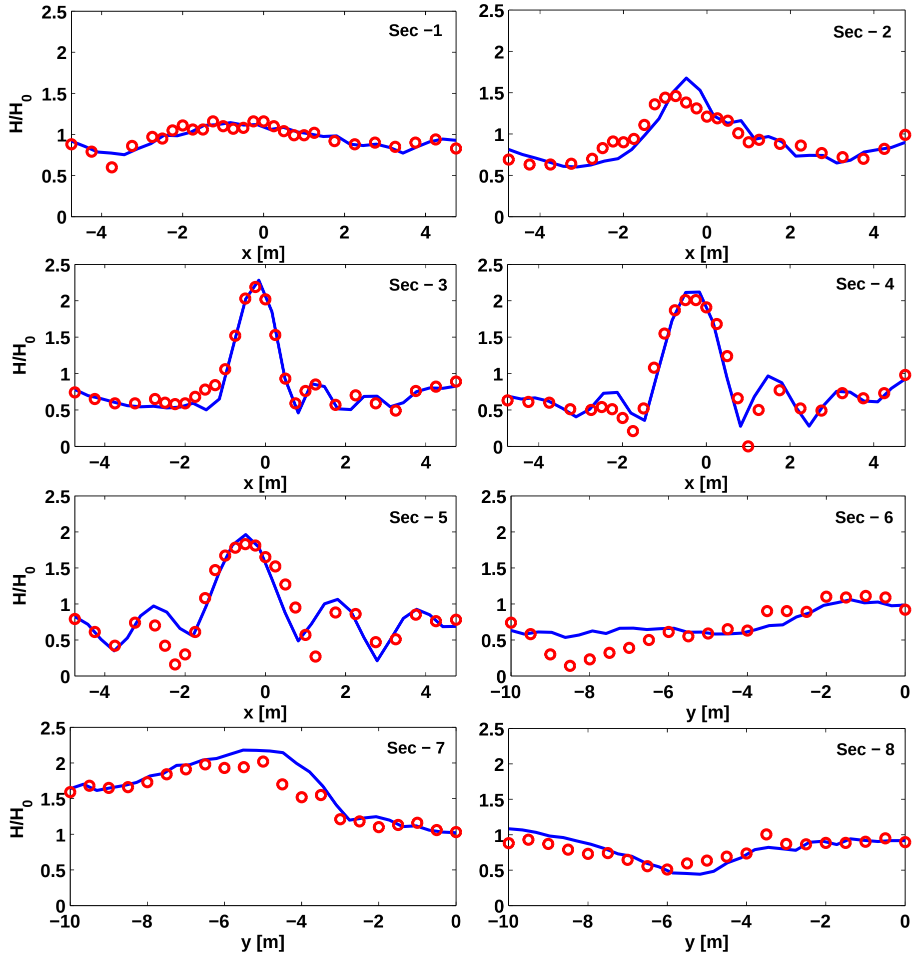

Figure 4.3: *Comparison of the measured (o o) and computed (-) normalized wave amplitude in eight sections.*

north boundary ($y = 10$) and propagate in the south direction. For the computation, the west and east boundary conditions (at $x = -10$ and $x = 10$) are set to be a fully reflective wall, while at the south an absorbing boundary condition is implemented using a sponge layer of 5 m wide. To influx a wave into the domain at the north boundary ($y = 10$), we use internal wave generation with a spatial delta function and modified influx signal with the group velocity of the model, similar with the method described in Kim et al. [2007]. We use an unstructured triangular grid with grid spacing approximately 0.1 m. The vertical profile function will depend on the depth $h(\mathbf{x})$; the wave number $\kappa(h(\mathbf{x}))$

of the Airy function (4.4) is such that it corresponds to the (fixed) input frequency ω_0 ($= 2\pi/\text{s}$) according to the VBM dispersion relation : $\Omega_{vbm}(\kappa(h), h) = \omega_0$.

In Adytia and van Groesen [2011] the calculation was done for the linear version of the model, in this chapter, we performed a simulation of the nonlinear version of the model over a time interval of 50 wave periods without any stability problem. The wave amplitude of the simulation is obtained by averaging the maximal amplitudes of the last 5 wave periods of the simulation (i.e. from $t = 45$ s to $t = 50$ s). In Figure 4.2, the amplitude contours are given of the measurement (upper left part) and of the simulation (upper right part). In the lower part the average of the maximal wave amplitude from $t = 45$ s to $t = 50$ s is shown.

Figure 4.3 shows the comparison between computed and measured normalized wave amplitude for the eight sections shown in Figure 4.1. Figure 4.2 shows that the model can follow the diffraction pattern, including the refraction effect in the wave focusing by the shoal. Figure 4.3 shows that the agreement between the measurement and the simulation is good.

4.4 Conclusions

Via the variational formulation of surface water waves, the VBM was derived by approximating the kinetic energy using a space-dependent Airy function as vertical structure in the fluid potential. The resulting system consists of two dynamic equations and an additional linear elliptic equation. In contrast with other Boussinesq-type equations, the system has no spatial derivatives of higher than second order, which allows for simple numerical implementation. In this Chapter, the model has been implemented in a 2D Finite Element (FE) method in a way that is consistent with the variational formulation. This implementation has been tested to simulate the experiment of Berkhoff et al. [1982] which represents the importance of diffraction, refraction and shoaling. Although nonlinearity is very important for the example that was given by Kirby and Dalrymple [1984], using this code, we found very little difference between linear and nonlinear simulations. The comparison between the model and measurements shows a good agreement.

Chapter 5

Coastal zone simulations in Jakarta harbour

Summary

In this chapter, we show realistic and synthetic coastal zone simulations in Tanjung Priok, the Harbour in Jakarta, Indonesia. To obtain a realistic wind wave condition, the energy spectrum of waves are calculated by a phase-averaging model SWAN (Booij et al. [1999]) in a large domain of Indonesia. Simulations of SWAN are performed in several nested areas, i.e. from a larger domain to the harbour. The resulting energy spectrum from the SWAN simulation in the smallest nested area is taken as input signal (by providing random phases) for the phase-resolving model: the OVBM. Since the peak frequency of the spectrum in the entrances of the harbour is very small, i.e. $T_{peak} \approx 3.5$ s, the simulations with OVBM are performed with three (vertical) profiles. The dynamic simulations in the harbour are investigated by analyzing the wave disturbances (the quotient of the significant waveheight and the input significant waveheight) and signals at several places in the inner harbour. As additions to the realistic simulation, synthetic extreme cases are performed by taking several JONSWAP spectra with larger peak-frequencies as input spectrum.

5.1 Introduction

A realistic wind wave condition in a coastal area such as a harbour, can be obtained by predicting first the wind wave condition in a larger area where the waves are generated. In this extensive area, the prediction is only practically possible in a phase-averaged sense. In this sense, the energy spectra of the wave are modelled, while the phases are assumed to be uniformly distributed. Over the last three decades, several phase-averaging models have been developed, e.g. WAM (WAMDI group 1988), WAVEWATCH III (Tolman [1991]) and SWAN (Booij et al. [1999]). The present-day models are known as third-generation models in which the spectral action balance equation is solved without any a priori restriction on the evolving spectrum during wave growth (see Section 6.4.7 of Holthuijsen [2007] for the first-, second- and third-generation concepts). The WAM and WAVEWATCH III models are primarily designed for deep water (oceanic scale), whereas the SWAN model (acronym for Simulating WAves Nearshore) is an extension of the deep water models to shallow water. The SWAN model incorporates formulations for deep water processes of wave generation, dissipation and the quadruplet wave-wave interactions from the WAM model (Komen et al.). In shallow water, these processes are supplemented by formulations for dissipation due to bottom friction, triad wave-wave interactions and depth-induced breaking (Booij et al. [1999]).

For our application in a coastal area such as a harbour, we choose the SWAN model for providing the wave energy spectrum near the harbour. The resulting wave energy spectrum near the harbour is then used as input signal (by providing random phases) for simulations of our phase-resolving model OVBM. Results of SWAN simulations in order to provide realistic wind wave condition in the Jakarta harbour are described in the following section.

5.2 Simulations of SWAN

The spectral model SWAN requires a bathymetry (bottom topography) and wind data as inputs for the simulations. The wind data is freely available from the National Centers for Environmental Prediction (NCEP) of the National Oceanic & Atmospheric Administration (NOAA). To obtain realistic wind wave conditions in the harbour of Jakarta, we choose an extreme wind event in Indonesia on 14 January 2010 (west monsoon wind). We perform stationary simulations of SWAN using a regular rectangular grid in 5 nested areas in Indonesia. For the largest domain, zero initial and boundary conditions for the spectral action balance equation are used. The resulting spectral wave conditions from this domain are then used as initial conditions for the simulation in smaller domain. This procedure is then repeated for the third, fourth and fifth nested domains. The simulations of SWAN that are shown here are performed in LabMath-Indonesia by Meirita Ramdhani.

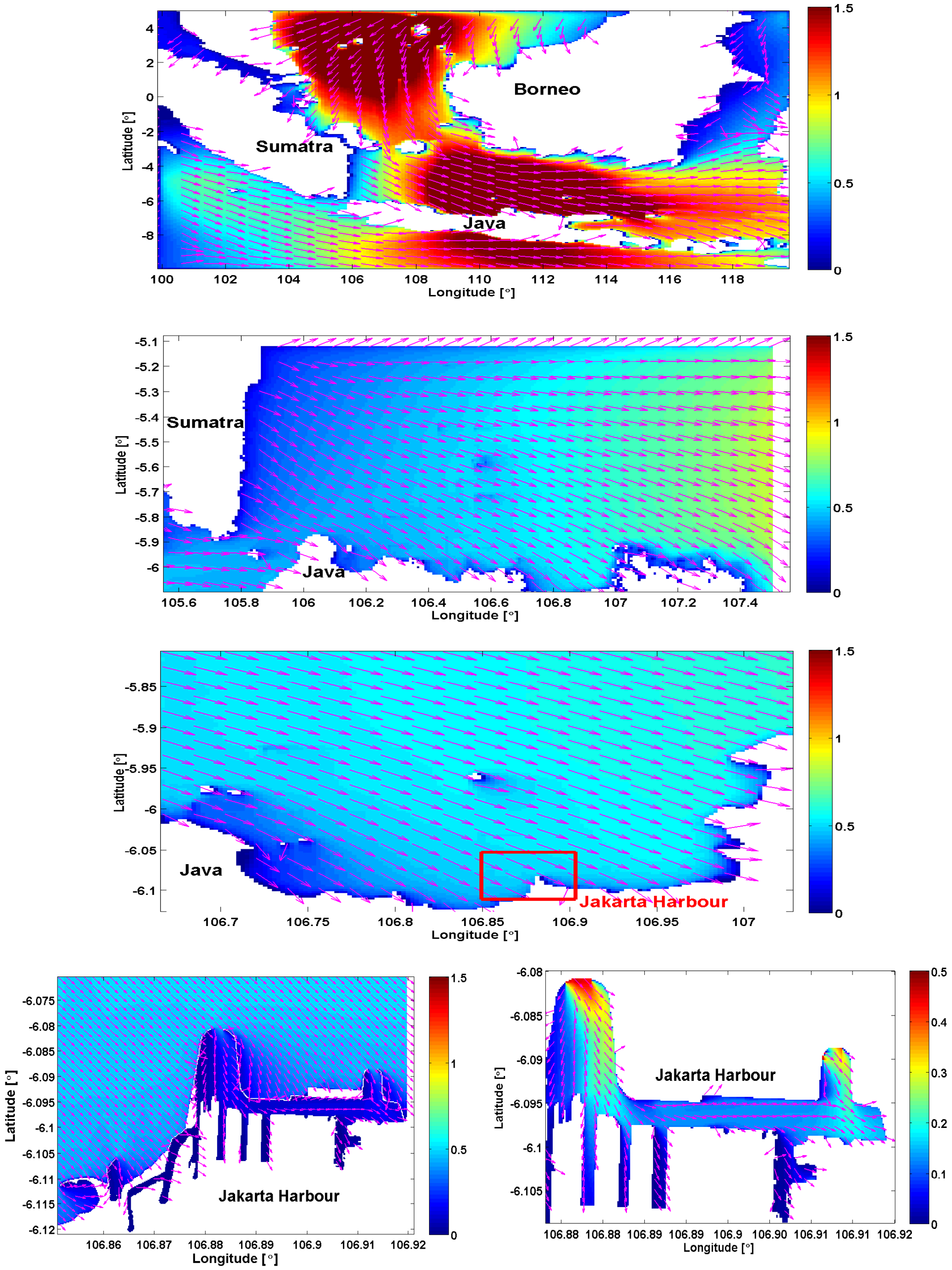

Figure 5.1: *Significant waveheight (indicated by colorbar, in meter) from the stationary simulations of SWAN in 5 nested areas in Indonesia by using the wind condition on 14 January 2010. The arrows indicates the wind directions. The resulting significant waveheight in the entrances of the Jakarta harbour is:* $H_{sig} \approx 0.4$ *m.*

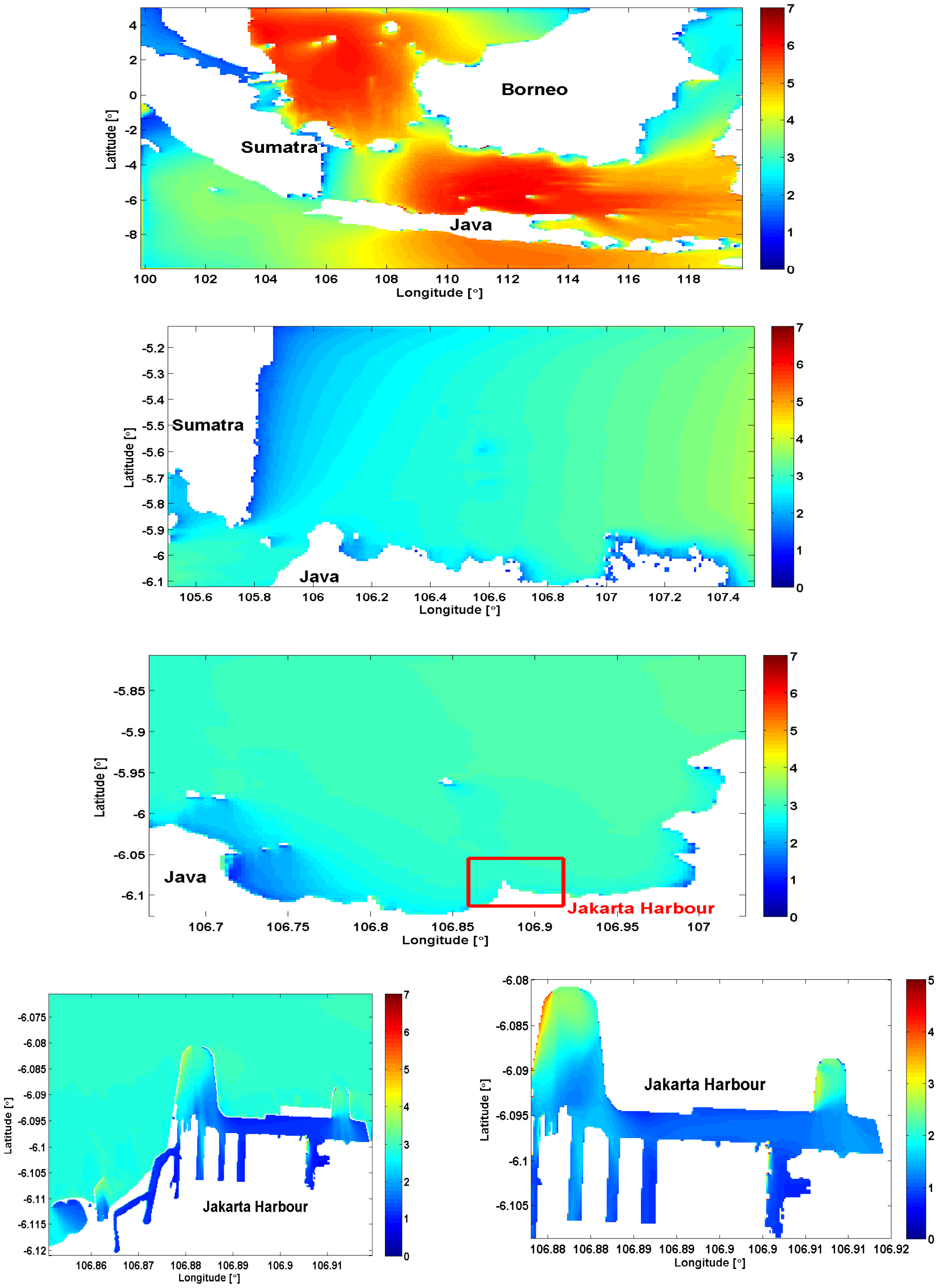

Figure 5.2: *The mean wave period (indicated by colorbar, in seconds) from the stationary simulations of SWAN in 5 nested areas in Indonesia. The resulting mean wave period in the entrances of the Jakarta harbour is:* $T \approx 3.5$ *s.*

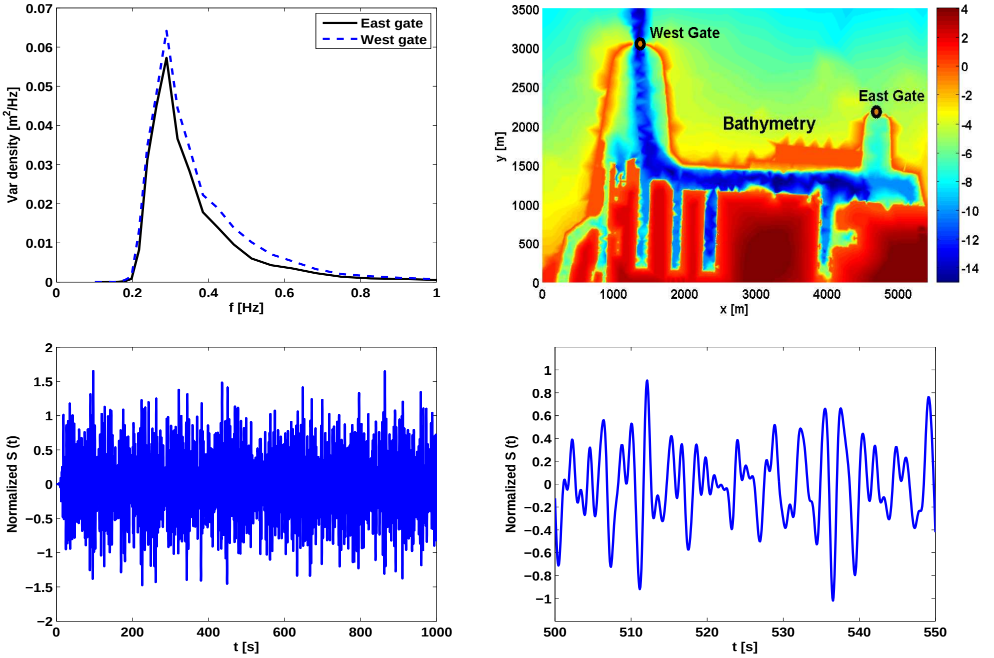

Figure 5.3: *The variance density spectrum (corresponds to energy spectrum) at the west and east gate of the Jakarta harbour are shown in the upper left plot. The upper right plot shows the locations of the west and east gates in the harbour. Here, the colorbar (in meter) indicates the bathymetry of the harbour. In the lower plots, the normalized time signal from the variance density in the west gate are illustrated.*

The simulations of SWAN provide several wind wave conditions as output:

i. The variance density spectrum (corresponds to the energy spectrum of the wave by multiplying it with ρg, where ρ is the mass density and g is the gravitational acceleration),

ii. The significant waveheight,

iii. The mean wave period.

In Figure 5.1, the significant waveheight from the simulations of SWAN are shown in 5 nested areas, and in Figure 5.2, the mean wave period from the simulation. From these figures, one can observe that the resulting wind wave condition at the harbour of Jakarta is rather calm: significant waveheight of approximately 0.4 m and period of 3.5 s in the entrances of the harbour. The resulting 1D variance density spectra in the entrances of the harbour are shown in the upper part of Figure 5.3. To obtain signals from this variance density spectra, we use random phases. In the lower part of Figure 5.3, normalized signals (divided by half of the significant waveheight) of the west gate spectrum is shown.

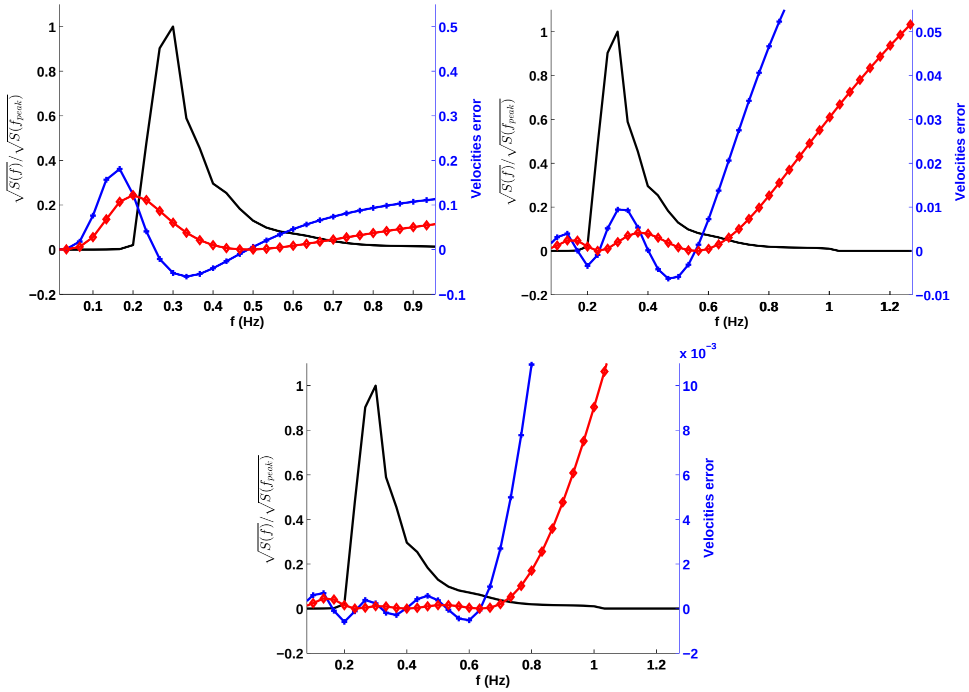

Figure 5.4: *The normalized energy spectrum (solid line, left hand axis) from the SWAN simulation at the west gate of Jakarta harbour ($h = 13.5$ m) is plotted together with the group velocity error (solid line with plus sign, right hand axis) and the phase velocity error (solid line with circle, right hand axis) as functions of frequency [Hz]. At the top left for the 1-profile OVBM with $\kappa = 0.92$ (corresponds to 0.48 Hz), at the top right for the 2-profile model with $\kappa_1 = 0.21$, $\kappa_2 = 1$ (corresponds to 0.23 Hz and 0.5 Hz) and at the lower for the 3-profile model with $\kappa_1 = 0.22$, $\kappa_2 = 0.63$, $\kappa_3 = 1.63$ (corresponds to 0.23 Hz, 0.4 Hz and 0.63 Hz).*

Now we use the resulting wind wave conditions, i.e. the energy spectrum and the significant waveheight, at the entrances of the Jakarta harbour as input signals for the OVBM. Simulations of the OVBM are described in the following section.

5.3 Simulations of OVBM

Simulations with OVBM will be performed in the interior of the harbour of Jakarta by taking input signals (at the harbour entrances) from the SWAN simulations. Illustrations of the input signals are shown in the lower part of Figure 5.3.

As shown in Figure 5.1, the significant waveheight in the entrances of the Jakarta harbour ($h = 13.5$ m) from the SWAN simulations is 0.4 m, and the wavelength of the peak waves of the spectrum in Figure 5.3 is very short, i.e. approximately 20 m. Therefore, we use the linear version of the OVBM for the simulations. Note that this is indeed a deep water situation in which the ratio of the depth and wavelength is $h/\lambda_0 > \frac{1}{2}$. Therefore

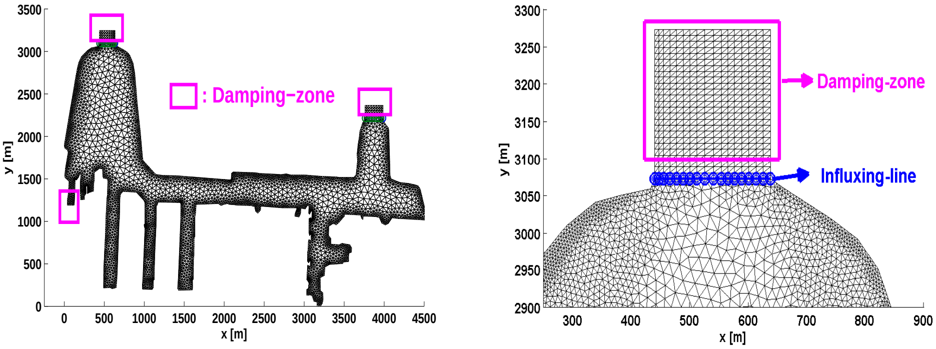

Figure 5.5: *Illustrations of the damping-zones, internal influxing line and an unstructured triangular grid for numerical simulation of the OVBM. The actual used grid size for the OVBM simulations is much finer than the illustration in this figure.*

traditional Boussinesq-type models, e.g. Peregrine [1967], Madsen and Sørensen [1992] and Nwogu [1993] will fail to simulate this type of waves due to lack of accuracy in the dispersiveness. This also holds for the commercial software package MIKE 21 BW (MIKE, by DHI software), the VBM with parabolic profile and the OVBM with one profile. The phase and group velocity errors of the OVBM with one, two and three profiles are plotted together with the spectrum from the SWAN simulation in Figure 5.4. These plots indicate that acceptable velocity errors are achieved by using three profiles: then for $f < 0.8$ Hz the error in the group and phase velocity is less than 1% and 0.1% respectively. We use three profiles to simulate the waves from the SWAN output. That is why for efficiency in computation time of wave dynamics, we restricted the simulation domain to the interior of the Jakarta harbour, and all waves outside the interesting area are damped by using a damping-zone. The domain of computation and the locations for damping-zones are illustrated in Figure 5.5. Here, we use the internal influx lines for wave generation (see Chapter 2). These are placed at both entrances of the Jakarta harbour. The waves are influxed uniformly into the domain with the same directions as the results of the SWAN, i.e. 34.5^o (west gate) and 29.5^o (east gate) counter clockwise from the north direction. For the boundary in the inner harbour, we use the fully reflective (hard wall) boundary conditions.

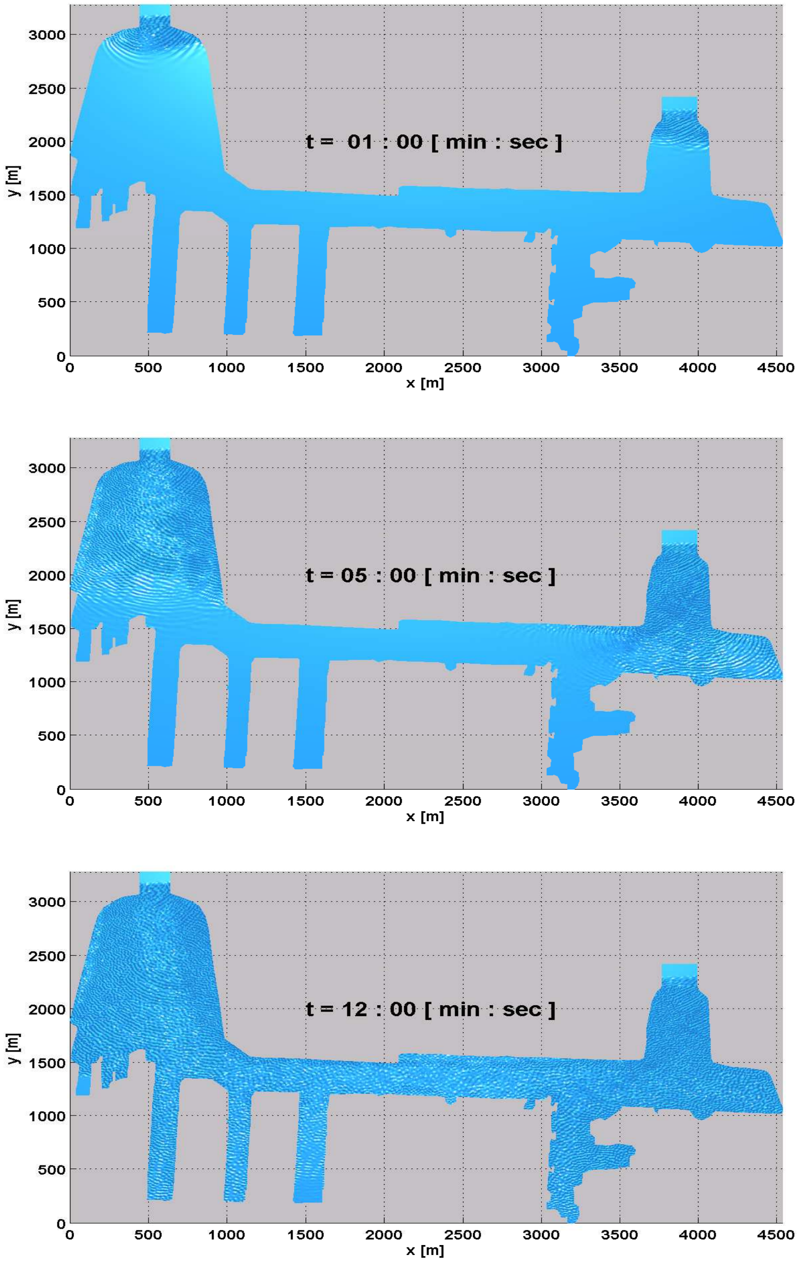

Figure 5.6: *Snapshots of the OVBM simulations with input spectrum from SWAN simulations ($T_{peak} = 3.5$) at $t = 1$ min, 5 min and 12 min. After 12 minutes, the inner harbour is filled with the waves.*

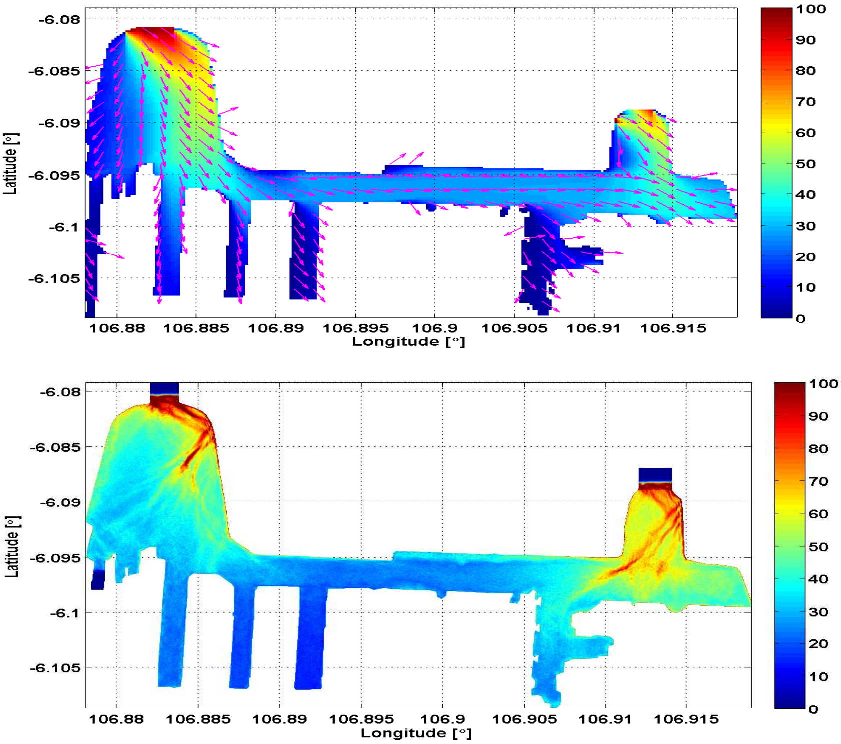

Figure 5.7: *Wave disturbances (in percentage) of the simulations with SWAN (upper plot) and the OVBM with three profiles (lower plot).*

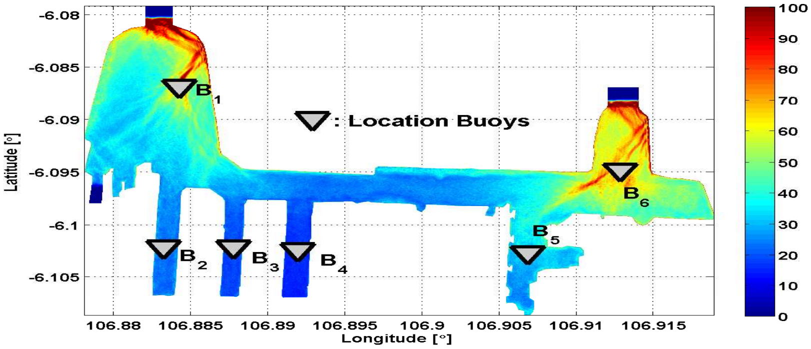

Figure 5.8: *Buoy positions for extracting elevation signals. The colorbar describes the wave disturbance (in percentage) from the OVBM simulations.*

As mentioned in Chapter 2, we use the unstructured triangular grid for 2D OVBM simulation. Since the expected waves will have rather short wavelength, we use a sufficiently fine grid to simulate the waves accurately. The resulting unstructured triangular grid has approximately 270.000 elements (triangles) and 135.000 nodes (points). An illustration of the unstructured triangular grid is shown in Figure 5.5, but the grid size for the OVBM simulations is much finer that the illustration in this figure.

The simulations of OVBM with three profiles are performed for 40 minutes physical time. The calculation time with three profiles takes 11 times of the physical time with a PC with 2.7GHz Intel i7 processor and 16GB of RAM. Snapshots of the simulations at $t = 1$, 5 and 12 minutes are shown in Figure 5.6. After 12 minutes, the inner harbour is completely filled with the waves.

An interesting quantity to investigate for harbour simulations is *the wave disturbance* in a harbour which is defined as

$$WD = \frac{H_{sig}}{H_{sig,input}} \times 100\%$$

where H_{sig} is the significant waveheight at a point in the harbour and $H_{sig,input}$ is the significant waveheight in the harbour entrance (significant waveheight of the influx signal). This quantifies the harbour's response with respect to waves that are influxed. From this quantity, one can investigate and analyze which area in the harbour will have the most significant disturbance.

Since the wave disturbance is a normalized significant waveheight, we compare the wave disturbance of the OVBM simulation with the SWAN simulation. This comparison is shown in Figure 5.7. In general, both results give the same behaviour. The differences that can be observed are the effects of diffraction especially near the west and east entrances of the harbour. The OVBM can simulate this physical aspect very well as shown in Chapter 4, while in SWAN, the diffraction is modelled in a restricted sense as stated in Booij et al. [1999] and in the Scientific and Technical Documentation of SWAN Cycle III (SWAN). SWAN cannot handle diffraction in a harbour or in front of reflecting obstacles properly.

Other differences are the reflections that can be seen clearly in the OVBM simulation, but cannot be observed in the SWAN simulation. Notice that, the OVBM does not include the effect of bottom dissipation, while in the SWAN simulation this effect is included. Since the waves are rather short (compared to the depth) in these simulations, i.e. $h/\lambda_0 > \frac{1}{2}$, this effect is very small and therefore can be neglected in these simulations outside the shallow area near the harbour entrances.

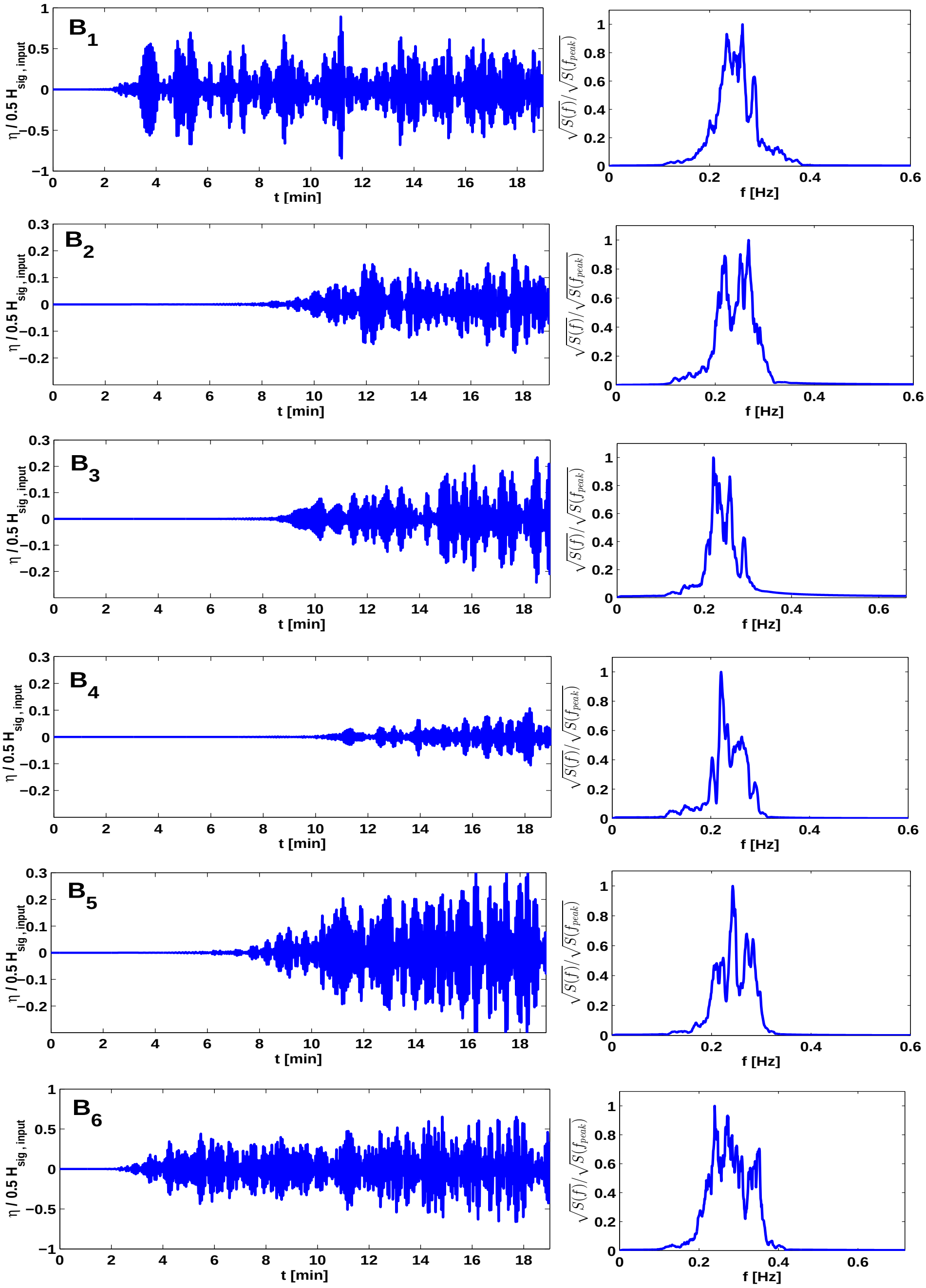

Figure 5.9: *Signals (left part) and their corresponding normalized energy spectrum (right part) at buoy positions:* B_1,B_2, $\cdots$, B_6 *as in Figure 5.8.*

From the calculation of the wave disturbance, we detect the elevation signals from the OVBM simulations at six (artificial) buoy positions. The location of these buoys is illustrated in Figure 5.8; in Figure 5.9, the signals and their corresponding normalized energy spectrum are shown. As indicated in the wave disturbance plot, the most significant disturbances are at positions B_1 and B_6. Locations where ships are docked in the harbour for loading and unloading cargos, i.e. buoy positions B_2, B_3, B_4 and B_5 are actually relatively calm. From the spectrum plots in the right part of Figure 5.9, at six buoy positions, the extracted elevation signals have frequency less than 0.4 Hz. By using three profiles model, as indicated in Figure 5.4, the velocity errors are less than 0.1% (phase velocity) and 1% (group velocity) until waves with frequency 0.8 Hz. So the simulation with three profiles is definitely good and simulation with two profiles could also have been used.

As addition to this realistic simulation, we will show synthetic extreme wave conditions to investigate the wave disturbance in the Jakarta harbour.

5.4 Simulations with synthetic extreme wave conditions

As shown in the previous section, realistic simulations in the Jakarta harbour that were obtained by taking an extreme wind condition at west monsoon time, result in relatively calm wave disturbances in the harbour. This is understandable, since the wind wave conditions near the Jakarta harbour have relatively small significant waveheight ($H_{sig} = 0.4$ m) and very short wave period ($T_{peak} = 3.5$ s).

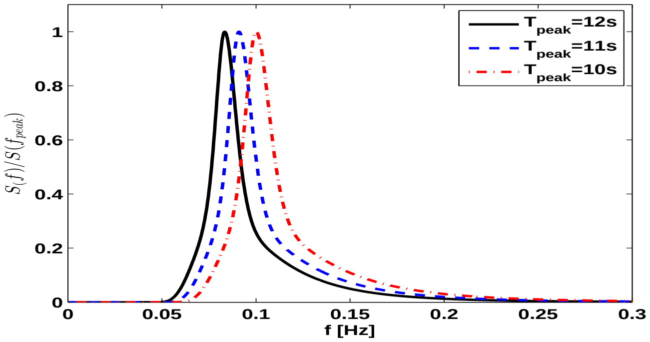

Figure 5.10: *JONSWAP spectrum with peak period* $T_{peak} = 12$ *s*,11 *s and* 10 *s for extreme cases in Jakarta harbour.*

To investigate the harbour's response for longer wave periods, synthetic extreme wind wave conditions can be obtained by taking JONSWAP-type of spectra (Hasselmann et al. [1973]) with longer peak period, e.g. $T_{peak} = 7$, 8, 9, 10, 11 and 12 s. The formula of JONSWAP (JOint North Sea WAve Project) spectra for peak wave-frequency f_{peak} is given by

$$S_{JON}\left(f\right) = \alpha g^2 \left(2\pi\right)^{-4} f^{-5} \exp\left[-\frac{5}{4}\left(\frac{f}{f_{peak}}\right)^{-4}\right]\gamma^a$$

with

$$a = \exp\left[-\frac{1}{2}\left(\frac{f/f_{peak}-1}{\sigma}\right)^2\right], \ \sigma = \begin{cases} 0.07, \text{ if } f \leq f_{peak} \\ 0.09, \text{ if } f \geq f_{peak}, \end{cases}$$

α is a constant that is proportional to H_{sig}, and is thus related to the wind speed and fetch length, g is the gravitational acceleration and f is the wave frequency.

In this section, we perform simulations of OVBM by using the spectra illustrated in Figure 5.10. In this plot, the JONSWAP spectra are normalized by their values at peak frequency. Since the peak period of the waves are rather long, simulations with one profile is accurate enough (with velocity errors less than 1%). Here we use coarser grid than in the previous section, i.e. an unstructured triangular grid with approximately 150.000 elements (triangles) and 75.000 nodes (points). The simulations are performed for 40 minutes physical time. The calculate time with one profile takes 4 times the physical time.

Snapshots of the simulations with input from JONSWAP with $T_{peak} = 10$ s at $t = 1$, 5 and 9 minutes are shown in Figure 5.11. After 9 minutes, the inner harbour is filled with the waves.

In Figure 5.12, the wave disturbance of the OVBM simulations with input from JONSWAP spectrum with $T_{peak} = 7$, 8 and 9 s, and in Figure 5.13 simulations with $T_{peak} = 10$, 11 and 12 s are shown. Notice that the scales of colorbar in Figure 5.12 and 5.13 are different than in Figure 5.7. Figure 5.12 and 5.13 show that the wave disturbance for waves with longer periods (therefore more energy) are much bigger. Since longer wave periods correspond to longer wavelengths, the effect of the bathymetry in these simulations is much bigger than for the realistic case in the previous section.

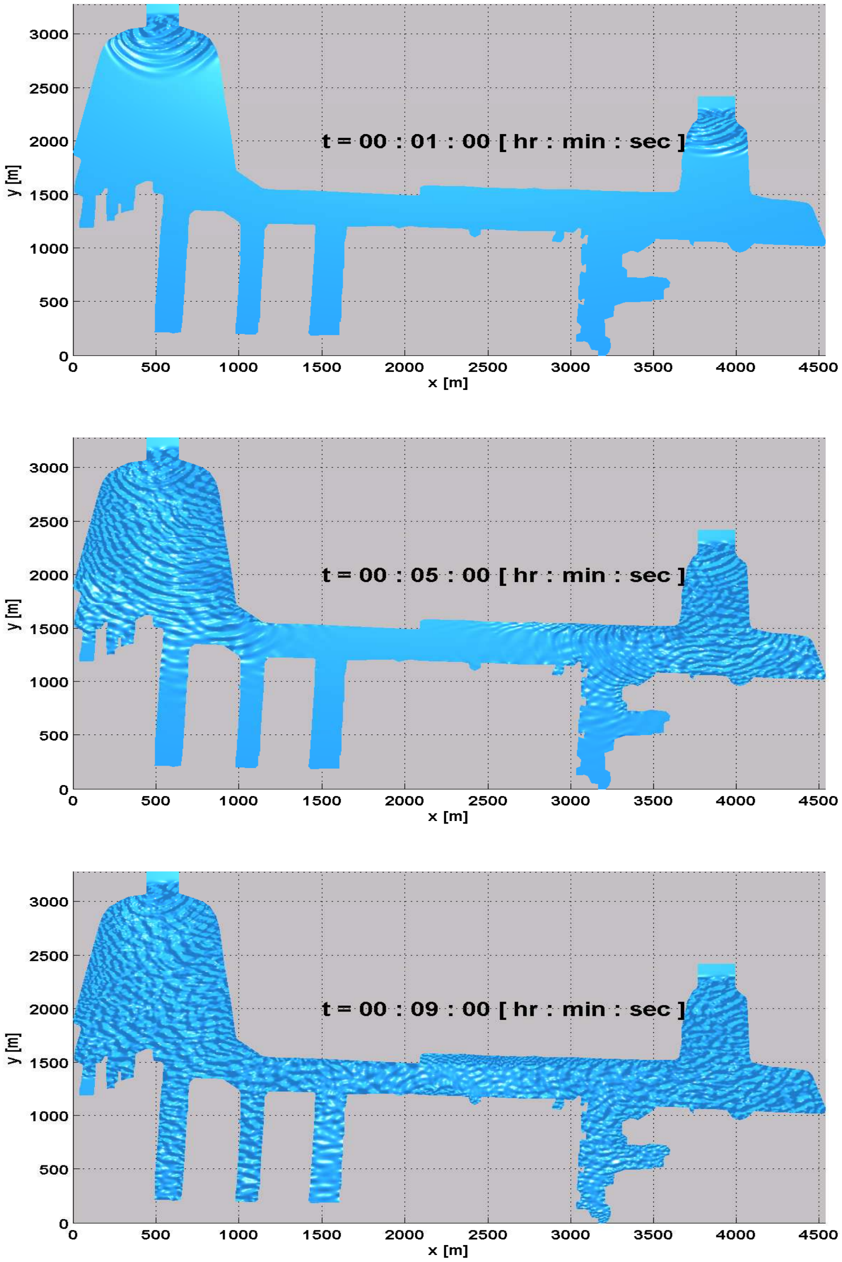

Figure 5.11: *Snapshots of the OVBM simulations with input signal from JONSWAP spectrum with* $T_{peak} = 10$ *s at* $t = 1$ *min,* 5 *min, and* 9 *min.*

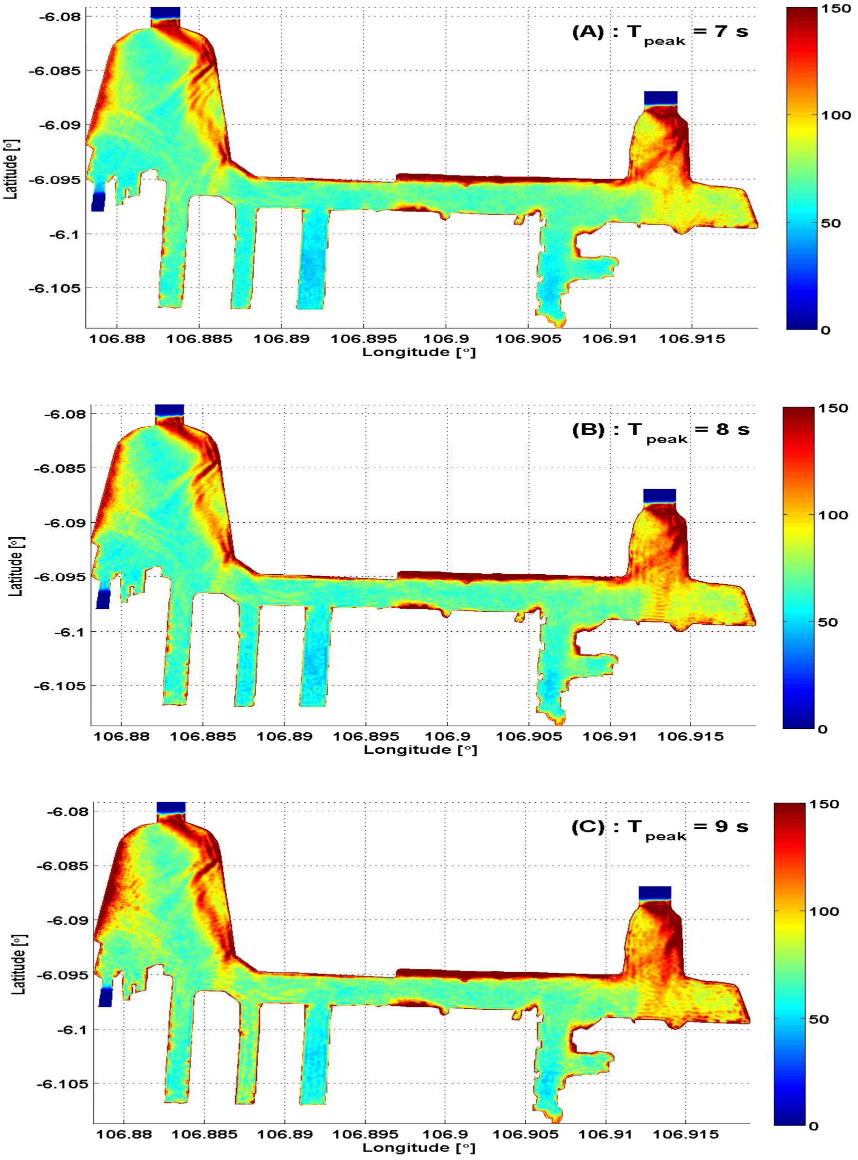

Figure 5.12: *Wave disturbances (in percentage) of simulations of the OVBM with influx from JONSWAP spectrum with* $T_{peak} = 7$ *s (upper plot), 8 s (middle plot) and 9 s (lower plot).*

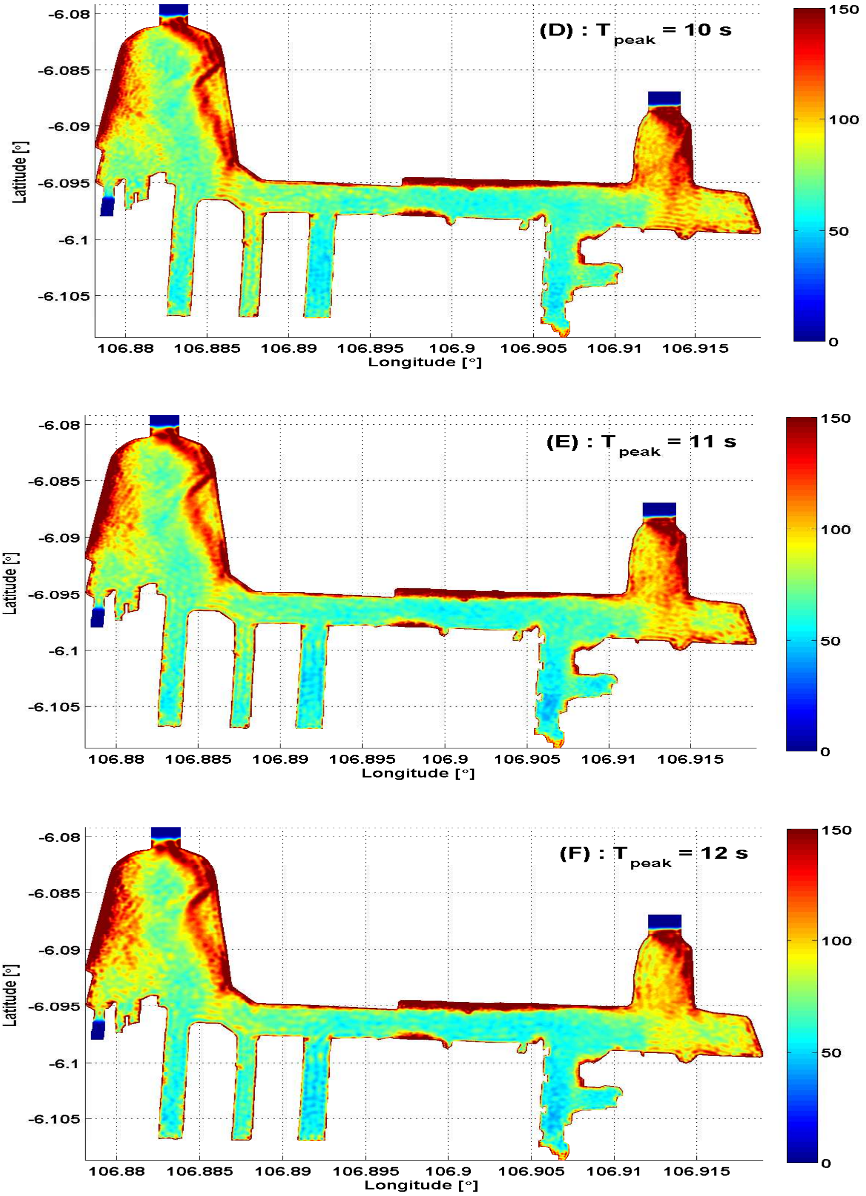

Figure 5.13: *Wave disturbances (in percentage) of simulations of the OVBM with influx from JONSWAP spectrum with* $T_{peak} = 10$ *s (upper plot),* 11 *s (middle plot) and* 12 *s (lower plot).*

5.5 Conclusions

Realistic simulations in the harbour of Jakarta, Indonesia, has been performed by using the spectral wave model SWAN and the phase-resolving model OVBM. The results of simulations show calm wind wave conditions with significant waveheight 0.4 m and mean wave period 3.5 s in the entrances of the harbour. Validations of the model simulations are limited by lack of measurement data in the inner harbour of Jakarta. But, from the comparison of wave disturbance, both models show (in general) similar behaviour, except for diffraction effects in which the SWAN model is limited.

Results of the simulations with input from JONSWAP spectrum $T_{peak} = 7$ s, 8 s,$\cdots$, 12 s, show much larger wave disturbance in the harbour. In particular, since the waves have longer wavelength, effects of the bathymetry are clearly seen in the west entrances and other shallow areas in the inner harbour.

Chapter 6

Conclusions and Outlook

6.1 Conclusions

In the earlier development of the VBM (Klopman et al. [2005, 2007, 2010]), *one* profile is used to approximate the depth dependence of the fluid velocity potential, either using a parabolic profile (inspirated by the parabolic shape function of the classical Boussinesq equations) or the Airy profile (based on the Airy linear theory). The VBM with parabolic profile performs well for relative water depth $kh < \pi$, i.e. for wavelengths in excess of twice the water depth h (see Klopman [2010]) and has the same the dispersion relation characteristics as the enhanced Boussinesq model of Madsen and Sørensen [1992] (see Figure 1.2). The VBM with one Airy profile can be tuned, through its parameter κ, to have exact dispersion for a certain wavenumber at a certain depth. The applicability of the earlier model is limited to rather long waves, e.g. tsunami waves, and rather narrow band waves. The earlier model has been used for tsunami simulations: Adytia [2008], van Groesen et al. [2008] and Adytia and van Groesen [2009].

For dealing with broad-band waves such as wind-generated waves, the quality of dispersiveness of the VBM needs to be improved. In this thesis, for signalling problems, the improvement is achieved by using a few Airy profiles (up to three profiles), and since each Airy profile is a function of a wavenumber κ, the choices of the κ's is obtained by defining an optimization criterion for a given influx signal. The optimization criterion that is used in this thesis is based on the idea introduced in Lakhturov, Adytia, and van Groesen [2012] for varying bottom. In this criterion, the kinetic energy is rewritten in a form that incorporates the initial power spectrum of the given initial signal. The error in the kinetic energy of the VBM compared to the least value which is achieved for exact dispersion, is minimized with respect to the wavenumbers κ. The resulting model is called the *Optimized VBM (OVBM)*. The flexibility to choose the number of vertical profiles and the possibility to optimize the vertical profiles means that the OVBM is *case-dependent*. This is different than other Boussinesq-type models where the quality of dispersiveness is measured by the largest relative water depth kh (given a certain accuracy) that can be achieved. This then holds for any simulation in this interval. In the OVBM, instead of achieving a larger value of kh for all kind of wave motions, the dispersion is optimized to give the highest desired accuracy in dispersiveness for the specific waves to be simulated for a given signal.

In the previous variant of the VBM (Klopman et al. [2005, 2007, 2010]), the model was implemented with a pseudo-spectral method on rectangular grids. A limitation of this implementation is a lack of flexibility when dealing with complicated domains such as harbours or complicated coastlines. In this thesis, supported by the fact that the VBM is derived using the variational formulation, it is chosen to implement the model with a Finite Element Method (FEM). The implementation is straightforward and simple, i.e. the use of linear spline basis functions is possible since the model has highest spatial derivatives of second order in the equations (and of first order in the Lagrangian form) and has no mixed spatial-temporal derivatives. Moreover, the use of unstructured triangular grids in 2D FE implementations increases the efficiency in computation and gives more flexibility compared to, e.g. curvilinear meshes and nested grids. The use of FE implementation for the OVBM has broaden the applicability compared to the previous variant of VBM (Klopman et al. [2010]).

Compared to other Boussinesq models, the VBM has positive Hamiltonian (see Klopman et al. [2010]) and is relatively simple for numerical implementation. As a drawback, an additional linear elliptic system has to be solved. But because of the positivity of the Hamiltonian and symmetry of the associated matrices in the elliptic system, for a large system with fine discretization, an iterative preconditioned conjugate gradient method has been used to solve the elliptic system. This step contributes 20% to 40% to the total computing time. This relatively low percentage can be achieved since a good initial guess is available from the previous time steps.

The efficiency and accuracy of the 1D FE implementation of OVBM for simulating broad band waves have been shown in Chapters 1 and 3. The use of 2- and 3-Airy profile and the optimization criterion for the vertical profile improves significantly the quality of the dispersiveness of the OVBM. Results of simulations and laboratory experiments agree very well. In general, for the 1D-FE code, the calculation time for the OVBM with two profiles takes 1.5 times longer than using one profile, and approximately the same for the OVBM with three profiles: 1.5 times longer than with two profiles. The calculation with three profiles is only necessary for very short and very broad band spectra waves as shown in Chapter 1 for the freak wave experiment of MARIN hydrodynamic laboratory. But for wind-generated waves (with JONSWAP-type of spectra), the calculation with two (vertical) profiles is usually accurate enough.

The performance of the 2D FE code has been shown for the experiment of Berkhoff et al. [1982]. This experiment is well known to test the accuracy of a code in representing effects of refraction, diffraction and shoaling. In Chapter 4, it is shown that results of simulations of the 2D FE code and the laboratory experiment agree very well. In Chapter 5, the 2D FE code of OVBM is tested for simulating realistic wind-generated waves in the harbour of Jakarta, Indonesia. Realistic wind-wave conditions are obtained by performing simulations of a phase-averaged model SWAN in a large area of Indonesia. Realistic wind wave conditions in the harbour produce relatively calm waves, even for an extreme wave condition as on 14 January 2010: waves with significant waveheight of 0.4 m and mean wave period of 3.5 s were calculated at the entrances of the harbour. Since the waves have short period, we performed the OVBM simulations with three profiles.

Validations of the model simulations are limited by lack of measurement data in the inner harbour of Jakarta. But, from comparison of the wave disturbance, results of simulations of SWAN and OVBM show similar behaviour, except for diffraction effects in which the SWAN model is limited.

6.2 Outlook

Development of the OVBM is part of the ongoing research in the Department of Applied Mathematics of University of Twente in collaboration with LabMath-Indonesia. Several physical aspects will be addressed in the near future to improve the present model and code.

From several comparisons with experimental data, the FE - code of OVBM performs very well. As stated in Chapter 1, the focus of this thesis is to improve the accuracy of the dispersion relation of the original variant of the VBM (Klopman et al. [2005, 2007, 2010]), and restricted to the *weakly-nonlinear* model (as defined in Klopman et al. [2005]). From several test cases that are shown in this thesis, the weakly-nonlinear version of the OVBM is accurate enough to represent the nonlinearity of waves. But for dealing with very steep waves, i.e. when $\nabla\eta$ is not negligible, generalization of the model to a *fully-nonlinear* model can be done by taking into account contributions of $\nabla\eta$ in the approximate kinetic energy. When needed, the model will be generalized to the fully nonlinear model.

To obtain more realistic simulations in a harbour, several physical aspects need to be addressed: wave breaking and effects of bottom friction. Just as in other Boussinesq-type models (Schäffer et al. [1993], Karambas and Koutitas [1992]), wave breaking will be included in the OVBM. Bottom friction becomes important as waves propagate into very shallow area. This has been shown in the synthetic simulations of the 2D FE-code in the harbour of Jakarta in Section 5.4 in Chapter 5. In plots of the wave disturbances in Figure 5.12 and 5.13, effects of bottom friction will change the behaviour of waves in the shallow area near the entrances of the harbour.

As mentioned above, in the early development of the VBM, tsunami simulations were performed in Indonesia's area (Adytia [2008], van Groesen et al. [2008] and Adytia and van Groesen [2009]). Now we will show briefly a recent application of the 2D-code for tsunami simulations in Indonesia (Adytia et al. [2012]).

In the present day, to tackle the serious and multiple water problems in the Jakarta area, one of various options is to built a 'Giant Sea Wall' in the Jakarta Bay. In view of the possibility that a tsunami may hit the Jakarta bay, the 'future' sea wall of Jakarta should better be constructed in such a way that it can withstand a tsunami. To obtain a rough indication of a possible tsunami in the Jakarta bay, we reconstructed the tsunami caused by the Krakatau explosion in 1883. Since the initiation of a tsunami is the most crucial element in tsunami modelling, any difference in the generation will cause differences in the propagating waves. Recently, Maeno and Imamura [2011] reconstructed the 1883 Krakatau tsunami where three types of generation mechanism are used: a pyroclastic flow model, a caldera collapse model and a phreatomagmatic explosion model. After careful consideration, it is concluded that one variant of pyroclastic flow gave the best match in comparison with the measured signal at Batavia (Verbeek [1885]). Since the pyroclastic flow model is a two fluid model in which the pyroplastic flow acts as the generating force

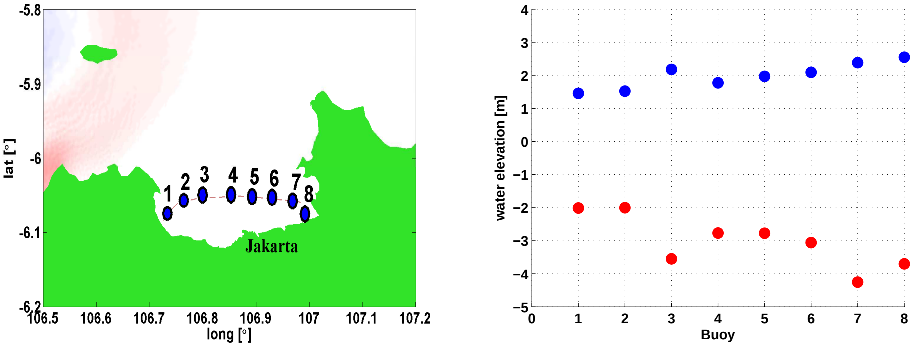

Figure 6.1: *Artificial buoy locations in the Jakarta bay are shown in the left plot. In the right plot, the maximal and minimal wave elevations at the 8 positions.*

for the nonlinear Shallow Water Equations (SWE) as the wave model, the generation is quite complicated. Instead, we adopted the phreatomagmatic model as initiation for the tsunami. By adjusting the wavelength (that corresponds to the spatial extent of the tsunami) and amplitude of the initial condition of phreatomagmatic, we obtain a signal that resembles reasonably the measured data in Batavia (Verbeek [1885]). Details of the VBM simulations is given in Adytia et al. [2012]. By using this initial condition, we observe conditions in the Jakarta bay as shown in Figure 6.1. A schematic drawing of hypothetical sea wall in Jakarta bay is shown in left plot of Figure 6.1, and maximal and minimal elevations at 8 (artificial) buoy locations are shown in the right plot.

In conclusion, to design such a sea wall, the designers should take into account the effects of such tsunami waves in the Jakarta bay. For instance, one consequence of an oblique collision against the wall is that, taking nonlinear effects into account, a four-fold amplitude amplification may arise if the wall is smooth (see Yeh et al. [2011], Peterson and van Groesen [2000] and Peterson et al. [2003]). The design of a wall-form that prevents a large amplification (and correspondingly huge forces on the wall) could be an additional challenge.

Bibliography

MIKE21 by DHI software. URL `http://mikebydhi.com`.

SWAN. URL `http://swanmodel.sourceforge.net`.

M. B. Abbott, H. M. Petersen, and O. Skovgaard. On the numerical modelling of short waves in shallow water. *J. Hydr. Res*, 16:173–203, 1978.

D. Adytia. Tsunami simulation in indonesia'a areas based on Shallow Water Equations and Variational Boussinesq Model using Finite Element Method. Master's thesis, Institut Teknologi Bandung, Dept. Mathematics, Bandung, Indonesia, 2008.

D. Adytia and E. van Groesen. Variational Boussinesq model for simulations of coastal waves and tsunamis. *Proc.* 5^{th} *Int. Conf. on Asian Pacific Coasts in Singapore; World Scientific 2010.*, pages 122–128, 2009.

D. Adytia and E. van Groesen. The variational 2D Boussinesq model for wave propagation over a shoal. *International Conference on Developments in Marine CFD in Chennai, India. RINA*, pages 25–29, 2011.

D. Adytia and E. van Groesen. Optimized variational 1D Boussinesq modelling for coastal waves propagating over a slope. *Coast. Eng.*, 64:139–150, 2012.

D. Adytia, M. Woran, and E. van Groesen. Effect of a possible Anak Krakatau explosion in the Jakarta bay. *Proc. of Basic Science International Conference 2012, Malang, Brawijaya University*, 2012.

Y. Agnon, P. A. Madsen, and H. A. Schäffer. A new approach to high order Boussinesq models. *J. Fluid Mech.*, 399:319–333, 1999.

G. A. Athanassoulis and K. A. Belibassakis. A consistent coupled-mode theory for the propagation of small-amplitide water waves over variable bathymetry regions. *J. Fluid Mech.*, 389:275–301, 1999.

K. A. Belibassakis and G. A. Athanassoulis. A coupled-mode system with application to nonlinear water waves propagating in finite water depth and in variable bathymetry regions. *Coast. Eng.*, 58:337–350, 2011.

J. C. W. Berkhoff, N. Booij, and A. Radder. Verification of numerical wave propagation models for simple harmonic linear water waves. *Coast. Eng.*, 6:255–279, 1982.

N. Booij, R. C. Ris, and L. H. Holthuijsen. A third-generation wave model for coastal regions, part i, model description and validation. *J. Geoph. Research*, 104(C4):7649–7666, 1999.

J. V. Boussinesq. Théorie des ondes et des remous qui se propagent le long d'un canal rectangulaire horizontal, en communiquant au liquide contenu dans ce canal des vitesses sensiblement pareilles de la surface au fond. *J. Math. Pures Appl.*, 17:55–108, 1872.

L. J. F. Broer. On the Hamiltonian theory of surface waves. *Appl. Sci. Res.*, 29:430–446, 1974.

L. J. F. Broer. Approximate equations for long wave equations. *Appl. Sci. Res.*, 31(5): 377–395, 1975.

L. J. F. Broer, E. W. C. van Groesen, and J. M. W. Timmers. Stable model equations for long water waves. *Appl. Sci. Res.*, 32:619–636, 1976.

D.R. Fuhrman and P. A. Madsen. Simulation of nonlinear wave run-up with a high-order Boussinesq model. *Coast. Eng.*, 55(2):139–154, 2008.

A. E. Green and P. M. Naghdi. A derivation of equation for wave propagation in water of variable depth. *J. Fluid Mech.*, 78:237–246, 1976.

WAMDI Group. The WAM model - a third generation ocean wave prediction model. *J. Phys. Oceanogr.*, 18:1775–1810, 1988.

K. Hasselmann, T.P. Barnett, E. Bouws, H. Carlson, D.E. Cartwright, H. Gienapp K. Enke, J.A. Ewing, D.E. Hasselmann, P. Kruseman, A. Meerburg, P. Müller, D.J. Olbers, K. Richter, W. Sell, and H. Walden. Measurement of wind-wave growth and swell decay during the Joint North Sea Wave Project (JONSWAP). *Deutsch. Hydrogr. Z.*, 12, 1973.

S. Haver. Freak waves: a suggested definition and possible consequences for marine structures. In M. Olagnon and M. Prevosto, editors, *Proc. Rogue Waves, Ifremer, France*, 2004.

S. Haver and O. Jan Andersen. Freak waves: rare realizations of a typical population or typical realizations of a rare population? In *Proc. of the* 10^{th} *International offshore and Polar Engineering Conference (ISOPE), Seattle USA*, pages 123–130, 2000.

Leo H. Holthuijsen. *Waves in Oceanic and Coastal Waters.* Cambridge University Press, 2007.

T. K. Karambas and C. Koutitas. A breaking wave propagation model based on the Boussinesq equations. *Coast. Eng.*, 18:1–19, 1992.

A. B. Kennedy, J. T. Kirby, Q. Chen, and R. A. Dalrymple. Boussinesq-type equations with improved nonlinear performance. *Wave Motion*, 33:225–243, 2001.

G. Kim, C. Lee, and K. D. Suh. Internal generation of waves: Delta source function method and source term addition method. *Ocean Engineering*, 34:2251–2264, 2007.

J. T. Kirby. *Gravity Waves in Water of Finite Depth*, chapter Nonlinear, dispersive long waves in water of variable depth., pages 55–125. Computational Mechanics Publications, 1997.

J. T. Kirby and R. A. Dalrymple. Verification of a parabolic equation for propagation of weakly-nonlinear waves. *Coast. Eng.*, 8:219–232, 1984.

G. Klopman. *Variational Boussinesq modelling of surface gravity waves over bathymetry.* PhD thesis, University of Twente, Dept. of Applied Mathematics, Enschede, The Netherlands, 2010.

G. Klopman, M. W. Dingemans, and E. van Groesen. A variational model for fully non-linear water waves of Boussinesq type. *Proc.* 20^{th} *Int. Workshop on Water Waves and Floating Bodies, Longyearbyen, Spitsbergen, Norway*, 2005.

G. Klopman, M. W. Dingemans, and E. van Groesen. Propagation of waves groups over bathymetry using a variational Boussinesq model. *Proc.* 22^{th} *Int. Workshop on Water Waves and Floating Bodies, Plitvice, Croatia*, 2007.

G. Klopman, E. van Groesen, and M. Dingemans. A variational approach to Boussinesq modelling of fully non-linear water waves. *J. Fluid Mech.*, 657:36–63, 2010.

G. K. Komen, L. Cavaleri, M. Donelan, K. Hasselmann, S. Hasselmann, and P. A. E. M. Jassen. *Dynamics and Modelling of Ocean waves.* Cambridge University Press, Cambridge, UK.

I. Lakhturov and E. van Groesen. Optimized Variational Boussinesq Modelling; part 1: Broad-band waves over flat bottom. *Internal report, University of Twente*, 2010. URL `http://eprints.eemcs.utwente.nl/`.

I. Lakhturov, D. Adytia, and E. van Groesen. Optimized Variational 1D Boussinesq modelling for broad-band waves over flat bottom. *Wave Motion*, 49(2):309–322, 2012.

J. Larsen and H. Dancy. Open boundaries in short wave simulations - a new approch. *Coast. Eng.*, 7:285–297, 1983.

L. She Liam, D. Adytia, and E. van Groesen. On internal wave generation for 1 and 2D dispersive surface wave models. In preparation.

J. C. Luke. A variational principle for fluid with a free surface. *J. Fluid Mech.*, 27: 395–397, 1967.

P. Lynett and P.L.-F. Liu. A two-layer approach to wave modeling. *Proc. R. Soc. Lond. A.*, 460:2637–69, 2004a.

P. Lynett and P.L.-F. Liu. Linear analysis of the multi-layer model. *Coast. Eng.*, 51: 439–454, 2004b.

P. A. Madsen and D. R. Fuhrman. *Advances of Numerical Simulation of Nonlinear Water Waves*, chapter Higher-order Boussinesq-type modelling of nonlinear wave phenomena in deep and shallow water., pages 245–285. World Scientific, 2010.

P. A. Madsen and H. A. Schäffer. Higher order Boussinesq-type equations for surface gravity waves : derivation and analysis. *Phil. Trans. R. Soc. Lond. A.*, 356:3123–3181, 1998.

P. A. Madsen and O. R. Sørensen. A new form of the Boussinesq equations with improved linear dispersion characteristics. Part 2: A slowly-varying bathymetry. *Coast. Eng.*, 18:183–204, 1992.

P. A. Madsen and I. R. Warren. Performance of a numerical short-wave model. *Coast. Eng.*, 8:73–93, 1984.

P. A. Madsen, R. Murray, and O. R. Sørensen. A new form of the Boussinesq equations with improved linear dispersion characteristics. Part 1. *Coast. Eng.*, 15:371–388, 1991.

P. A. Madsen, H. B. Bingham, and H. Liu. A new Boussinesq method for fully nonlinear waves from shallow to deep water. *J. Fluid Mech.*, 462:1–30, 2002.

P. A. Madsen, H. B. Bingham, and H. A. Schäffer. Boussinesq-type formulations for fully nonlinear and extremely dispersive water waves : derivation and analysis. *Proc. R. Soc. Lond. A.*, 459:1075–1104, 2003.

F. Maeno and F. Imamura. Tsunami generation by rapid entrance of phyroclastic flow into the sea during the 1883 Krakatau eruption, Indonesia. *J. Geophys. Res.*, 116, 2011.

C. C. Mei and B. Le Méhauté. Note on the equations of long waves over an uneven bottom. *J. Geophys. Res*, 71:393–400, 1966.

D. M. Milder. A note on: 'On Hamilton's principle for surface waves'. *J. Fluid Mech.*, 83(1):159–161, 1977.

D. M. Milder. The effect of trucation on the surface-wave Hamiltonian. *J. Fluid Mech.*, 216:249–262, 1990.

J. W. Miles. On Hamiltonian's principle for surface waves. *J. Fluid Mech.*, 83:153–158, 1977.

K. Nadaoka, S. Beji, and Y. Nakagawa. A fully-dispersive weakly nonlinear model for water waves. *Proc. R. Soc. London A*, 453(1957):303–318, 1997.

O. Nwogu. Alternative form of Boussinesq equations for nearshore wave propagation. *J. Waterw. Port Coast. Ocean Eng.*, 119:618–638, 1993.

D. H. Peregrine. Long waves on a beach. *J. Fluid Mech.*, 27:815–827, 1967.

P.-O. Persson and G. Strang. A simple mesh generator in matlab. *SIAM Review*, 46(2): 329–345, 2008.

P. Peterson and E. van Groesen. A direct ind inverse problem for wave crests modelled by interactions of two solitons. *Physica D*, 141:316–332, 2000.

P. Peterson, T. Soomere, J. Engelbrecht, and E. van Groesen. Soliton interaction as a possible model for extreme waves in shallow water. *Nonlinear Processes in Geophysics*, 10:503–510, 2003.

M. M. Rienecker and J. D. Fenton. A Fourier approximation method for steady water waves. *J. Fluid Mech.*, 104:119–137, 1981.

H. A. Schäffer, P. A. Madsen, and R. Diegaard. A Boussinesq model for waves breaking in shallow water. *Coast. Eng.*, 20:185–202, 1993.

H. Schaper and W. Zielke. A numerical solution of boussinesq type wave equations. *Proc.* 19^{th} *Int. Conf. on Coastal Engineering*, pages 1057–1071, 1984.

P. F. Serre. Contribution á l'étude des écoulements permanents et variables dans les canaux. *La Houille Blanche*, 830-872:374–388, 1953.

H. L. Tolman. A third-generation model for wind waves on slowly varying, unstready and inhomogeneous depths and currents. *J. Phys. Oceanogr.*, 21(6):782–797, 1991.

E. van Groesen and Andonowati. Variational derivation of KdV-type of models for surface water waves. *Physics Letters A*, 366(3):195–201, 2007.

E. van Groesen and Andonowati. Fully dispersive dynamic models for surface water waves above varying bottom, Part 1: Model equations. *Wave Motion*, 48:657666, 2011.

E. van Groesen and Jaap Molenaar. *Continuum Modelling in the Physical Sciences, in: Mathematical Modeling and Computation.* SIAM, 2007.

E. van Groesen and I. van der Kroon. Fully dispersive dynamic models for surface water waves above varying bottom, Part 2: Hybrid spatial-spectral implementations. *Wave Motion*, 49:198–211, 2012.

E. van Groesen, D. Adytia, and Andonowati. Near-coast tsunami waveguiding: phenomenon and simulations. *Natural Hazard and Earth System*, 8:175–185, 2008.

E. van Groesen, Andonowati, L. She Liam, and I. Lakhturov. Accurate modelling of uni-directional surface waves. *J. Comput. Appl. Math.*, 234:1747–1756, 2010.

R. D. M. Verbeek. *Krakatau.* Gov. Press. Batavia, Indonesia, 1885.

G. Wei, J. T. Kirby, S. T. Grilli, and R. Subramanya. A fully nonlinear Boussinesq model for surface waves. Part 1. Highly nonlinear unsteady waves. *J. Fluid Mech*, 294:71–92, 1995.

G. Wei, J. T. Kirby, and A. Sinha. Generation of waves in Boussinesq models using a source function method. *Coast. Eng.*, 36:271–299, 1999.

G. B. Whitham. Variational methods and applications to water waves. *Proc. R. Soc. London A*, 299(1456):6–25, 1997.

J. M. Witting. A unified model for the evolution of nonlinear water waves. *J. Comput. Phys*, 56:203–236, 1984.

H. Yeh, S. Sato, and Y. Tajima. Waveform evolution of the 2011 east Japan tsunami. *Proc.* 6^{th} *Int. Conf. on Asian Pacific Coasts in Hong Kong, China*, pages 131–138, 2011.

Sung B. Yoon and Philip L.-F. Liu. A note on Hamiltonian for long water waves in varying depth. *Wave Motion*, 20:359–370, 1994.

V. E. Zakharov. Stability of periodic waves of finite amplitude on the surface of a deep fluid. *J. Appl. Mech. and Tehn. Phys.*, 657:190–194, 1968.

Z. L. Zou. A new form of higher order Boussinesq equations. *Ocean Eng.*, 27:557–575, 2000.

Acknowledgments

The research presented in this thesis has been carried out over the past (almost) 4 years in the Applied Analysis and Mathematical Physics (AAMP) group at University of Twente and in Laboratorium Matematika Indonesia (LabMath-Indonesia) in Bandung.

First of all, I would like to express sincere gratitude to my promotor Prof. E. (Brenny) van Groesen for trusting me to do many things in mathematics (and outside mathematics), which I found very interesting. And (again) for giving me an opportunity to do directly a postdoc with the same topic, which will start next month. Yes, you have convinced me that 'mathematics is very useful and fascinating'. Secondly, my gratitude goes to Dr. Andonowati, who providing me a very nice place to stay during my research in Indonesia: Laboratorium Matematika Indonesia.

Especially I would like to thank Prof. Stephan van Gils for the opportunity to work in his group, and also his willingness to be one of my graduation committee.

I also would like to thank to other members of my graduation committee: Prof. René Huijsmans, Prof. Wim Uijttewaal, Prof. Suzanne Hulscher and Prof. Christian Kharif (who comes all the way from Marseille, France). I also would thank to Prof. A.J. Mouthaan as the chairperson and secretary of my graduation committee.

Special thanks for MARIN hydrodynamic Laboratory, who provides me experiment data from which I can test my model and code.

Further I want to thank my friends and colleagues in the MPCM: Wenny Kristina and Arnida Latifah (who willing to be my paranymph and shared fruitful friendship), Ruddy Kurnia, Pak Tito Julianto (my spiritual mentor), She Lie Liam, Ivan Lakhturov, Anastasia Bukhvostova, David Lopez-Penha, Julia Mikhal, Shavarsh Nurijanyan, Sid Visser, Lilya Ghazaryan, Elena Gagarina and Marcel Lourens. Especially I express my sincere thanks to our secretaries Mariëlle Slotboom-Plekenpol and Linda Wychgel - van Dalm for all their help during my stay in Enshede. I thank Gerard Jeurnink for involving me in educational activities as his teaching assistant. I thank Gert Klopman for a nice discussion about coding during his stay in Bandung.

In the beginning of developing my Finite Element code, I learned a lot a programming experience from Pak Sena and Oscar Osaputra. I thank them for this.

During my stay in Enschede, I shared a fruitful friendship with Indonesian friends: Tettri Nuraini and Winkausyar Wanranto (thank you for our adventures), Adit Jayusman, Ferry Haris, Eyla Maranny, Muhammad Zeno, Yusuf, Irdham Kusumawardhana, Wisnu, Yuti Ariani, Poppy Ramdhania, Dayu Roosanti, Cut Susanti, Yusi Mursityo and all member of PPIE that I cannot list them all here. I thank Ibu Vina Serevina for all her advises and being my very nice neighbour in Stadweide. My special thanks go to David Marpaung (and his wife Vince) for his help for my thesis template, printing and all technicalities regarding my defense. I appreciate it very much.

During my stay in Bandung, I indebted many thanks for Ibu Dian Astuti and Mira Melanie, for helping me with all kind of administrative processes. I thank Meirita Ramdhani for providing me the simulation of SWAN, also Pak Wiwin Windupranata for nice discussion about comparing our simulations. I have to mention also my colleagues in LabMath-Indonesia: Andy Scauff, Mourice Woran, Erwin Vonk, Amanda, Zulkarnain and Dwi Saputri (for providing the simulation of MIKE21).

Lastly and most importantly I wish to thank my big family: my late father Husin Mas'ud and my mother Yensi Nio (who always support me, whatever I do), my wife Fara lingga (for your patience and support) and my son (to be born next month), Indra Jaya, Ika trinanda, Tinton Ariestanto, Hanny Widiastuti, mama Resofin Yusuf, Ibu Tati and Rosdiana. Alhamdulillah.

About the author

Didit Adytia was born on the 5^{th} of February 1983 in Tanjung Pandan, Belitung, Indonesia. He received his Bachelor of Science degree (cum laude) from Mathematics department of Institut Teknologi Bandung (ITB), Indonesia in July 2006 on a subject of "Water wave evolutions based on Boussinesq equations" under supervision of Dr. Sri Redjeki Pudjaprasetya and Dr. Andonowati. Directly after this, he started his study as Master's student at the same department. In June 2008, he finished his Master's thesis with title "Tsunami simulation in Indonesia's areas based on shallow water equations and variational Boussinesq model using Finite Element Method" under supervision of Dr. Andonowati. During his master study, he also worked as an internship student in Laboratorium Matematika (LabMath) Indonesia.

In July 2008, he started his Ph.D. research in Applied Analysis and Mathematical Physics (AAMP) group, Department of Applied Mathematics, University of Twente, under supervision of Prof. dr. E.W.C. van Groesen. This PhD work is executed partly at LabMath-Indonesia in Bandung. In May 2012, he finished his doctoral studies. The result of his research is contained in this thesis.

Didit Adytia is now employed (starting 1^{st} of June 2012) as a post-doctoral researcher in AAMP group University of Twente, working on topic of wave breaking and forces on structure using Variational Boussinesq Model. This project is funded by STW.